



FRIEDRICH–SCHILLER–UNIVERSITÄT JENA  
PHYSIKALISCH–ASTRONOMISCHE FAKULTÄT  
ASTROPHYSIKALISCHES INSTITUT UND  
UNIVERSITÄTS–STERNWARTE



# Thermal Emission Modeling of Circumstellar Debris Disks

—DISSERTATION—

zur Erlangung des Akademischen Grades  
Doctor Rerum Naturalium (Dr. rer. nat.)



Vorgelegt dem Rat der Physikalisch–Astronomischen Fakultät  
der Friedrich–Schiller–Universität Jena

von Dipl.-Phys. SEBASTIAN MÜLLER  
geboren am 21.03.1983 in Dortmund

April 2010

1. Gutachter: Prof. Dr. ALEXANDER V. KRIVOV  
*Friedrich-Schiller-Universität Jena*
2. Gutachter: Prof. Dr. SEBASTIAN WOLF  
*Christian-Albrechts-Universität zu Kiel*
3. Gutachter: Prof. Dr. PHILIPPE THÉBAULT  
*Observatoire de Paris, Section de Meudon (Frankreich)*

Tag der Disputation: 19. Oktober 2010

*From our home on Earth, we look out into the distances and strive to imagine the sort of world into which we were born. With increasing distance our knowledge fades until at the last dim horizon we search among ghostly errors for landmarks scarcely more substantial. The search will continue. The urge is older than history. It is not satisfied and it will not be suppressed.*

EDWIN P. HUBBLE

Quelle des Titelbildes:  
[http://berkeley.edu/news/media/releases/2008/11/13\\_exoplanet.shtml](http://berkeley.edu/news/media/releases/2008/11/13_exoplanet.shtml)

# Contents

Kurzfassung . . . . .	v
Abstract . . . . .	vi
<b>1 Introduction</b>	<b>1</b>
1.1 Debris Disks in the Framework of Planet Formation . . . . .	1
1.2 Implications from Observations . . . . .	4
1.2.1 Photometry . . . . .	4
1.2.2 Spectroscopy . . . . .	5
1.2.3 Imaging . . . . .	6
1.2.4 Other Techniques . . . . .	6
1.3 Aim of This Study . . . . .	7
<b>2 Theory</b>	<b>8</b>
2.1 Basic Disk Definitions . . . . .	8
2.1.1 Disk Densities . . . . .	8
2.1.2 Total Disk Cross Section . . . . .	8
2.1.3 Optical Depth . . . . .	9
2.2 Scattering Theory . . . . .	9
2.2.1 Electrodynamics . . . . .	9
2.2.2 Spherical, Homogeneous Particles . . . . .	10
2.2.3 Spherical, Inhomogeneous Particles . . . . .	11
2.2.4 Refractive Indices . . . . .	12
2.3 Thermal Emission of Debris Disks . . . . .	13
2.3.1 Typical Units . . . . .	13
2.3.2 Debris Disks in Thermal Equilibrium . . . . .	14
2.4 Dynamics of Debris Disks . . . . .	15
2.4.1 Mechanisms in Debris Disks . . . . .	15
2.4.2 Collisions . . . . .	18
2.4.3 Kinetic Theory . . . . .	20
2.5 Evolution of Debris Disks . . . . .	21
2.5.1 The “Steady-State” Disk . . . . .	21
2.5.2 Scaling Laws . . . . .	21
<b>3 Numerical Tools</b>	<b>23</b>
3.1 Computation of the Collisional Evolution — ACE . . . . .	23
3.2 Computation of Thermal Emission Properties . . . . .	23
3.2.1 SEDUCE . . . . .	23
3.2.2 SUBITO . . . . .	25
3.2.3 Numerical Caveats . . . . .	25
<b>4 Classical Modeling</b>	<b>27</b>
4.1 The Classical Modeling Approach . . . . .	27
4.2 Application: HR 8799 . . . . .	28
4.2.1 The System . . . . .	28
4.2.2 Modeling Preparations . . . . .	29
4.2.3 Photometric Modeling . . . . .	29
4.2.4 Summary of the Results of Complementary Investigations . . . . .	33
4.2.5 Interpretation . . . . .	33

4.3	Discussion . . . . .	35
4.3.1	Advantages . . . . .	35
4.3.2	Caveats and Disadvantages . . . . .	35
<b>5</b>	<b>Modeling from the Sources</b>	<b>36</b>
5.1	The New Modeling Approach . . . . .	36
5.2	Application: Grid . . . . .	37
5.2.1	The Idea . . . . .	37
5.2.2	Reference Disks . . . . .	37
5.2.3	Results . . . . .	40
5.2.4	Modeling of Selected Debris Disks . . . . .	46
5.3	Application: Vega . . . . .	52
5.3.1	The Vega System . . . . .	52
5.3.2	The Reference Model . . . . .	56
5.3.3	Variation of Model Parameters . . . . .	61
5.3.4	Discussion . . . . .	72
5.4	Discussion . . . . .	76
5.4.1	Advantages . . . . .	76
5.4.2	Caveats and Disadvantages . . . . .	76
5.4.3	Possible Model Extensions . . . . .	77
<b>6</b>	<b>Conclusions</b>	<b>83</b>
6.1	Summary . . . . .	83
6.2	Comparison of the Two Approaches . . . . .	84
6.3	Outlook . . . . .	85
	<b>References</b>	<b>88</b>
	<b>Danksagung</b>	<b>101</b>
	<b>Ehrenwörtliche Erklärung</b>	<b>101</b>
	<b>Curriculum Vitae</b>	<b>102</b>

# Kurzfassung

Seit etwa 25 Jahren ist die Existenz von Trümmerscheiben um Hauptreihensterne, die als Überbleibsel der Planetenentstehungsphase betrachtet werden, bekannt. Sie bestehen aus subplanetaren Objekten, angefangen mit Planetesimalen von bis zu einigen 100 km Durchmesser, bis hin zu Staub, wovon allerdings nur der Staubanteil durch seine (thermische) Emission beobachtbar ist. Ironischerweise ist der beobachtbare Staub die kurzlebigste Komponente in Trümmerscheiben, und ist nur wegen einer ständigen Produktion durch die langlebigeren Planetesimale (z.B. durch gegenseitige Kollisionen) vorhanden. Damit enthalten Planetesimale wesentlich mehr Informationen über die Vergangenheit des Systems als der Staub.

In dieser Arbeit wird ein neuer, kollisionsbasierter Ansatz zur Modellierung von Trümmerscheiben vorgestellt, verdeutlicht und mit der traditionellen Modellierungsmethode verglichen. Die letztere Methode konzentriert sich allein auf den Staub, dessen räumliche und Teilchengrößevertelung durch Potenzgesetze angenähert werden. Zur Veranschaulichung dieses Herangehens wurde das Planetensystem HR 8799 ausgewählt. Zwei Staubkomponenten, eine warme innerhalb des innersten Planeten und eine kalte außerhalb des äußersten Planeten, sind notwendig, um die beobachtete thermische Emission zu erklären. Wie komplementäre Untersuchungen zeigen, ist dies in Übereinstimmung mit den stabilen Bereichen für Planetesimale.

Um auch die Planetesimalkomponente direkt mit einzubeziehen, wurde ein neuer Modellierungsansatz entwickelt, in dem die komplette Trümmerscheibe mit dem Programm ACE unter der Annahme einer kollisionsdominierten Entwicklung simuliert und die resultierende Staubverteilung zum Vergleich mit den Beobachtungsdaten verwendet wird. Da die Simulationen sehr zeitaufwendig sind, wird in der ersten Anwendung dieses Ansatzes ein Gitter von Referenzscheiben um sonnenähnliche Sterne erzeugt, das auf beobachtete Systeme angewendet werden kann, um schnell erste Ergebnisse zu bekommen. Die fünf aufgeführten Beispiele machen die Anwendbarkeit deutlich. Desweiteren wird die Trümmerscheibe um Wega als Anwendung für die neue Modellierungsmethode herangezogen. Eine detaillierte Untersuchung des Systems zeigt, dass — entgegen der Meinung einiger Autoren der letzten Jahren — die Beobachtungen sich mit einer kollisionsdominierten Scheibe im Gleichgewicht erklären lassen.

Der Vergleich zwischen den beiden vorgestellten Modellierungsarten macht deutlich, dass beide Methoden ihre Rechtfertigung haben und je nach Beobachtungslage eines bestimmten, zu untersuchenden Systems zum Einsatz kommen sollten.

# Abstract

Debris disks as the remnants of planet formation processes have been known to be a common feature around main-sequence stars for about 25 years now. They comprise solids ranging from planetesimals of up to several 100 km in diameter down to small dust. However, observations are only sensitive to thermal emission stemming from the disk's dust, which is, ironically, the most short-lived component. Only steady supply by planetesimals (e.g., by mutual collisions) can sustain the observed amount of dust. Information about the system's history is stored in planetesimals.

This work presents a new, collision-based way of modeling debris disks and compares it to the classical modeling approach. The latter procedure focuses on the disk's dust portion. Both, spatial and size distributions of dust are approximated by power-laws. For a demonstration the planetary system HR 8799 is chosen. To account for the observed thermal emission of this system two dust components, a warm ring inside the planets and a cold, outer component, are necessary. Complementary investigations reveal a good agreement with the location of stable regions for planetesimal evolution.

A new approach was developed to directly incorporate planetesimals into the model. The code ACE is used to model the complete debris disk under the assumption of a collision-dominated evolution. The resulting dust distribution can be used for comparison with observational data. Due to long computation times, this approach is adopted first to generate a grid of reference disks around sun-like stars. Applied to observed systems first conclusions can be drawn quickly. Five examples are given to demonstrate the applicability of the new approach. Furthermore, the archetypal Vega debris disk is modeled in-depth. Contrary to claims of different authors in recent years, investigations show that observations are well in agreement with the assumption that the Vega disk evolves in a collisional equilibrium.

Finally, both modeling approaches are compared. None of them can be assessed superior and each has its advantages and disadvantages. Depending on the state of observations towards a certain system to model the one or the other approach should be favored.



# Chapter 1

## Introduction

*God is infinite, so His universe must be too. Thus is the excellence of God magnified and the greatness of His kingdom made manifest; He is glorified not in one, but in countless suns; not in a single earth, a single world, but in a thousand thousand, I say in an infinity of worlds.*

GIORDANO BRUNO

### 1.1 Debris Disks in the Framework of Planet Formation

Although this statement may have been one of the reasons for his conviction by the Inquisition in Rome in the year 1600, seen from nowadays point of view, Giordano Bruno was not so wrong in interpreting the stars as sun-like objects (or the other way round: the sun as one among the innumerable stars). Also the existence of planets as a common feature for stellar systems has now been known for about 20 years. With such ideas, the Age of Enlightenment unclosed the need to find new answers to one of the oldest questions of mankind: “Where do we come from and where do we go?”

Scientifically, this draws back to the modern understanding of the formation of the sun and the earth, or more general, the formation of stars and planets. These processes have their origin in relatively dense and cool molecular clouds (e.g., Becklin & Neugebauer 1967; Lada 1992), which are agglomerations of interstellar material and mainly consist of gas with some fraction of dust (typically a ratio of 100 : 1 is assumed, see Hildebrand 1983). If densities are high enough, the region becomes unstable and gravitational collapse occurs (Bonnor 1956; Larson 1969). Further fragmentation creates a bunch of collapsing cores. In the centers of these cores, a protostar is formed first (Shu et al. 1993). It is surrounded by an envelope of primordial material. As confirmed by observations, molecular clouds exhibit inhomogeneities (Larson 1981; McKee & Ostriker 2007) transferring angular momentum to the collapsing regions. Thus, rotation is induced to the collapsing cores. Rotation causes the cores to flatten to a disk (Adams & Lin 1993). Such disks are the stage for the formation of planets.

A short glimpse at the solar system is sufficient to indicate that there cannot be a unique explanation of how planets are formed. The solar system comprises two kinds of planets, namely terrestrial planets in the inner part of the system and gas giants beyond. Constraints on formation time scales are set by one observational fact at least for gas giants: systems with ages of typically 3 – 10 Myr (depending on the primary mass) clear both, gas and dust disk within a rather short time (Currie 2010, and references therein). The clearing process takes about  $10^5$  yr (Simon & Prato 1995; Wolk & Walter 1996). However, recent studies suggest that the actual clearing time may be up to 1 Myr (Currie 2010). Within this period, first, indications for the presence of gas vanish and, second, optical thick dust emission becomes optically thin or ceases completely. Thus, disks in this clearing phase are called transitional disks.

Today, it is known that transitional disks form inner gaps and clear from inside out (Alexander 2008, and references therein). Recently, it was suggested that there also exists a second kind of transitional disks that loose their material homologously (Currie & Kenyon 2009; Currie 2010). Both types can be distinguished by analysis of dust emission. Gas can only be traced by its characteristics when being accreted to the central star. Most detections are therefore sensitive to gas inside  $\sim 0.1$  AU and it is unclear, whether some fraction of gas survives further away from the star for a longer period of time than the canonical values for the disk dispersal. Three effects are supposed to be responsible for the removal of gas. First, gas is gradually accreted to the protostar. Second, photoevaporation can occur, when the (proto)stellar UV radiation,

after the onset of nuclear fusion heats the disk surface. If the thermal energy of gas exceeds the gravitational binding energy, the resulting pressure gradient blows the gas out of the system (Begelman et al. 1983; Hollenbach et al. 1994; Clarke et al. 2001; Font et al. 2004). Last, formed (giant) planets can gravitationally open a gap in the disk, resulting in continued accretion interior to the planet (Alexander 2008, and references therein).

In the past two explanations for the formation of planets have been suggested. One possibility to easily form gas giants within the required time scale is similar to the formation of the star itself. If densities in the gas disk are high enough and sufficient cooling has taken place to reduce the sound speed, self gravity can provoke a gravitational collapse, which leads to the direct formation of a gas giant on very short time scales (Cameron 1978; Boss 1997; Rice et al. 2003).

A second scenario is the core accretion model (Safronov 1969). It assumes that, once a planetary core is grown large enough, gas accretion sets in creating a huge gas envelope (Perri & Cameron 1974; Pollack et al. 1996). The required core masses are of the order of  $10 M_{\oplus}$  (Mizuno 1980) (to keep an atmosphere, masses of  $\sim 0.1 M_{\oplus}$  are sufficient). In the first stage of gas accretion, the envelope is in a hydrostatic equilibrium until the envelope mass reaches the core mass. Then, a runaway gas accretion starts, which can only be stopped by the dispersal of the gas disk or the opening of a gap in the gas disk due to the growing planet (Pollack et al. 1996; Rice & Armitage 2003; Hubickyj et al. 2005; Alibert et al. 2005; Tanigawa & Ikoma 2007).

The mechanism for the formation of gas giant cores is closely connected to the formation of terrestrial planets. After the formation of planetesimals (possible processes will be discussed below), solid bodies up to some 10 km large grow by coagulation resulting in so-called oligarchs, which have gathered most of the material in their surrounding. The outcome of this agglomeration process is very sensitive to the location in the disk. In the inner part within only 0.01 – 1 Myr, 100 – 1000 km large bodies of  $10^{-2} - 10^{-1} M_{\oplus}$  (for solar-like systems) grow (Wetherill & Stewart 1993; Ida & Makino 1993; Kokubo & Ida 1996; Weidenschilling et al. 1997). However, it is impossible for the oligarchs to grow any further, as all available material is depleted (e.g., Raymond et al. 2006). Due to lower densities and longer orbital periods in the central part of the disk it takes 5 – 10 Myr until oligarchs have formed. In turn, the masses reach  $10 M_{\oplus}$  and more and are therefore sufficient for accretion of a gas envelope (e.g., Chambers 2008). In the outer parts of the disk very low densities and long orbital periods prevent from the formation of oligarchs.

Summarizing, while it seems possible to grow gas giant cores in the required time scale, terrestrial planets cannot be completed by coagulation of planetesimals. However, once the oligarchs have cleared their surrounding, eccentricities (kept low by dynamical friction with planetesimals) increase and the oligarchs start interacting with each other. This leads to a final assembly of a few planets within about 100 – 200 Myr (e.g., Raymond et al. 2006; O’Brien et al. 2006). In this phase, gravitational perturbations of outer giant planets may be of importance (e.g., Chambers & Wetherill 1998; Thébault & Brahic 1999; Thébault et al. 2002; Raymond et al. 2006).

Simulations dealing with the formation of planets in the solar system show a general agreement out to Saturn. However, it is questionable whether Uranus and Neptune can have formed in situ. A widely accepted scenario is that the protoplanets formed further inside and then gravitationally interacted with planetesimals in the outer disk. This results in an outward migration during which further accretion takes place so that finally the completed planets end up at their current location (Fernandez & Ip 1984).

Since an extrasolar planet has been detected for the first time (Campbell et al. 1988; Wolszczan & Frail 1992; Mayor & Queloz 1995), several hundred planetary candidates around other main-sequence stars have been found (detection limits are only slowly penetrating the level to find terrestrial planets similar to those in the solar system). Their properties differ significantly from the planets around the sun. In particular, there is a wide spread of planetary distances and eccentricities (Armitage 2010, and references therein). One curiosity is the finding of so-called hot

Jupiters, Jupiter-mass planets located at  $\sim 0.1$  AU. While it is already difficult to form gas giants at 1 AU (Bodenheimer et al. 2000), it appears almost impossible for hot Jupiters. This is another indication that the standard planet formation theory is not complete. One possible solution is the migration of the planet due to its interaction with the gas disk. Simulations show that after their formation in the outer disk, giant planets can migrate inward on short time scales ( $< 1$  Myr) (Lin & Papaloizou 1986; Chambers 2006). As a by-product, migration of massive planets can also excite their eccentricities (Papaloizou et al. 2001; D'Angelo et al. 2006). A major problem in this scenario is that migration will also affect oligarchs, who may therefore be lost before planetary cores can be formed (e.g., Chambers 2008). Only reduced migration rates allow the formation of gas giants (Alibert et al. 2005).

Fundamental for the planet formation models is the presence of planetesimals. Solid material is supposed to be present from the very beginning in the form of small dust. Within a few AU from the star, it takes only  $10^3 - 10^4$  yr for the dust to settle to the disk mid-plane. On its way, dust particles collide and stick together, so that in the end mm- to cm-size objects are formed (e.g., Safronov 1969; Dullemond & Dominik 2005; Brauer et al. 2008). With increasing size, further growth is hampered in two ways. First, larger grain sizes imply higher relative velocities, which at some point prevent further sticking (Blum & Wurm 2008). Second, with increasing size, particles are subject to rapid inward drift due to the interaction with the gas disk, culminating for  $\sim 1$  m objects. Thus, material is quickly removed without the chance of any further growth (e.g., Brauer et al. 2007, 2008). This issue is usually referred to as the meter barrier for planetesimal formation (Weidenschilling 1980). Recent work implies that even for relative velocities of  $\gtrsim 10$  ms $^{-1}$  net growth may be possible (e.g., Wada et al. 2009). Still, it remains questionable, whether such mechanisms are appropriate to produce planetesimals in the required time scale of  $10^5$  yr.

An alternative scenario that bypasses the bottle-neck of gradual growth picks up the idea of gravitational instability again (Toomre 1964). After dust has settled to the mid-plane, high densities — even increased by the radial drift of dust — may cause a collapse in the dust sub-disk leading to the rapid formation of 5 – 10 km sized planetesimals within about 10 AU (Safronov 1969; Goldreich & Ward 1973). A problem that might prevent the dust from collapsing is self-induced turbulence due to friction between the dust sub-disk and the gas disk (e.g., Cuzzi et al. 1993). However, additional instabilities (resulting in clumps, streams, spiral arms, etc.) are a possibility to create required over-densities (Johansen et al. 2007; Chiang 2008).

The only direct observational source of information for planetesimals is the solar system, where the formation processes have long finished and primordial gas is gone. Around other stars planetesimals remain invisible and can only be conjectured indirectly (see below). The remaining disk/rings in the solar system is/are what is called a debris disk, comprising (amongst others) the completed planetesimals that survived the planet formation phase and the planets. The leftover planetesimals around the sun gather in the asteroid belt between Mars and Jupiter and in the Edgeworth-Kuiper belt beyond the orbit of Neptune. However, only the largest among these objects can be considered primordial. Due to their shorter collisional lifetimes, smaller bodies stem from mutual collisions. Without the damping effect of gas in the disk relative velocities are high and lead to destructive collisions, rather than sticking or bouncing. Such events are connected to appreciable alteration of the planetesimal material (e.g., Davison et al. 2010, and references therein). Recent comparison between planetesimal formation and evolution models and the observed distribution of asteroids support the direct formation of large planetesimals with sizes of up to several hundred km, favoring the collapse scenario (Morbidelli et al. 2009).

Another component in the solar system's debris disk is dust, which can be observed in the inner part of the system by scattered solar light, producing the zodiacal light. This dust, however, is not a remnant from the planet and planetesimal formation processes (simple estimates show

that typical dust lifetimes are by several orders of magnitudes shorter than stellar ages) but must have been produced rather recently, e.g., by mutual, fragmenting collisions of planetesimals or other erosive mechanisms (justifying the name debris disk, Backman & Paresce 1993). Dust production is not unique to the solar system. Debris disks have been observed around other main-sequence stars by the dust's excess emission over the expected stellar photosphere. Since the first detection (Aumann et al. 1984), several hundreds of such systems have been found. Except planets, which could have been detected in some cases, the dust emission is the only signpost of the formation processes in the early history of these systems. In order to draw conclusions on the planetesimals and their formation, it is therefore essential to understand the effects working on the observable dust.

## 1.2 Implications from Observations

Debris disks mainly show up by the dust's emission. In principle there are two ways of emission: dust particles scatter stellar light directly, or they absorb and reemit it at longer wavelengths. While scattered light is naturally the brightest around the stellar emission maximum, the reemitted thermal emission peaks at much longer wavelengths in the far-infrared (IR) with typical dust temperatures between 200 and 20 K. In order to detect debris disks successfully, it is important that the central star is faint enough so that it does not outshine the disk. This limits possible observations to wavelengths starting in the near-IR (or shortly below). Unfortunately, due to water absorption, the Earth atmosphere is relatively opaque at these wavelengths and only few windows in the near-IR, mid-IR, and sub-mm allow earth-based observations. Thus, most information gathered so far comes from space- or airborne missions.

Different types of observations are possible. In the following, the three most successful methods are introduced and the most important results summarized.

### 1.2.1 Photometry

Historically the first and most successful detection method for debris disks is IR-photometry. If an observation only measures the total flux of an astronomical object at a given wavelength (or to be precise: in a limited wavelength band), astronomers talk of a photometric observation. Like in the first debris disk discovery, a disk is traced by the excess it produces over the stellar photosphere. This, however, unveils an important limitation for photometry: due to the limited sensitivity of telescopes, excesses can only be detected if a certain contrast between disk and stellar emission is given. Thus, observations are usually performed far beyond the maximum of the stellar spectrum, starting in the mid-IR. As a consequence, photometry typically probes thermal emission rather than scattered light.

Since the first detection of a dust disk around the A0 star Vega with the *IRAS* satellite several hundreds of such Vega-like stars have been found. Especially the *Spitzer Space Telescope* (short: *Spitzer*) lifted knowledge about debris disks to a new level. Numerous surveys, mainly concentrating on the 24 and 70  $\mu\text{m}$  bands, namely for FGK stars a GTO (Beichman et al. 2005b; Bryden et al. 2006; Beichman et al. 2006b) and the FEPS Legacy program (Meyer et al. 2004; Kim et al. 2005; Meyer et al. 2006; Hillenbrand et al. 2008; Carpenter et al. 2009), for A stars a GTO project (Rieke et al. 2005; Su et al. 2006), surveys for young clusters (Gorlova et al. 2007; Siegler et al. 2007), and a binary program (Trilling et al. 2007), provided the possibility of various statistical analysis.

Nowadays it is known that on average about 15% of main-sequence stars host a detectable debris disk (Su et al. 2006; Siegler et al. 2007; Trilling et al. 2008; Hillenbrand et al. 2008). Their fractional luminosities (the ratio of dust to stellar luminosity) reaches up to values of  $10^{-5}$  to  $10^{-3}$ , which is supposed to be 2 (Vitense et al. 2010) to 4 (Booth et al. 2009) orders of magnitude above the presumed value for the current Kuiper belt. It was further found out that

the incidence of an excess strongly depends on the star's spectral type. While an outer disk at several 10 AU around A-type stars, implied by excesses at 24 and 70  $\mu\text{m}$ , was detected for 33% of the investigated stars (Su et al. 2006), the fraction decreases to 16% for stars of spectral type F0 to K0 (sun-like stars) (Beichman et al. 2006b; Bryden et al. 2006; Trilling et al. 2008). A 24  $\mu\text{m}$  excess, indicative for dust inside 10 AU around sun-like stars, was found for 4% of the investigated star sample (Trilling et al. 2008). Inner disks around A stars emit most efficiently short-ward of 24  $\mu\text{m}$  where the stellar photosphere is still very prominent, what hampers the detectability of such systems. Coming to even later-type stars, only up to 4% of observed K and M stars show an excess in the IR (Plavchan et al. 2005; Beichman et al. 2006b; Rhee et al. 2007; Gautier et al. 2007; Trilling et al. 2008; Plavchan et al. 2009). However, due to the lower temperatures detection at longer wavelength may be more efficient. Indeed, detection rates for K and M-type stars in the sub-mm and radio are slightly higher (Lestrade et al. 2006, 2009).

To derive dust masses, long-wavelength observations are more suitable as they typically trace larger particles which contribute most to the (dust) disk mass. Typical results lie within  $10^{-3} - 10^0 M_{\oplus}$  (earth masses).

An important parameter for the detection frequency of a debris disk is the age of the central star. A stars of about 10 Myr show a detection rate of some 60%, which decreases to about 10% for 600 Myr old systems (Siegler et al. 2007). Similarly, while warm dust was detected for about 20 – 40% of solar-type stars at 20 Myr, only few percent show excess at ages  $\gtrsim 1$  Gyr (Siegler et al. 2007; Meyer et al. 2008; Carpenter et al. 2009). Different studies investigated the evolution of observed emission finding an overall decay  $\propto t^{-\xi}$  of the dustiness with power-law indices up to 1 (Greaves & Wyatt 2003; Liu et al. 2004; Greaves 2005; Moór et al. 2006; Rieke et al. 2005). This is what is expected from dynamical models for collision dominated disks (Dominik & Decin 2003; Wyatt et al. 2007b; Löhne et al. 2008).

As debris disks are believed to be the final product of planet formation, it is natural to check for possible correlation with the incidence of planet detection in these systems. Results are still controversial (Greaves et al. 2004, 2006; Beichman et al. 2005b, 2006b; Moro-Martín et al. 2007; Kóspál et al. 2009; Bryden et al. 2009). Still, fractional luminosities around planetary host stars, at least for A stars, are expected to be brighter (Wyatt et al. 2007c,a). Statistics for solar-type stars slightly show such a trend, although they are not yet statistically significant (Bryden et al. 2009). What is rather statistically confirmed is that the detection of a debris disk is not correlated with the stellar metallicity (Greaves et al. 2006; Beichman et al. 2006b; Bryden et al. 2009).

## 1.2.2 Spectroscopy

Still considering the total flux of an astronomical object, but narrowing the band and taking a huge number of flux measurements at close-by wavelengths leads to the field of spectroscopy, or photospectroscopy. This method can be used complementary to photometry at about 24  $\mu\text{m}$  to detect warm dust around solar-type stars. Furthermore, spectroscopy is most useful to unravel the composition of observed dust as different types of dust produce different features in the observed spectrum. From small objects in the solar system it is known that much of the material is made of rocks — silicates like forsterite, fayalite, or olivine. Thus, the most promising spectral range is the mid-IR, where silicates show very prominent emission bands. Besides that, the excess is expected to rise over the stellar photosphere in the mid-IR. The exact knowledge of this part of the SED gives important insight into the highest temperatures in the disk, from which conclusions on the distance and grain size of dust can be drawn.

For more than a decade different facilities have taken spectra of debris disk systems from the near- to the mid-IR (e.g., Sloan et al. 2003; Gaidos & Koresko 2004; Honda et al. 2004; Schütz et al. 2005). However, not until *Spitzer/IRS (Infrared Spectrometer)* a systematic search for excesses due to warm dust around main-sequence stars became possible. A big search campaign

led to the conclusion that  $\sim 12\%$  of solar-type stars show excesses in the long wavelength *IRS* band (30 – 34  $\mu\text{m}$ ) (Beichman et al. 2006a; Lawler et al. 2009) while in the short wavelength band (8.5 – 12  $\mu\text{m}$ ) this is only the case for 1% of the observed stars. This gives an upper limit for typical dust temperatures of about  $\sim 500$  K. More than 80% of stars with excesses in the *IRS* range also reveal cold emission in the far-IR (Hillenbrand et al. 2008; Lawler et al. 2009).

Most near-IR spectra of systems with warm dust are relatively featureless indicating cold, large dust grains. There are only a few exceptions with a spectrum which exhibits various features. These can be attributed to a large set of different dust species (e.g., Lisse et al. 2007, 2008a,b, 2009). However, analysis is challenging due to the large number of degeneracies. The most popular example of such an exotic system is HD 69830 (Beichman et al. 2005a). The detection of three massive planets within 1 AU from the star makes this system very special. What is more, the excess decreases quickly towards longer wavelengths so that no excess emission could be measured at 70  $\mu\text{m}$ . The origin of these extraordinary features is still unclear.

### 1.2.3 Imaging

Resolved observations are the most direct way to reveal information about the structure of debris disks. Since recent years the number of resolved disks has steadily been increasing showing a vast variety of disk morphologies at different wavelengths. As a result of their scattering properties (see, e.g., Fig. 5.2) each spectral region is sensitive to a certain range of grain sizes. As will be explained in more detail in Chapter 2.4 and Chapter 5, particles of different sizes are subject to different physical processes, leading to a size segregation in the disk that can be observed at different wavelengths. While larger particles are bound to the region of their creation, smaller particles can spread over a wide range of distances or may even be removed from the system. Measurements at longer wavelengths (sub-mm) are more sensitive to cooler, typically larger particles, representative for the location of dust-producing planetesimals. The images mostly reveal structured disks, showing for example rings or clumps. However, when coming to the mid- and far-IR, thermal emission of smaller dust grains is probed. Such particles are highly affected by stellar radiation pressure and can therefore leave their birth region. The same disk may appear larger and mostly featureless (e.g., Su et al. 2005, 2009). Thermal emission at even shorter wavelengths traces back to the hottest particles in the disk, which are concentrated close to the star, where they are produced by the planetesimals. Images again show narrow ringlike structures (see Krivov 2010, Fig. 3).

Also resolved observations in the visual and near-IR, sensitive to scattered light of small bound dust, were successfully indicating the presence of inner cavities. (e.g., Ardila et al. 2004; Kalas et al. 2008; Marois et al. 2008). Some images exhibit different kinds of asymmetry and structure (e.g., Stapelfeld et al., in prep; Kalas & Jewitt 1995).

Several explanations for the afore mentioned structures can be found. The most natural, however, is that the disk is gravitationally perturbed by planets in the system (e.g., Mouillet et al. 1997; Augereau et al. 2001; Moro-Martín & Malhotra 2003; Moro-Martín et al. 2005; Faber & Quillen 2007). Thus, analyzing observed disk structures can also serve as a method to predict extrasolar planets (e.g., Moro-Martín et al. 2005; Zuckerman & Song 2004; Freistetter et al. 2007).

### 1.2.4 Other Techniques

With improvements in instrumentation, also other observation techniques came to the fore. Measurements of the disk's polarization have become possible in case of some systems (Krivova et al. 2000; Hildebrand & Kirby 2004). Using near-IR interferometry, it was possible to detect dust in the very inner parts of a few systems (e.g., Vega,  $\tau$  Cet, Fomalhaut) with typical masses of about  $10^{-7} M_{\oplus}$ , which appears as a lack of visibility (Absil et al. 2006, 2008; di Folco et al. 2007;

Akeson et al. 2009; Stark et al. 2009). Such dust structures are usually referred to as exozodiacal dust clouds. Their frequencies are expected to be some 20% (Absil et al., in prep.) for AFGKM stars.

### 1.3 Aim of This Study

This work presents and applies two ways of modeling debris disks. First, the classical modeling approach considers analytical functions to emulate the distribution of the disk's dust population. Calculating the observables it is straight forward to accurately fit the model parameters to observational data. This method is independent of any assumptions about physical mechanisms working on dust or planetesimals. Still, subsequent interpretation of the fitting results in the light of underlying processes in the disk is necessary. Second, which is the main focus of this work, a new modeling approach is derived. In contrast to the classical approach, this method is based on the physical effects on the dust and planetesimal population. Numerical simulations of the complete disk's collisional evolution provide disk models for which thermal emission properties can be calculated and compared to observations. The approach thus aims in directly constraining real physical parameters of the disk and its constituents, ranging self-consistently from sub-micron dust particles to planetesimals of hundreds of km. It therefore allows a more complete picture of debris disks and their (collisional) evolution and, consequently, naturally links the debris disk to earlier stages of disk evolution.

This is of special interest in the light of current uncertainties concerning the planetesimal formation. Both scenarios presented in Chapter 1.1 are expected to generate different distributions of planetesimals, which will most likely impact on the subsequent disk evolution. In particular, given that initially planetesimals are large, as it is expected from the rapid formation scenario, the amount of dust should be much smaller in the early evolution. This is because the longer period of planetesimal accretion with its steady dust production is bridged.

Beyond that, planets formed at earlier phases can affect debris disks in different observable ways, like stirring the planetesimals' eccentricities, clearing parts of the disk, producing clumps, warping the disk, etc (Wolf et al. 2007; Wolf 2008). Thus, understanding such mechanisms allows to draw conclusions on the presence of planets and their properties that are out of reach for conventional planet detection techniques. Similar investigations modeling dust emission of younger, protoplanetary disks have been proposed (Wolf et al. 1999) and applied to account for the detection of (proto-)planets and their formation processes (e.g., Wolf et al. 2003, 2008; Muzerolle et al. 2009; Cieza et al. 2010). If, in contrast, planets have already been found in a specific system, analyzing the dust emission will help constraining the whole structure and interaction between the system's different components, from the dust to the planets and the planetesimals. This will provide the possibility of setting the solar system in context to the global picture of planet formation and the subsequent evolution. To sum up, debris disk modeling is promising of deepening the insight into the formation of planetary systems, in particular the solar system.

After an introduction to the underlying processes of the dust's light emission and disk dynamics in Chapter 2 and the presentation of used numerical tools in Chapter 3, Chapter 4 summarizes the classical way of modeling debris disks and gives a brief example of its applicability. In Chapter 5 the new approach of debris disk modeling developed in the last three years is presented. Finally, advantages and disadvantages are discussed and a future prospect is given in Chapter 6.

# Chapter 2

## Theory

*In my opinion nothing occurs contrary to nature except the impossible, and that never occurs.*

GALILEO GALILEI

### 2.1 Basic Disk Definitions

#### 2.1.1 Disk Densities

The distribution of dust and planetesimals is mathematically described by disk densities that give the amount of material in the infinitesimally small interval of particle size  $[s; s + ds]$  and distance to the star  $[r; r + dr]$ . Densities describe the size distribution from a minimal size  $s_{\min}$  up to the largest planetesimals of several ten to some hundreds of kilometers. However, larger objects make a vanishing contribution to thermal emission. Typically, only grains with  $s \lesssim 1\text{mm}$  are observable. They are called dust. Besides that, the disk is usually assumed to be spatially limited to the region  $[r_{\min}; r_{\max}]$ .

Principally, disk densities are functions of grain size  $s$ , of location in the disk  $r$ , of azimuthal angle  $\theta$ , and of height  $h$ . However, as all disks considered in this work are axially symmetric and optically thin,  $\theta$  and  $h$  can be neglected. For subsequent calculations, the surface number density  $N(r,s)$  will be mainly applied. It has the units  $[N(r,s)ds] = \text{cm}^{-2}$ . Moreover, other related densities are employed by different authors. The most common densities are the cross section density  $\Sigma(r,s)$  and the number density  $n(r,s)$  which are connected to the surface number density as

$$\Sigma(r,s)ds = \pi s^2 N(r,s)ds \quad (2.1)$$

$$N(r,s)ds = 2r \sin \varepsilon n(r,s)ds, \quad (2.2)$$

with the disk's semi-opening angle  $\varepsilon$  and units  $[\Sigma(r,s)ds] = \text{cm}^2 \text{cm}^{-2}$  and  $[n(r,s)ds] = \text{cm}^{-3}$ .

Another density that will occur mainly in the context of simulated disks is the cross section density per unit size decade  $A$  with units  $[A(r,s)ds] = \text{cm}^2 \text{cm}^{-3}$ . It is defined as

$$A(r,s)ds = s \ln(10) \cdot \Sigma(r,s)ds. \quad (2.3)$$

#### 2.1.2 Total Disk Cross Section

For some applications the disk's total cross section  $S_{\text{dust}}$  is of interest. It equates

$$S_{\text{dust}} = \int_{r_{\min}}^{r_{\max}} dr \int_{s_{\min}}^{s_{\max}} ds \pi s^2 N(r,s), \quad (2.4)$$

where  $s_{\max}$  is the largest size that can appreciably contribute to the disk's cross section and therefore to its emission. It is typically chosen as  $s_{\max} = 1\text{mm}$ .

Consider the dust's surface number density follows a distribution of the kind  $N(r,s) = N_0 \left(\frac{r}{r_0}\right)^{-\xi} \left(\frac{s}{s_0}\right)^{-\eta}$ , with power-law indices  $\xi$  and  $\eta$ , and normalization factors  $r_0$  and  $s_0$  for the spatial and grain size distribution, respectively. The connection between the power-law constant



$N_0$  and the total disk cross section can then be expressed as

$$N_0 = \frac{S_{\text{dust}}}{r_0^2 s_0^3} \frac{(2 - \xi) \cdot (3 - \eta)}{2\pi^2} \left[ \left( \frac{r_{\text{max}}}{r_0} \right)^{2-\xi} - \left( \frac{r_{\text{min}}}{r_0} \right)^{2-\xi} \right]^{-1} \\ \times \left[ \left( \frac{s_{\text{max}}}{s_0} \right)^{3-\eta} - \left( \frac{s_{\text{min}}}{s_0} \right)^{3-\eta} \right]^{-1}. \quad (2.5)$$

In this case, the total dust mass  $M_{\text{dust}}$  can also be calculated using the total disk cross section

$$M_{\text{dust}} = \frac{4\rho}{3} s_0 S_{\text{dust}} \frac{3 - \eta \left( \frac{s_{\text{max}}}{s_0} \right)^{4-\eta} - \left( \frac{s_{\text{min}}}{s_0} \right)^{4-\eta}}{4 - \eta \left( \frac{s_{\text{max}}}{s_0} \right)^{3-\eta} - \left( \frac{s_{\text{min}}}{s_0} \right)^{3-\eta}}. \quad (2.6)$$

### 2.1.3 Optical Depth

The geometrical optical depth (for reasons of brevity from now on only optical depth) is the ratio of the material's cross section to the corresponding disk area

$$\tau = \frac{A_{\text{dust}}}{A_{\text{disk}}}. \quad (2.7)$$

In general, this has to be calculated along the observer's line of sight. For simplicity consider the disk to be observed edge-on. In polar coordinates with azimuthal angle  $\theta$  the line of sight can be expressed as  $r(R, \theta) = R(\cos \theta)^{-1}$  with a projected distance to the star  $R$ . Then the optical depth reads

$$\tau(R) = 2\pi R \int_0^{\theta_{\text{max}}} d\theta (\cos \theta)^{-2} \int_{s_{\text{min}}}^{s_{\text{max}}} ds s^2 n(r(R, \theta), s). \quad (2.8)$$

Due to the assumed symmetry, the  $\theta$  integration runs between 0 and  $\theta_{\text{max}} = \arccos(R/r_{\text{max}})$ .

The calculation is even more simplified, if the pole-on optical depth is of interest:

$$\tau(r) = \pi \int_{s_{\text{min}}}^{s_{\text{max}}} ds s^2 N(r, s). \quad (2.9)$$

## 2.2 Scattering Theory

Explanations for the derivation of Mie theory and effective medium theory as presented below are basically taken from Bohren & Huffman (1983).

### 2.2.1 Electrodynamics

Fundamental to electrodynamics are the four Maxwell equations. Together with the two material equations they are sufficient to explain any (classical) phenomenon connected to electrical charges and electric and magnetic fields. For almost 150 years it has been known that under the assumption of a plane wave for the electric and magnetic field  $\mathbf{E}$  and  $\mathbf{H}$ , respectively,

$$\mathbf{E}(\mathbf{r}) = \mathbf{E}_0 e^{i(\mathbf{k}\mathbf{r} - \omega t)} \quad (2.10)$$

$$\mathbf{H}(\mathbf{r}) = \mathbf{H}_0 e^{i(\mathbf{k}\mathbf{r} - \omega t)} \quad (2.11)$$

with the complex wave vector  $\mathbf{k}$ , the frequency  $\omega = 2\pi c/\lambda$ , the speed of light  $c$ , and the wavelength  $\lambda$ , the equations can be solved. It is easy to show that the norm of the wave vector — the

wave number  $k$  — can be expressed as

$$k = k' + ik'' = \frac{\omega N}{c}, \quad (2.12)$$

using the refractive index

$$N = n + i\kappa = c\sqrt{\varepsilon\mu}, \quad (2.13)$$

where  $\varepsilon$  is the (complex) dielectric function and  $\mu$  the permeability. Then, the Maxwell equations decouple resulting in two wave equations for the two fields.

In the next step the energy balance of a single particle exposed to an incident electromagnetic wave is considered. Usually the Poynting-vector

$$\mathbf{S} = \text{Re}(\mathbf{E}) \times \text{Re}(\mathbf{H}) \quad (2.14)$$

is introduced, describing the electromagnetic field's energy flux. Taking an imaginary sphere of surface  $A$  and normal vector  $\mathbf{e}_r$  surrounding the particle, the energy streaming through the surface is given by

$$W^{\text{abs}} = - \int_A \mathbf{S} \cdot \mathbf{e}_r dA. \quad (2.15)$$

Provided the particle does absorb only and no energy is produced inside the sphere, it is  $W^{\text{abs}} > 0$ , and the absorbed energy can be split into three contributions

$$W^{\text{abs}} = W^{\text{i}} - W^{\text{sca}} + W^{\text{ext}}. \quad (2.16)$$

The different contributions are the incident energy  $W^{\text{i}} = - \int_A \mathbf{S}^{\text{i}} \cdot \mathbf{e}_r dA$ , the scattered energy  $W^{\text{sca}} = \int_A \mathbf{S}^{\text{sca}} \cdot \mathbf{e}_r dA$ , and the extinct energy  $W^{\text{ext}} = - \int_A \mathbf{S}^{\text{ext}} \cdot \mathbf{e}_r dA$ . Assuming the medium surrounding the particle is non-absorbing ( $N_{\text{med}} = 1$ ), all absorption stems from the particle and  $W^{\text{i}}$  vanishes.

Denote the incident intensity by  $I_{\text{i}}$ , then the cross sections for extinction, scattering, and absorption are defined as

$$C^{\text{ext}} = \frac{W^{\text{ext}}}{I_{\text{i}}}, \quad C^{\text{sca}} = \frac{W^{\text{sca}}}{I_{\text{i}}}, \quad C^{\text{abs}} = \frac{W^{\text{abs}}}{I_{\text{i}}}, \quad (2.17)$$

respectively. Following Eq. (2.16) this implies

$$C^{\text{ext}} = C^{\text{abs}} + C^{\text{sca}}. \quad (2.18)$$

The efficiencies for extinction, scattering and absorption are defined as

$$Q^{\text{ext}} = \frac{C^{\text{ext}}}{G_{\text{g}}}, \quad Q^{\text{sca}} = \frac{C^{\text{sca}}}{G_{\text{g}}}, \quad Q^{\text{abs}} = \frac{C^{\text{abs}}}{G_{\text{g}}}, \quad (2.19)$$

with the particle's cross section  $G_{\text{g}}$  projected to an area perpendicular to the incident light. For spherical grains this is simply  $G_{\text{g}} = \pi s^2$ .

## 2.2.2 Spherical, Homogeneous Particles

It is impossible to solve the wave equation for a general geometry analytically. Therefore, it is necessary to make simplifying assumptions. The easiest geometry is a spherical, homogeneous, and isotropic particle. In this case, an analytical solution was found by Gustav Mie in 1908. A

longer derivation showed that the scattering and extinction cross sections can be written as

$$C^{\text{sca}} = \frac{2\pi}{k^2} \sum_{n=1}^{\infty} (2n+1) (|a_n|^2 + |b_n|^2) \quad (2.20)$$

$$C^{\text{ext}} = \frac{2\pi}{k^2} \sum_{n=1}^{\infty} (2n+1) \text{Re}(a_n + b_n), \quad (2.21)$$

with the scattering coefficients  $a_n$  and  $b_n$ . Using the Bessel functions of first and second kind  $J_n$  and  $Y_n$ , the spherical Bessel functions read

$$j_n(\rho) = \sqrt{\frac{\pi}{2\rho}} J_{n+\frac{1}{2}}(\rho) \quad \text{and} \quad h_n(\rho)^{(1)} = j_n(\rho) + iy_n(\rho), \quad (2.22)$$

with  $y_n(\rho) = \sqrt{\frac{\pi}{2\rho}} Y_{n+\frac{1}{2}}(\rho)$ . Then, the scattering coefficients can in principle be expressed through the Riccati-Bessel functions

$$\psi_n(\rho) = \rho j_n(\rho) \quad \text{and} \quad \xi_n(\rho) = \rho h_n^{(1)}(\rho). \quad (2.23)$$

However, for computational purposes it is more convenient to make use of the logarithmic derivative

$$D_n(\rho) = \frac{d}{d\rho} \ln \psi_n(\rho) \quad (2.24)$$

that can be obtained by recursion via

$$D_{n-1}(\rho) = \frac{n}{\rho} - \frac{1}{D_n(\rho) + \frac{n}{\rho}}. \quad (2.25)$$

Finally, the scattering coefficients can be calculated as

$$a_n = \frac{\left[ \frac{D_n(mx)}{m} + \frac{n}{x} \right] \psi_n(x) - \psi_{n-1}(x)}{\left[ \frac{D_n(mx)}{m} + \frac{n}{x} \right] \xi_n(x) - \xi_{n-1}(x)} \quad (2.26)$$

$$b_n = \frac{\left[ mD_n(mx) + \frac{n}{x} \right] \psi_n(x) - \psi_{n-1}(x)}{\left[ mD_n(mx) + \frac{n}{x} \right] \xi_n(x) - \xi_{n-1}(x)}. \quad (2.27)$$

The parameters in the functions are the size parameter  $x = 2\pi s N_{\text{med}}/\lambda$  and the relative refractive index  $m = N/N_{\text{med}}$ , with the refractive index of the surrounding medium  $N_{\text{med}}$ .

Named after its inventor, this approach is called Mie theory.

### 2.2.3 Spherical, Inhomogeneous Particles

Dropping the assumption of the particle being homogeneous causes severe problems when trying to solve the scattering problem analytically. One widely used approach to overcome these problems is to “create” new materials that show the same properties as inhomogeneous materials. Then, refractive indices of the new species can be used to model the scattering properties in the framework of Mie theory. This approach is usually called effective medium theory.

The effective medium theory describes the scattering properties of a inhomogeneous particle by a homogeneous particle with an effective dielectric function  $\epsilon^*$ . This is achieved by averaging

the material equation over the whole inhomogeneous particle and yields

$$\langle \mathbf{D}(\mathbf{r}, \lambda) \rangle = \varepsilon^* \langle \mathbf{E}(\mathbf{r}, \lambda) \rangle, \quad (2.28)$$

for the dielectric displacement  $\mathbf{D}(\mathbf{r}, \lambda)$  and the electric field  $\mathbf{E}(\mathbf{r}, \lambda)$ . The following relations were derived for objects made up of a matrix contaminated by a bunch of inclusions in the Rayleigh limit. This means that the inclusions must be small compared to the wavelength.

Consider  $N$  species of inclusions with the dielectric functions  $\varepsilon_i^\sigma$ , where  $\sigma = 1 \dots N$  stands for the inclusion type with a total volume  $V^\sigma$  and  $i = 1, 2, 3$  for the considered direction. The dielectric function for the environment of every inclusion is denoted by  $\varepsilon_0$ . The averaging procedure finally leads to the expression

$$\varepsilon^* - \varepsilon_0 = \frac{\sum_{\sigma=1}^N \sum_{i=1}^3 f^\sigma \varepsilon_0 \frac{\alpha_i^\sigma}{V^\sigma}}{\sum_{\sigma=1}^N \sum_{i=1}^3 f^\sigma \frac{\varepsilon_0}{\varepsilon_i^\sigma - \varepsilon_0} \frac{\alpha_i^\sigma}{V^\sigma}}. \quad (2.29)$$

Maxwell-Garnett assumed that the inclusions are embedded separately in a low concentration in a matrix (so that they cannot interact). This is equivalent to  $\varepsilon_0 = \varepsilon_m$ , with  $\varepsilon_m$  the dielectric function of the matrix, leading to

$$\varepsilon^* - \varepsilon_m = \frac{\sum_{\sigma=1}^N \sum_{i=1}^3 \frac{1}{3} f^\sigma \varepsilon_m \frac{\alpha_i^\sigma}{V^\sigma}}{1 - \sum_{\sigma=1}^N f^\sigma \left( 1 - \frac{1}{3} \sum_{i=1}^3 \frac{\varepsilon_m}{\varepsilon_i^\sigma - \varepsilon_m} \frac{\alpha_i^\sigma}{V^\sigma} \right)}. \quad (2.30)$$

Decreasing the complexity of the inclusions implies

$$\varepsilon^* - \varepsilon_m = \left[ \frac{3f \left( \frac{\varepsilon - \varepsilon_m}{\varepsilon + 2\varepsilon_m} \right)}{1 - f \left( \frac{\varepsilon - \varepsilon_m}{\varepsilon + 2\varepsilon_m} \right)} \right] \quad (2.31)$$

for one species of spherical, uncoated, isotropic inclusions with dielectric function  $\varepsilon$ . It is obvious that the choice of the matrix and the inclusion material is important as the equation is not invariant to an exchange.

Besides the Maxwell-Garnett theory, several other mixing rules have been developed (for an overview see, e.g., Ossenkopf 1991). This work, however, only uses the specialization presented above. As shown by Kolokolova & Gustafson (2001), effective medium theory has to be considered with caution. Their comparison between laboratory work and theoretical predictions show that any mixing rule only provides satisfactory results for inclusion fractions of up to 10%.

## 2.2.4 Refractive Indices

For simplicity in the course of this work, the dust particles are assumed to be non-magnetic. This provides an easy way for the calculation of dielectric functions  $\varepsilon = \varepsilon' + i\varepsilon''$  from refractive indices:

$$\varepsilon' = n^2 - \kappa^2 \quad (2.32)$$

$$\varepsilon'' = 2n\kappa. \quad (2.33)$$

Thus, the inverse transformation reads

$$n = \sqrt{\frac{\sqrt{\epsilon'^2 + \epsilon''^2} + \epsilon'}{2}} \quad (2.34)$$

$$\kappa = \sqrt{\frac{\sqrt{\epsilon'^2 + \epsilon''^2} - \epsilon'}{2}}. \quad (2.35)$$

This conversion is important, as effective medium theory is put in terms of the dielectric function, while optical properties of different materials are usually given as refractive index.

In principle it is of course possible to calculate optical data from a given atomic or molecular structure of a solid body (this is already subject to any introductory course in solid state physics), however real materials are too complex to be handled with the desired accuracy. Thus, for decades laboratory measurements, using different methods and setups for different materials and spectral regimes, provided the most reliable results on optical properties (see, e.g., Koike et al. 2003; Tamanai et al. 2006).

The presence of gas and dust between stars has been commonly known for a long time as it absorbs, scatters, reemits, polarizes and changes the color of stellar light from the surrounding sky area. Especially observations of polarization and absorption bands of the so-called interstellar medium (ISM) lead to the conclusion that the material must basically have a dielectric character (like ice, dirty ice, or silicates), rather than a metallic one (like graphite or iron, e.g., Martin 1973). Draine & Lee (1984) used measured absorption features to design refractive indices in order to reproduce the observations. The new artificial material was called “astronomical silicate” (short: astrosil) because it was based on amorphous silicates. It can be regarded as some dirty rock, contaminated with ice, iron, carbons, and other impurities. In subsequent years, the model was further improved and extended (Draine 1985; Laor & Draine 1993; Draine 2003b,a).

In recent years, astrosil has become a standard choice when modeling thermal emission properties of circumstellar dust. However, mid-IR spectra of disks around young Herbig Ae/Be stars (e.g., Malfait et al. 1998; Meeus et al. 2001), evolved stars (e.g., Molster et al. 2002), and even main-sequence stars (e.g., Jura et al. 2004; Beichman et al. 2005a; Chen et al. 2006; Lawler et al. 2009) reveal several features indicating crystalline silicates. Different methods have been developed to reproduce the observed spectra making use of laboratory work (e.g., Olofsson et al. 2009; Lisse et al. 2009). Besides that, recent SED modeling efforts of solar-type debris disk systems suggest the need to include ice, as pure astrosil emission tends to be too warm (Krivov et al. 2008; Tanner et al. 2009; Augereau et al. in prep.; Reidemeister et al. 2010).

Although all these approaches still have severe shortcomings and results on the real composition of observed dust need to be taken with caution, they clearly show that the assumption of amorphous astrosil can only be a first approximation.

## 2.3 Thermal Emission of Debris Disks

### 2.3.1 Typical Units

In terms of debris disk studies, fluxes are typically presented as a function of wavelength ( $[\lambda] = \mu\text{m}$ ). Thus, the corresponding flux has the units  $[F_\lambda] = \text{erg s}^{-1}\text{cm}^{-2}\text{\AA}^{-1}$ . Ironically, fluxes are usually given in units of frequency with the most common unit Jy (read: Jansky,  $1 \text{ mJy} = 10^{-26} \text{ erg s}^{-1}\text{cm}^{-2}\text{Hz}^{-1}$ ). Conversion between both types of fluxes is given by

$$F_\nu = \frac{\lambda^2}{c} F_\lambda. \quad (2.36)$$

### 2.3.2 Debris Disks in Thermal Equilibrium

Objects in the surrounding of a star scatter and absorb stellar radiation. Absorbed flux is reemitted as thermal emission. Assuming that absorption and reemission are in an equilibrium, the particle's distance to the star becomes a function of its temperature  $T_g$ :

$$r = \frac{R_*}{2} \sqrt{\frac{\int_0^\infty d\lambda C_\lambda^{\text{abs}}(s) F_{\lambda,*}(T_*)}{\int_0^\infty d\lambda C_\lambda^{\text{abs}}(s) B_\lambda(T_g)}}. \quad (2.37)$$

Here,  $R_*$  and  $F_{\lambda,*}(T_*)$  denote the stellar radius and emission at wavelength  $\lambda$ , respectively,  $T_*$  the stellar temperature,  $B_\lambda(T)$  is the Planck function, and  $C_\lambda^{\text{abs}}(s)$  is the absorption cross section. For calculating the latter quantity, Mie theory (see Chapter 2.2.2) can be applied.

As subsequent investigations concentrate on emission from the mid-IR towards longer wavelengths, scattered light only plays a subordinate role. Only thermal emission will be considered here. For a given distance  $D$  to the observer, the total flux  $F_{\lambda,\text{disk}}^{\text{tot}}$  of an axially symmetric disk extending from  $r_{\min}$  to  $r_{\max}$  with a dust distribution  $N(r,s)$  for sizes between  $s_{\min}$  and  $s_{\max}$  can be expressed as

$$F_{\lambda,\text{disk}}^{\text{tot}} = \frac{2\pi}{D^2} \int_{T_g(r_{\max})}^{T_g(r_{\min})} r(T_g) \frac{dr(T_g)}{dT_g} dT_g \int_{s_{\min}}^{s_{\max}} ds N(r,s) C_\lambda^{\text{abs}}(s) B_\lambda(T_g). \quad (2.38)$$

Similarly, the radial profile of the surface brightness  $S_\lambda(r)$  of the same disk reads

$$S_\lambda(r) \approx \frac{1}{D^2} \int_{s_{\min}}^{s_{\max}} ds N(r,s) C_\lambda^{\text{abs}}(s) B_\lambda(T_g(r,s)). \quad (2.39)$$

Due to diffraction and other instrumental issues, however, resolved observations never show the “right” image. Thus, the surface brightness needs to be convolved with the specific instrument's Point Spread Function (PSF) to obtain the observable surface brightness  $S'_\lambda$ .

In general disks are inclined by an angle  $i^1$ . Coordinates in the projected sky frame will be denoted by lower-case letters and those in the disk frame by capitals. The transformation in Cartesian coordinates between both frames, neglecting the third dimension, simply reads

$$\mathbf{R} = \begin{pmatrix} x \\ y \end{pmatrix} = \begin{pmatrix} X \\ Y \sin i \end{pmatrix}. \quad (2.40)$$

Without loss of generality, the  $x$  direction is assumed along the major axis of the observed disk.

For the convolution, of course, only the sky projected surface brightness  $\tilde{S}_\lambda$  is of relevance:

$$S'_\lambda(\mathbf{r}) = \tilde{S}_\lambda(\mathbf{r}) \otimes \text{PSF}_\lambda(\mathbf{r}). \quad (2.41)$$

Given  $S_\lambda(R)$  is the surface brightness in the disk frame, it changes to  $\tilde{S}_\lambda(r)$  in the projected sky frame according to  $\tilde{S}_\lambda(r) da = S_\lambda(R(\mathbf{r})) dA$ .

The convolution therefore can be written as

$$S'_\lambda(\mathbf{r}) = (\sin i)^{-1} \int_0^\infty r' dr' \int_0^{2\pi} d\phi' S_\lambda(R(\mathbf{r}-\mathbf{r}')) \text{PSF}_\lambda(r', \phi'), \quad (2.42)$$

<sup>1</sup>Here, inclination  $i = 90^\circ$  means pole-on, while edge-on disks have  $i = 0^\circ$ .

with the surface brightness profile's argument

$$R(\mathbf{r} - \mathbf{r}') = \sqrt{(r \cos \varphi - r' \cos \varphi')^2 + (r \sin \varphi - r' \sin \varphi')^2 (\sin i)^{-2}}. \quad (2.43)$$

However, in case of a pole-on disk, Eq. (2.43) simplifies. If, furthermore, also the PSF is considered axially symmetric, the same is true for the convolved profile. Thus, it is sufficient to calculate the profile for a single azimuthal angle, e.g.,  $\varphi = 0$ , so that

$$S'_\lambda(r) = \int_0^\infty dr' r' \text{PSF}_\lambda(r') \int_0^{2\pi} d\varphi' S_\lambda \left( \sqrt{r^2 + r'^2 - 2rr' \cos \varphi'} \right). \quad (2.44)$$

For computational purposes it is convenient to replace the explicit integration in Eq. (2.42) by Fast Fourier Transformation (FFT):

$$S'_\lambda(\mathbf{r}) = \mathcal{F}^{-1} \{ \mathcal{F} \{ S_\lambda(R(\mathbf{r})) \} \mathcal{F} \{ \text{PSF}_\lambda(\mathbf{r}) \} \}. \quad (2.45)$$

## 2.4 Dynamics of Debris Disks

### 2.4.1 Mechanisms in Debris Disks

Several physical processes and mechanisms drive the evolution of dust and planetesimals in debris disks. The most important ones will be introduced below.

#### Gravity

The basics for the dynamical evolution of any particle of mass  $m$  in the gravitational field of a star of mass  $M_*$  is given by Newton's gravity law. It describes the gravitational force  $\mathbf{F}_G$  as a function of the distance vector  $\mathbf{r}$  to the star

$$\mathbf{F}_G = -G m \frac{M_*}{r^3} \mathbf{r}, \quad (2.46)$$

with the gravitational constant  $G$ . This force leads to Keplerian orbits — bound circles and ellipses or unbound parabolas and hyperbolas — with Keplerian velocities  $v_K$ .

#### Direct Radiation Pressure

Besides gravity, the particle's response to stellar radiation is important. It can be divided into a radial, velocity-independent and a velocity-dependent part. The former is called (direct) radiation pressure and its force  $\mathbf{F}_{\text{rp}}$  on the particle can be expressed in terms of the gravitational force. Thus, the total force reads

$$F_{\text{tot}} = \mathbf{F}_G + \mathbf{F}_{\text{rp}} = -G m \frac{(1 - \beta_{\text{rp}}) M_*}{r^3} \mathbf{r}. \quad (2.47)$$

Following Burns et al. (1979) with the (usual) assumption of spherical particles of radius  $s$  and density  $\rho$ , the so-called beta ratio  $\beta_{\text{rp}} = |\mathbf{F}_{\text{rp}}|/|\mathbf{F}_G|$  can be calculated as

$$\beta_{\text{rp}} = \frac{3L_* \langle Q^{\text{pr}}(s) \rangle}{16\pi G M_* c s \rho}, \quad (2.48)$$

with the stellar luminosity  $L_*$ . If one adopts Mie theory again, the wavelength-averaged radiation pressure efficiency  $\langle Q^{\text{pr}}(s) \rangle$  can be deduced from the efficiencies for extinction  $Q_\lambda^{\text{ext}}$  and

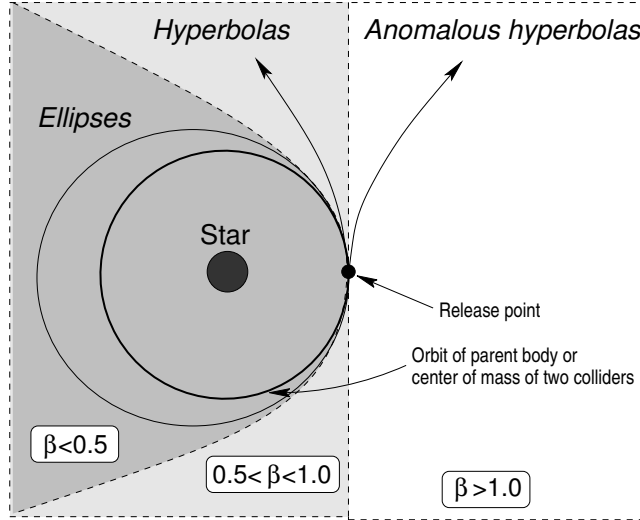


**Figure 2.1:** Sketch of the three different types of orbits a particle can adopt depending on its  $\beta$  ratio (from: Krivov et al. (2006)).

scattering  $Q_{\lambda}^{\text{sca}}$  and the asymmetry parameter  $\langle \cos \theta \rangle$ , so that

$$Q_{\lambda}^{\text{pr}}(s) = Q_{\lambda}^{\text{ext}}(s) - Q_{\lambda}^{\text{sca}}(s) \langle \cos \theta \rangle. \quad (2.49)$$

Eq. (2.47) clearly shows that Newton's law is still valid when direct radiation pressure is included. However, the particle "sees" a central star with reduced mass  $M_{*}(1 - \beta_{\text{rp}})$ . Consequently, in addition to normal Keplerian orbits hyperbolic orbits that are opened outwardly (anomalous hyperbola) are possible as well. Consider a particle released from a circular Keplerian orbit around a star, e.g., in a collision of larger objects. Due to direct radiation pressure, the orbit changes to ellipses with eccentricities  $e = \beta_{\text{rp}}/(1 - \beta_{\text{rp}})$  (Burns et al. 1979). Thus, for  $\beta_{\text{rp}} < 0.5$  the particle is still bound, for  $0.5 < \beta_{\text{rp}} < 1$  the orbit changes to (unbound) hyperbolas, and to anomalous hyperbolas for  $\beta_{\text{rp}} > 1$ . This is illustrated in Fig. 2.1. The Keplerian velocity changes to  $v_{\text{rp}} = \sqrt{1 - \beta_{\text{rp}}}v_{\text{K}}$ .

As a measure of how long a particle stays inside the system before it is removed due to radiation pressure, the blowout timescale is introduced. For a particle starting with semi-major axis  $a$  it is defined as

$$T_{\text{rp}} = \frac{2\pi}{|1 - \beta_{\text{rp}}|} \sqrt{\frac{|a|^3}{GM_{*}}}. \quad (2.50)$$

This is the timescale that corresponds to the orbital period of bound particles.

### Poynting-Robertson Drag

The velocity-dependent part of radiation pressure is usually called Poynting-Robertson (PR) drag. It acts like a "headwind" on the particles that causes them to lose velocity and therefore to spiral inwards. The drag force acting on the particles, depending on its velocity  $\mathbf{v}$ , can be given as

$$\mathbf{F}_{\text{PR}} = -Gm \frac{\beta_{\text{rp}} M_{*}}{cr^2} \left[ \frac{(\mathbf{v} \cdot \mathbf{r}) \mathbf{r}}{r^2} + \mathbf{v} \right]. \quad (2.51)$$



Taking both radiation effects together, the force reads

$$\mathbf{F}_{\text{rad}} = |F_{\text{rp}}| \left[ \left( 1 - \frac{\dot{r}}{c} \right) \frac{\mathbf{r}}{r} - \frac{\mathbf{v}}{c} \right]. \quad (2.52)$$

Here,  $\dot{r}$  is the time derivative of the distance between star and particle.

The (local) PR time scale  $T_{\text{PR}}$  is defined as the ratio of the drag induced change rate in semi-major axis to the semi-major axis itself,  $T_{\text{PR}} = a/\dot{a}$ , and is, similar to the blowout time scale, size-dependent. This is a typical time scale for the inward migration. If compared to typical collisional time scales (see Chapter 2.4.2) it turns out that for all debris disks observed to date PR drag is negligible (Wyatt 2005b). However, for tenuous disks similar to the zodiacal cloud, the drag force can efficiently impact the particles' dynamics up to sizes of hundreds of micrometers becoming the leading process after gravity (Grün et al. 1985).

### Other Mechanisms

Besides the processes described above, also other effects may occur. However, as they are of no importance for the disks discussed in this work, they are just shortly listed below.

**Stellar Wind Drag** is the particle counterpart of stellar radiation effects. With the wind velocity  $v_{\text{wind}}$  and the stellar mass loss rate  $\dot{M}_*$  parameterizing the stellar wind strength the  $\beta$  ratio for stellar wind pressure  $\beta_{\text{wp}}$  results in

$$\beta_{\text{wp}} = \frac{3\dot{M}_* v_{\text{wind}}}{16\pi G M_* \rho}. \quad (2.53)$$

As counterpart to Eq. (2.52) the wind drag force reads

$$\mathbf{F}_{\text{wind}} = |F_{\text{wp}}| \left[ \left( 1 - \frac{\dot{r}}{v_{\text{wind}}} \right) \frac{\mathbf{r}}{r} - \frac{\mathbf{v}}{v_{\text{wind}}} \right]. \quad (2.54)$$

This is only expected to play a role in disks around late-type stars which typically show strong stellar winds (e.g., Plavchan et al. 2005; Strubbe & Chiang 2006; Augereau & Beust 2006).

**Perturbations of Planets** can affect the dynamics of a dust and planetesimal disk in different ways. Here, only a few shall be mentioned. First, planets have been suggested to produce structures which are observed in some disks. Mean motion resonances can trap planetesimals creating clumps (e.g., Wyatt 2003; Greaves et al. 2005; Hahn & Malhotra 2005; Krivov et al. 2007). If the planet's orbit is inclined with respect to the disk plane, the inner part of the disk can be aligned to the planet's orbit plane, while the outer part remains unaffected, resulting in a warped disk (Mouillet et al. 1997). Secondly, an enhanced collisional dust production due to a dynamically unstable phase in the history of a system can be attributed to the rapid relocation of a giant planet (Gomes et al. 2005). The Late Heavy Bombardment in the solar system 700 Myr after its formation is an example of this phenomenon. However, Booth et al. (2009) have estimated such an event to occur only around less than 12% of sun-like stars. Given the short duration of enhanced fragment generation, the observation probability only amounts to 0.04%. Thirdly, planets may play a fundamental role in the transition from protoplanetary to debris disks. Due to gravitational friction, the largest bodies (the later planets) stir up the velocities of smaller objects until coagulation is finally replaced by destructive collisions initiating the collisional cascade (e.g., Kenyon & Luu 1999a; Kenyon & Bromley 2001, 2004a,b, 2005, 2006). This effect is known as self-stirring. Similarly, gravitational interaction with planets which have already been formed can dynamically heat up the disk (Wyatt 2005a; Mustill & Wyatt 2009).

**Electric Charge** of dust particles can couple to stellar and planetary magnetic fields, inducing a Lorentz force. Taking for example the typically size-independent surface potential of 3 – 10 V for the solar system (Wyatt 1969; Horányi 1996; Kimura & Mann 1998), the effect is strongest for 0.1  $\mu\text{m}$  and smaller particles (Leinert & Grün 1990). Especially in the inner part of a system sufficiently charged nano-dust (1 – 10 nm) can be accelerated by stellar magnetic fields to values of up to several hundred  $\text{km s}^{-1}$  (Czechowski & Mann 2010). Nevertheless, since considered disks are typically located much further from the central star and affected grains are too lightweight, the electric forces are by two to three orders of magnitude too weak to have an impact on the outcome of the collisional cascade.

### 2.4.2 Collisions

This chapter only summarizes the collisional prescription and algorithm used later for simulations (Löhne 2008). For a more general and complete discussion, the reader is referred to the literature (e.g., Stewart & Leinhardt 2009).

Consider two colliders denoted as target “t” and projectile “p” with masses  $m_t$  and  $m_p$ , respectively, to collide with impact velocity  $v_{\text{imp}}$ . Without loss of generality  $m_t > m_p$  is considered. The total mass is denoted by  $M = m_t + m_p$  and the reduced mass is defined as  $\mu = \frac{m_t m_p}{m_t + m_p}$ . Then the impact energy is given by

$$E_{\text{imp}} = \frac{1}{2} \mu v_{\text{imp}}^2. \quad (2.55)$$

Instead of impact energy, most studies use the specific impact energy  $Q = E/m$ . In a destructive collision (also: disruptive, fragmenting, or catastrophic) the largest fragment adheres less than half the total mass. The condition for a collision to end up in destruction of the target is given by

$$Q_{\text{imp}} \geq Q_{\text{D}}^*. \quad (2.56)$$

The material property  $Q_{\text{D}}^*$  is called the critical specific energy for fragmentation and dispersal. Following Benz & Asphaug (1999) this threshold can be divided into two regimes:

$$Q_{\text{D}}^*(s) = Q_{\text{D},s} \left( \frac{s}{1 \text{ m}} \right)^{-3b_s} + Q_{\text{D},g} \left( \frac{s}{1 \text{ km}} \right)^{3b_g}, \quad (2.57)$$

with the power-law indices  $3b_s$  and  $3b_g$ . In the strength regime (denoted by “s”) the sticking of the material is dominated by inter-molecular sticking forces, which is also often referred to as shear strength. While this is only valid for smaller objects, particles of typically  $s > 100 \text{ m}$  (the actual size depending on the material) are in the gravity regime (indicated by the subscript “g”). Here, self gravity is the driving force to hold the material together.

Provided both colliders are of similar strength, the impact energy equally splits on target and projectile and the fragmentation condition for the projectile can be written as

$$\frac{1}{2} E_{\text{imp}} \geq m_p Q_{\text{D}}^*(m_p). \quad (2.58)$$

If impact energies are too low to fulfill Eq. (2.58), some material will be excavated from both target and projectile. The mass ruptured in such an event amounts to

$$m_{\text{crat, t/p}} = \frac{1}{2} \frac{E_{\text{imp}}/2}{Q_{\text{D}}^*(m_{\text{t/p}})}. \quad (2.59)$$

In principle, even lower impact energies will end up in bouncing or agglomeration. Such events are not supposed to play a significant role, though. Large planetesimals and possible formed

planets heat up the disk dynamically causing relatively high impact velocities ( $\gtrsim 100 \text{ m s}^{-1} - 1 \text{ km s}^{-1}$ ). Further, they cannot be damped by interaction with gas which has left the system at the end of the protoplanetary phase. Therefore, these two effects are neglected in this work.

As the projectile can only absorb as much energy as it needs to be fragmented, the remaining energy  $E_{\text{rem}} = E_{\text{imp}} - m_p Q_D^*(m_p)$  is inherited by the target. This will be fragmented if

$$E_{\text{rem}} \geq m_t Q_D^*(m_t). \quad (2.60)$$

However, if the remaining energy is not sufficient to destroy the target, some material will be excavated by the projectile. This is called a cratering collision. The released mass  $m_{\text{crat}}$  in such a collisional event is, in accordance with Eq. (2.59), given by

$$m_{\text{crat}, t} = \frac{1}{2} \frac{E_{\text{rem}}}{Q_D^*(m_t)}. \quad (2.61)$$

To calculate the mass distribution of the collisional outcome, the material is split into two parts: the remnant and the excavated mass  $m_{\text{rem}}$  and  $m_{\text{exc}}$ , respectively. Depending on the collisional regime (I. — fragmenting, II. and III. — cratering), the masses are given by

$$\text{I.} \quad m_{\text{rem}} = 0 \quad \text{and} \quad m_{\text{exc}} = m_p + m_t \quad (2.62)$$

$$\text{II.} \quad m_{\text{rem}} = m_t - m_{\text{crat}, t} \quad \text{and} \quad m_{\text{exc}} = m_p + m_{\text{crat}, t} \quad (2.63)$$

$$\text{III.} \quad m_{\text{rem}} = (m_t + m_p) - (m_{\text{crat}, t} + m_{\text{crat}, p}) \quad \text{and} \quad m_{\text{exc}} = m_{\text{crat}, t} + m_{\text{crat}, p}. \quad (2.64)$$

The fragment distribution then reads

$$g(m) = (2 - \eta) m_{\text{exc}} \cdot \left( \frac{m_x}{m} \right)^\eta \cdot \frac{1}{m_x^2} \Theta(m_x - m) + \delta(m - m_{\text{rem}}), \quad (2.65)$$

with the Dirac and Heaviside step functionals  $\delta(x)$  and  $\Theta(x)$ . The slope of the distribution is in the range  $1.5 < \eta < 2$  (Fujiwara 1986, and references therein) with the “classical” value of  $\eta = 1.83$ .

The only parameter that is still missing is the mass of the largest fragment  $m_x$ . It changes, depending on whether the target is destroyed or cratered:

$$\text{I.} \quad m_x = \frac{1}{2} M \left( \frac{m_t Q_D^*(m_t) + m_p Q_D^*(m_p)}{E_{\text{imp}}} \right)^c \quad (2.66)$$

$$\text{II. \& III.} \quad m_x = m_{\text{exc}} \frac{2 - \eta}{\eta - 1}. \quad (2.67)$$

In case of fragmenting collisions, laboratory results for the slope range from  $c \approx 1.24$  for basalt (Fujiwara et al. 1977) to  $c \approx 0.91$  for ice (Arakawa 1999).

Previous studies (e.g., Löhne et al. 2008) only took catastrophic collisions into account. Here, however, cratering collisions will be included as well. This is necessary, as cratering collisions alter the size distribution of dust in the disk markedly, which shows up in thermal emission (Thébault et al. 2003; Thébault & Augereau 2007).

An essential difference to other investigations is the assumption of a single power law for the size distribution of the fragments in an individual collision in Eq. (2.65). Instead, a broken power-law was proposed originally by Thébault et al. (2003). However, this difference has little effect on the resulting size distribution in collisional equilibrium (see Chapter 5.4 for a more detailed discussion).

### 2.4.3 Kinetic Theory

In recent years, statistical approaches as known from kinetic theory in statistical physics have proven successful to describe debris disks. Several authors deduced analytical expressions for the disks' mass and spatial distribution and their evolution (e.g., Dominik & Decin 2003; Wyatt et al. 2007c). Naturally, such approaches inhere in strong assumptions on the underlying physics. To overcome these limitations numerical simulations are required (e.g., Thébault et al. 2003; Kenyon & Bromley 2008, 2010). Alternative methods are usually not suitable. Hydrodynamical approaches can only be applied when densities of gas or dust are high enough so that the material can be considered a fluid. Due to computational limitations, N-body simulations cannot handle the required number of particles. Moreover, there exists no possible treatment of mutual collisions in such approaches. In contrast, N-body simulations are the best choice to investigate structures in the disk (e.g., Wyatt 2003, 2005a; Reche et al. 2008; Stark & Kuchner 2008). Still, recently a new way was suggested to emulate collisions in N-body models (Stark & Kuchner 2009; Kuchner & Stark 2010). Besides that, a hybrid method was proposed to model the formation of spiral arms as a result of dust avalanches in debris disk (Grigorieva et al. 2007).

This work applies numerical solutions of the statistical approach. Given a set of phase space variables  $\mathbf{p}$  (e.g., location and velocity of differently sized objects), the state of the disk can be described via the phase space distribution function  $n(\mathbf{p}, s, t)$ . It is defined that  $n(\mathbf{p}, s, t) d\mathbf{p} ds$  is the number of particles with  $[\mathbf{p}; \mathbf{p} + d\mathbf{p}]$  and  $[s; s + ds]$  at a given time instant  $t$ . Accordingly, for the total number of objects this implies

$$N = \int_{\mathbf{p}} \int_s n(\mathbf{p}, s, t) d\mathbf{p} ds. \quad (2.68)$$

The evolution of the disk can then be expressed via the master equation

$$\frac{dn}{dt}(\mathbf{p}, s, t) = \left( \frac{\partial n}{\partial t} \right)_{\text{gain}} - \left( \frac{\partial n}{\partial t} \right)_{\text{lost}} - \text{div}(n\dot{\mathbf{p}}) \quad (2.69)$$

(Krivov et al. 2000). Neglecting the divergence, Eq. (2.69) is sometimes also referred to as Boltzmann-Smoluchowski equation (according to the underlying Boltzmann and Smoluchowski/coagulation equation). The righthand side of this equation can be split into two parts: the partial derivatives corresponding to gain and loss due to mutual collisions between disk constituents, and the transport term (Krivov et al. 2005; Löhne 2008). Only considering the first part, the master equation can be reformulated

$$\begin{aligned} \frac{dn}{dt}(\mathbf{p}, s, t) &= \int \int \int \int [G(\mathbf{p}, s; \mathbf{p}_1, s_1; \mathbf{p}_2, s_2) - L(\mathbf{p}_1, s_1; \mathbf{p}_2, s_2) \delta(\mathbf{p} - \mathbf{p}_1) \delta(s - s_1)] \\ &\quad \times n(\mathbf{p}_1, s_1, t) n(\mathbf{p}_2, s_2, t) \\ &\quad \times d\mathbf{p}_1 ds_1 d\mathbf{p}_2 ds_2, \end{aligned} \quad (2.70)$$

where  $G$  and  $L$  are the gain and loss functions, respectively. The Dirac functional  $\delta$  is defined in such a way that for any given function  $\phi = \phi(\mathbf{x})$ :

$$\int d\mathbf{x}' \phi(\mathbf{x}') \delta(\mathbf{x} - \mathbf{x}') = \begin{cases} \phi(\mathbf{x}) & \text{if } \mathbf{x} = \mathbf{x}' \\ 0 & \text{else} \end{cases}. \quad (2.71)$$

The gain function can then be split into the probability  $R$  for a collision between the two consid-

ered objects, and the distribution of fragments  $F$ :

$$G(\mathbf{p}, s; \mathbf{p}_1, s_1; \mathbf{p}_2, s_2) = R(\mathbf{p}, s; \mathbf{p}_1, s_1; \mathbf{p}_2, s_2)F(\mathbf{p}, s; \mathbf{p}_1, s_1; \mathbf{p}_2, s_2). \quad (2.72)$$

$F$  is basically composed of the fragment distribution given in Eq. (2.65).

Transport mechanisms like PR or wind drag act like diffusion processes, formally represented in the last term in Eq. (2.69), imposing an additional, explicit time dependence on the phase space variable. Without transport, a particle remains on its orbit on which it was released until it is destroyed in a collision.

As shown in Krivov et al. (2005) and Krivov et al. (2006) this statistical approach can be reformulated in orbital elements  $\mathbf{p} = (a, e, i, \Omega, \omega, \theta)$  so that it applies to circumstellar systems.

## 2.5 Evolution of Debris Disks

### 2.5.1 The “Steady-State” Disk

The notion of a quasi-steady state or quasi equilibrium refers to the amount of particles of different sizes and on different orbits staying constant relative to each other, while the overall amount changes with time. With the same nomenclature of Chapter 2.4.3, this can mathematically be expressed as

$$n(\mathbf{p}, s, t) = \tilde{n}(\mathbf{p}, s)f(t), \quad (2.73)$$

with a continuously differentiable function  $f(t)$ . Ignore transport mechanisms first of all and consider the total disk mass and the time derivative of the total disk mass according to Eq. (2.73) as  $M_{\text{disk}} = f(t) \int \int \tilde{n}(\mathbf{p}, s) d\mathbf{p} ds$  and  $\dot{M}_{\text{disk}} = \dot{f}(t) \int \int \tilde{n}(\mathbf{p}, s) d\mathbf{p} ds$ . Together with Eq. (2.70) it can be found that  $\dot{n} \propto f^2(t)$ , and thus  $\dot{f}(t) \propto f^2(t)$ , resulting in

$$f(t) = \frac{1}{1 + t/T_{\text{char}}}. \quad (2.74)$$

The characteristic time  $T_{\text{char}}$  is the time for a particle of size  $s$  to be destroyed. It increases with grain size and distance to the star. A quasi equilibrium is only reached for

$$t \gg T_{\text{char}}. \quad (2.75)$$

Consequentially, the larger the particles and the further away from the star they are located, the longer it takes them to start evolving in a quasi-steady state. The longer the disk has evolved, the more parts of the disk are in quasi equilibrium. Once the condition in Eq. (2.75) is fulfilled, the shape of the size and spatial distribution does no longer change in the considered grain size and spatial region. Mathematically, this means that the ratio  $C = -\dot{M}_{\text{disk}}/M_{\text{disk}}^2 = \dot{f}(t)/f^2(t)$  cannot be a constant over time. Taking numerical simulations, Löhne et al. (2008) showed that it decreases as  $C \propto t^{-2/3 \dots -4/5}$ .

For reasons of brevity, the adjective “quasi” will be omitted in the following. The onset of a steady-state evolution is a well known feature in debris disk models that enable the use of certain scaling rules (e.g., Löhne et al. 2008; Krivov et al. 2008). This will now be explained in detail.

### 2.5.2 Scaling Laws

In case of a purely collision-driven disk evolution, three scaling rules for modeled disk distributions have been found, when the disk has reached the collisional equilibrium (earlier phases may require a more sophisticated treatment).

**a) Dependence of Evolution on Initial Disk Mass:** Given a disk at distance  $r$  to the star at a time instant  $t$  with an initial disk mass  $M_0$ . For any quantity  $F(M_0, r, t)$  which is directly

proportional to the amount of material in any size interval Löhne et al. (2008) found the disk's evolution following

$$F(xM_0, r, t) = xF(M_0, r, xt), \quad (2.76)$$

for any factor  $x > 0$ . This means that an increase of the initial disk mass leads to an amplification of  $F$  but at the same time the evolution will speed up.  $F$  can be considered the total disk mass  $M_{\text{disk}}$  which is dominated by large planetesimals. Alternatively,  $F$  can be taken to be the dust mass  $M_{\text{dust}}$  that only measures the mass of objects up to 1 mm. Besides that also the corresponding cross sections can be used.

**b) Dependence of Evolution on Distance:** Shifting the location of the disk approximately affects the disk evolution according to

$$F(M_0, xr, t) \approx F(M_0, r, x^{-4.3}t) \quad (2.77)$$

(Wyatt et al. 2007b; Löhne et al. 2008). Thus, the further away from the star the slower the disk evolves.

**c) Dust Mass as a Function of Time:** Löhne et al. (2008) also claim that the decay of dust mass can be approximated by

$$M_{\text{dust}}(M_0, r, xt) \approx x^{-\xi} M_{\text{dust}}(M_0, r, t), \quad (2.78)$$

where  $\xi \approx 0.3 - 0.4$ . Basically, this last scaling is valid in the strength regime. It can thus be extended from the dust mass  $M_{\text{dust}}$  to the mass of objects smaller than about 100 m.

# Chapter 3

## Numerical Tools

*Research is what I'm doing when I don't know what I'm doing.*

WERNHER VON BRAUN

### 3.1 Computation of the Collisional Evolution — ACE

To model a debris disk's collisional evolution the ACE (Analysis of Collisional Evolution) code was developed over the last six years in the theory group of the Astrophysical Institute in Jena, Germany. It is based on the kinetic theory as discussed in Chapter 2.4.3 (Krivov et al. 2005, 2006; Löhne et al. 2008). Like all numerical tools presented in this Chapter, ACE is written in C/C++. For a detailed description of the discretization of the underlying algebra and the integrator see the PhD thesis by Löhne (2008).

For a specific simulation a set of about 60 parameters has to be specified, ranging from stellar properties to material properties, details concerning the dynamics, and computational settings. In particular, the initial distribution of planetesimals<sup>1</sup> is requested, namely the initial disk mass  $M_0$ , the initial spatial extension, the initial slopes for the spatial and size distribution (usually chosen such as to produce a constant optical depth in the initial planetesimal ring), and the dynamical excitation (eccentricity and inclination range). The mechanisms that can be handled with ACE are stellar gravity, mutual collisions (with the different regimes, see Chapter 2.4.2), Poynting-Robertson drag, wind drag, and gas drag. However, in all cases considered in this work drag forces can be neglected without compunction.

Once it is started, ACE solves the Boltzmann-Smoluchowski kinetic equation in three dimensions: grain mass (or size), semi-major axis (or pericenter), and eccentricity. Therefore, the equation is averaged over the remaining orbital elements:

$$n(a, e, s, t) = \int \int \int \int d\theta d\omega d\Omega di n(a, e, i, \Omega, \omega, \theta, s, t) \quad (3.1)$$

(for details see Krivov et al. 2005, 2006). The code is fast enough to follow the debris disk's evolution over stellar lifetimes. As a result, ACE prints out disk mass, dust mass, and planetesimal mass, as well as the coupled grain size and radial distribution at different time steps in the system's evolutionary history.

### 3.2 Computation of Thermal Emission Properties

In contrast to the ACE code, both programs (SEDUCE and SUBITO) to extract thermal emission properties are the author's contribution to the set of numerical tools which are used in this work. They are presented below.

#### 3.2.1 SEDUCE

Once the development of ACE had reached a point at which it was expected to cope with processes in real debris disks it was a natural step to implementing tools to extract observables from the synthetic disk models. This is exactly the purpose of this work. Therefore, the code SEDUCE (SED Utility for Circumstellar Environment) was designed to extract SEDs from the dust portion of modeled ACE disks. SEDUCE is based on Eqs. (2.38) and (2.37).

---

<sup>1</sup>Note that it is sufficient to concentrate on larger bodies because for typical lifetimes of small grains are rather short so that almost instantaneously a steady state is reached in the dust regime which is independent of the considered initial distribution of small objects.

The information required for SED calculations can be grouped in three categories. The first group covers the central star. SEDUCE expects synthetic *NextGen* photosphere models (Hauschildt et al. 1999), which need to be converted into units that are used for internal calculations. Therefore, the stellar radius, or alternatively the stellar temperature and luminosity are important. Occasionally, stellar parameters may differ with stellar latitudes (see Chapter 5.3). Thus, it is requisite to differentiate between stellar parameters perceived by the disk and those seen from the observer. The second category is concerned with dust properties, namely the bulk density and the refractive indices, which are used to derive absorption cross sections using a Mie algorithm from Bohren & Huffman (1983). Principally, it is possible to consider several dust components with different ratios. As ACE can only handle a single material, usually one dust component is used. The last parameter group deals with the considered dust distribution. Given a certain ACE disk, SEDUCE reads the distribution in a specified size and spatial range. Alternatively, analytical expressions of the kind  $N \propto r^{-\xi} s^{-\eta}$  can be considered as well. In this case it is also possible to calculate the SED for several dust rings with different chemical compositions at the same time.

In the past, some codes have been developed to analyze the parameter space to find a best fit to a set of observations by minimizing  $\chi^2$ . However, ACE simulations are far too time-consuming to be performed in the required quantity for such a fitting approach. Thus, the only parameter that can be adjusted by SEDUCE is the disk mass corresponding to a vertical shift of the SED. In case of power-law dust distributions this is straight forward because the disk mass is independent of other parameters. When considering ACE disks, however, scaling rules as explained in Chapter 2.5.2 need to be applied. In particular, if the disk is considered in a steady state, the dust mass  $M_{\text{dust}}$  is directly proportional to the height of the SED. Then Eq. (2.76) can be rewritten as

$$M_{\text{dust}}(xM_0, t/x) = xM_{\text{dust}}(M_0, t). \quad (3.2)$$

Thus, if a dust mass  $x$ -times larger (smaller) than the original mass is needed, a similar disk  $x$ -times denser (more tenuous) than the original one at an earlier (later) time instant  $t/x$  will provide the desired dust mass. However, what is searched for is the initial disk mass that will produce the desired dust mass at the given age  $t$  of the system. Basically, this problem can be solved analytically by combining the first and third scaling law (Eqs. (2.76) and (2.78)), once the slope of the dust mass decay  $\xi$  is known.

SEDUCE only makes use of the first (and only exact) scaling rule, so that an iterative algorithm is mandatory. For the sake of simplicity, first a single observation at wavelength  $\lambda$  is considered. The model's total emission at the given age  $t$  of the system with the nominal dust mass  $M_{\text{dust}}(M_0, t)$  denotes  $F_{\lambda, \text{disk}}^{\text{tot}}(M_0, t)$  and the observed flux at  $\lambda$  is called  $F_{\lambda, \text{obs}}^{\text{tot}}$ . The ratio  $\alpha = F_{\lambda, \text{obs}}^{\text{tot}}/F_{\lambda, \text{disk}}^{\text{tot}}(M_0, t)$  directly leads to the required dust mass  $M_{\text{dust}}^{\text{req}} = \alpha M_{\text{dust}}(M_0, t)$ . Then  $x = \alpha$  can be used as a first approximation for the scaling factor in the iterative scheme

$$M_{\text{dust}, i} = M_{\text{dust}}(x_i M_0, t) = x_i M_{\text{dust}}(M_0, x_i t) \quad (3.3)$$

$$x_{i+1} = M_{\text{dust}, i} / M_{\text{dust}}(M_0, t). \quad (3.4)$$

The accuracy of the fit is limited by the time resolution of the ACE outcome. Once the final scaling factor  $x$  is found, the total disk mass follows from  $M_{\text{disk}}^{\text{fin}} = xM(M_0, xt)$ . The final initial disk mass is simply  $M_0^{\text{fin}} = xM_0$ . In practice, it is of course not only a single SED point that should be reproduced. The initial guess for the scaling factor  $\alpha$  is therefore determined by a  $\chi^2$  minimization algorithm.



### 3.2.2 SUBITO

Complementary to SEDUCE, the program SUBITO (SURface Brightness Investigation TOOL) was developed to calculate radial surface brightness profiles for single wavelengths. Model parameters are almost identical to those of SEDUCE, except for the stellar parameters. SUBITO only needs the properties as seen from the disk. Furthermore, SUBITO was not given the possibility to scale dust masses to observed profiles. Instead, it is supposed to use dust distributions which have already been scaled with SEDUCE. Using SEDUCE for mass scaling first of all and applying SUBITO subsequently does make sense since usually more SED points are given than resolved observations. The SED is therefore more suited to constrain the dust mass, whereas the profiles provide additional information on the disk shape.

To convolve the surface brightness profiles with the PSFs at the given wavelengths, as given in Eq. (2.45), an additional code was developed. The system's inclination  $i$  and — if  $i \neq 90^\circ$  — the rotation angle of the observed disk are parameters required for the convolution. As a result, images are obtained from which again profiles can be extracted. However, especially when images are analyzed, it is important to consider the correct orientation of the PSFs as even small asymmetries directly translate into the convolved images (although their impact on the profiles may be negligible).

### 3.2.3 Numerical Caveats

Before applying the two codes SEDUCE and SUBITO to real astrophysical objects, several tests and consistency checks were performed. It is beyond the scope of this work to present the different efforts. For more information the reader is referred to Müller (2007).

Fundamental to the modeling of thermal emission properties of a given debris disk is the proper calculation of the particles' optical properties. As mentioned above, this is done by Mie theory. However, for long it is known that the most popular implementation given by Bohren & Huffman (1983) only provides accurate results for small size parameters, in particular for  $x \leq 2 \times 10^4$  (e.g., Wolf & Voshchinnikov 2004). This is of particular interest for the largest particles when calculating the absorbed stellar radiation and hence the grain temperature. Nevertheless, regarding the photosphere of the hottest star in this work (Vega, see Chapter 5.3), which peaks at about  $0.7 \mu\text{m}$ , the size parameter of the largest considered grains (1 mm) equals  $x_{\text{peak}} = 9 \times 10^3$ . This is well below the limit given above. Since the stellar spectrum drops quickly towards shorter wavelength (larger size parameters) the impact of numerical uncertainties in the implemented algorithm can be neglected.

Additionally, as will be discussed more thoroughly in Chapter 5.4.2, modeled emission in the sub-mm is object to further uncertainties. As emission in this spectral region mainly stems from large particles, it appears too costly to implement a more complex and therefore more slow algorithm. Still, a more sophisticated code is available that can be implemented when a very accurate treatment of particles with even larger size parameters is requested (Wolf & Voshchinnikov 2004).

Another numerical issue arises from the step from analytical dust distributions towards the binned ACE output. Due to long computation times the resolution in the ACE parameter space is very limited. This can affect the modeling results in two ways. First, if the (pericenter, eccentricity, or mass) grid of the simulation is not sufficiently narrow, the synthetic distribution fails to converge. In this case results are not trustworthy, anyway. It thus makes no sense to proceed with computation of the thermal emission properties. Since convergence of ACE simulations is beyond the scope of this work, the reader is referred to the literature. For all simulations performed here the grid was adjusted thus as to provide accurate results while still allowing simulations in a reasonable period of time (T. Löhne, priv. com.).

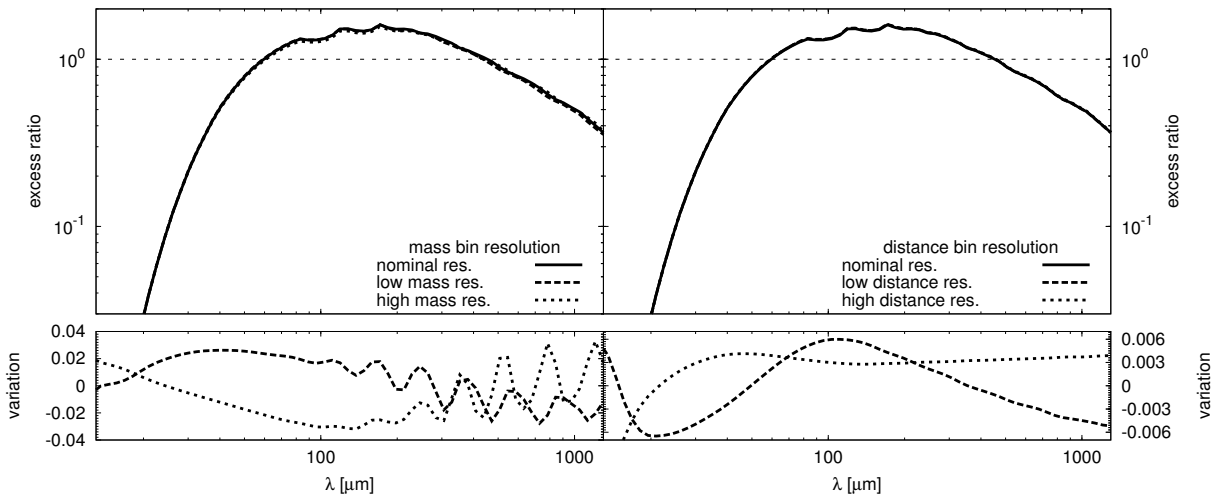


**Figure 3.1:** Comparison of the same standard disk model (solid lines, see the 10EKB@30AU disk in Chapter 5.2.2) with halved (dashed lines) and doubled resolution (dotted lines) in the dust mass (lefthand plots) and distance binning (righthand plots). Top: excess ratio. Bottom: variation from the nominal resolution used in the course of this work.

Second, the coarser the binning in the dust distribution the larger the uncertainties for the interpolation (SEDUCE and SUBITO use a simple linear interpolation scheme) in subsequent calculations become. This concerns both, the mass and the distance grid. In the remainder of this chapter the impact of the bins' width on the resulting thermal emission properties will be checked. Starting from a standard disk model (see the 10EKB@30AU disk in Chapter 5.2.2) with nominal grid resolution as it is used in the course of this work four additional simulations were performed doubling / halving the number of dust mass / distance bins<sup>2</sup>. Fig. 3.1 shows the SEDs of this standard disk with its different grid resolutions in the upper panel. To amplify the differences in the models instead of the excess flux the excess ratio (ratio of disk excess emission to stellar photosphere radiation, see also Chapter 5.3.2) is plotted as a function of wavelength. The different curves are almost identical. Thus, the bottom panel gives the relative deviations of the modified disk models from the nominal resolution model for a better comparison. This comparison demonstrates that the chosen nominal resolution provides accurate results. As expected, changes from the distance grid width are negligible with deviations below 1%. Also the differences resulting from the mass grid resolution remain below 3%, which is within the typical error for photospheric observations. Given the possible (mathematical) accuracy of the desired modeling algorithm (see Chapter 5) this is absolutely acceptable and justifies the choice of the nominal grid resolution.

<sup>2</sup>It shall be noted that the changes in the distance grid resolution are negligible for the simulations' convergence. Especially the distance binning cannot affect the accuracy of the synthetic disk distribution, because ACE calculations only use the semimajor axis (or pericenter). The distance distribution is separately computed for the output of the disk distribution (see Krivov et al. 2005).

## Chapter 4

# Classical Modeling

*Your theory is crazy, but it's not crazy enough to be true.*

NIELS BOHR

### 4.1 The Classical Modeling Approach

As discussed in Chapter 1.2, the dust surrounding the central star is the only observable signpost of a debris disk. Thus, photometric modeling of an observed debris disk always has to concentrate on reproducing the dust portion's emission properties. Assuming a certain model for the dust distribution in the disk these properties can be calculated and compared to actual observations. Moreover, possible deviations between real and model disk observables have to be minimized by varying the free parameters in the model, which finally provides some insight into possible disk properties.

In the beginning of debris disk studies the adopted model was still very simple. Aumann et al. (1984) assumed a single blackbody of 85 K (corresponding to a stellar distance of 85 AU) to reproduce the measured *IRAS* fluxes for Vega. However, additional observations came up soon indicating the need for improving the model (Harper et al. 1984). First, spatial distributions of dust were implemented and emission properties modified (e.g., Buitrago & Mediavilla 1985, 1986; Anandarao & Vaidya 1986). Temperatures, however, were basically still blackbody temperatures. With upcoming observations and improving computational capabilities the debris disk model was extended once more by adding a grain size dependence. Temperatures were now self-consistently calculated (see Chapter 2.3.2) taking the deviations from blackbody radiation not only for emission but also for absorption of stellar radiation into account (Wolstencroft & Walker 1988; Artymowicz et al. 1989; Backman & Paresce 1993). With it the classical debris disk model was defined and afterwards only minor modifications were added. Several tools have been developed to calculate emission resulting from such model disks (e.g., Wolf & Hillenbrand 2005; Augereau et al. in prep.).

Below, the most important model parameters that can be fitted to match observations are introduced (for a more detailed discussion on the different model parameters see Wolf & Hillenbrand 2003):

- *The dust chemical composition.* The most simple assumption is to consider dust as blackbody radiators. Then, temperatures in the disk are independent of grain size and directly translate into distance from the central star. Especially when dealing with large number statistics this is the usual assumption (e.g., Hillenbrand et al. 2008). To make it more realistic, some authors added a constant dust opacity / mass absorption coefficient to account for scattering losses (e.g., Holland et al. 1998). This, however, can only be a reasonable solution if just a single observational wavelength and a narrow range of grain sizes is considered. A further improvement is the assumption of a modified blackbody. Here an additional wavelength dependence is introduced so that the dust's emission is of the kind  $F_\lambda \propto \lambda^{-\nu} B_\lambda$ . More elaborate models implement Mie theory which requires a set of optical data (usually refractive indices). The standard choice is astrosil. Besides that, also amorphous carbon and ice, as well as combinations of all these species are typical dust materials. Effective medium theory allows emulating inhomogeneity (e.g., Augereau et al. 1999). First efforts have been made to come to a more precise description of the particles' emission behavior (Shen et al. 2009). However, due to high computational requirements and a huge set of additional free parameters, this method is still unhandy.

- *The dust location.* In case resolved observations are available, this parameter is of course quite confined. However, as for most known debris disk systems only the excess in the SED is observed this remains a free parameter. In general, a complete spatial distribution requires an inner and an outer edge, as well as an analytical description for the distribution in between. The most common choice for such a distribution is a power-law. Anyway, especially in large number statistics only an average location of dust is of interest.
- *The dust size distribution.* This can of course only come into play, if non-blackbody radiators are considered, because blackbody particles all emit at the same temperature and thus only the total emitting dust area is of interest. Only if the area shall be converted into dust mass, certain assumptions on the grain size (distribution) are necessary. Typically, the assumed distribution follows a power-law with an upper and a lower cutoff. Often, variation of the power-law index is ignored and the parameter is simply set to  $-3.5$ , the solution for a collisional cascade in equilibrium (Dohnanyi 1969). Another simplification is to assume a set of single grain sizes and scale their abundance to the observations (for a comparison between both approaches see, e.g., Su et al. 2005).
- *The dust mass.* As it is directly proportional to the total height of emission but does not affect the spectral or spatial appearance of the emission, the dust mass is well constrained, once the other model parameters have been fixed. The final dust mass is very sensitive to the considered dust sizes and their composition.

Within this approach it is also possible to combine multiple dust “rings” (Backman et al. 2009; Reidemeister et al. 2009; Su et al. 2009). Fitting algorithms differ: eye fitting and  $\chi^2$  minimization schemes are most popular.

Obviously, the more observations available the better constrained and less degenerate are the model parameters. As an example it is very difficult to distinguish the effects of spatial and size distribution, if no images are by hand. If only the SED is known, but the coverage with observations in the sub-mm and radio is poor, no conclusive result will be possible on the outer disk edge and the upper grain size cutoff. Similarly, a lack of photometry in the mid-IR hinders conclusions on the inner disk edge and the smallest grain sizes.

Recent years have shown a trend dealing with two directions. On the one hand, objects with an excellent coverage of different observations are modeled in-depth (Su et al. 2005, 2009; Backman et al. 2009). On the other hand, debris disk systems with low or intermediate number of observation are neglected for detailed investigations. Instead, information about many objects were gathered to use two- or three-parameter fits (usually disk location and mass) applying the results for large number statistics (e.g., Bryden et al. 2006; Su et al. 2006; Trilling et al. 2008; Hillenbrand et al. 2008).

The main focus of this work lies on the development of a new modeling approach that is based on the numerical simulation of the whole debris discs collisional evolution (see section 5). However, for reasons of completeness, in the following an example of a detailed debris disk modeling within the classical modeling method is presented. Subsequently, a discussion about advantages and disadvantages is attached.

## 4.2 Application: HR 8799

(Results presented here are based on work that was carried out for “Reidemeister et al. (2009)”. The author’s contribution is described in detail in Chapter 4.2.3, while additional investigation results obtained by other team members are added in Chapter 4.2.4 for the sake of completeness.)

### 4.2.1 The System

HR 8799 is an A5 V star at a distance from Earth of about 40 pc. For more than 20 years the system has been known to show a strong excess in IRAS observations in the far IR (Sadakane &

Nishida 1986; Zuckerman & Song 2004; Rhee et al. 2007), which was supported by subsequent ISO (Moór et al. 2006) and Spitzer/MIPS measurements (Su et al. 2009). In addition, warm dust emission in the mid-IR with Spitzer/IRS (Jura et al. 2004; Chen et al. 2006) and very cold dust in the sub-mm and radio with JCMT and IRAM (Williams & Andrews 2006; Sylvester et al. 1996) were detected.

This system is special, because three planetary candidates<sup>1</sup> were discovered by direct imaging with *Keck* and *Gemini* (Marois et al. 2008). In confirmation of the presence of the outermost planet Lafrenière et al. (2009) and Fukagawa et al. (2009) analyzed archive data from HST/NICMOS from 1998 and SUBARU/CIAO from 2002, respectively. Close & Males (2010) could not find any companion more massive than  $3 M_{\text{Jup}}$  within 600 AU. Unfortunately, age and inclination of HR 8799 are highly uncertain leaving planetary locations and masses unconstrained. Marois et al. (2008) give a probable mass range of  $7 - 10 M_{\text{Jup}}$  and projected distances of 24, 38, and 68 AU. First dynamical analyses were performed by Fabrycky & Murray-Clay (2010) and Goździewski & Migaszewski (2009).

While previous studies only concentrated on single aspects of the system, like the planets or the planetesimals, in this analysis (Reidemeister et al. 2009) a comprehensive investigation of the whole system is performed, starting with the central star, covering the dust disk and planets and ending with the planetesimal reservoir, in order to obtain a synthetic view of the planetary system. All available observational data is gathered and analyzed. Presenting all investigations is far beyond the scope of this work. Therefore, Chapter 4.2.3 explains the photometric modeling in detail, while Chapter 4.2.4 summarizes the results from Reidemeister et al. (2009) concerning the other components of the system. Finally, Chapter 4.2.5 connects both parts and draws final conclusions.

## 4.2.2 Modeling Preparations

Before getting started with the main modeling, it is essential to deduce an accurate stellar photosphere. For this purpose, *NextGen* model atmospheres (Hauschildt et al. 1999) were fitted to visible and near-IR photometry (for a more detailed description see Reidemeister et al. 2009). The best fit photosphere model is then used to extrapolate stellar emission down to radio wavelengths so that the stellar contribution of observed photometry data could be subtracted. Results are shown in Table 4.1.

Besides that, a *SPITZER/IRS* spectrum (originally published by Chen et al. 2006) was extracted from the archive and re-reduced. The final result is added in Fig. 4.1. Unfortunately, calibration of the spectrum is vague. This emanates from uncertainties in background subtraction and the lack of reliable mid-IR photometry, that could serve for reasonable scaling of the spectrum.

## 4.2.3 Photometric Modeling

### The Modeling Idea

The most straight forward way of applying the classical way of debris disk modeling is to assume the observed dust to be distributed in a single ring around the star. The disk extension together with the other disk parameters can then be found by automated fitting routines. In this study, however, another procedure will be followed. This is for two reasons. First, dust generation in the HR 8799 system is supposed only to occur in certain regions where planetesimal evolution is stable against planetary perturbations. Thus, also the dust distribution should be ‘coupled’ to the discovered planets. Of course dust at the lower end of the size distribution is too small to be

---

<sup>1</sup>For reasons of brevity and simplicity, from now on they are called “planets”. The definition of an extrasolar planet is under current debate and the most widespread understanding of an “exoplanet” as a star-orbiting object with a mass below the deuterium burning limit is not generally accepted. Yet, it cannot be excluded that at least one of the companions in the system of HR 8799 lies above this limit of about  $13.6 M_{\text{Jup}}$ .

**Table 4.1:** Photometric data of HR 8799.

$\lambda$ [ $\mu\text{m}$ ]	$F_{\text{disk}}$ [mJy]	Instr.	Ref.
12	$(2.67 \pm 0.34) \times 10^2$	IRAS	Helou & Walker (1988)
12	$(2.78 \pm 0.36) \times 10^2$	IRAS	Moshir et al. (1990)
24	$(2.9 \pm 0.17) \times 10^1$	Spitzer	Su et al. (2009)
25	$(2.46 \pm 0.00) \times 10^2$	IRAS <sup>*</sup> )	Helou & Walker (1988)
25	$(1.74 \pm 0.75) \times 10^2$	IRAS <sup>*</sup> )	Moshir et al. (1990)
60	$(3.07 \pm 0.61) \times 10^2$	IRAS	Helou & Walker (1988)
60	$(3.11 \pm 0.62) \times 10^2$	IRAS	Moshir et al. (1990)
60	$(4.12 \pm 0.21) \times 10^2$	ISO	Moór et al. (2006)
70	$(6.05 \pm 0.31) \times 10^2$	Spitzer	Su et al. (2009)
90	$(5.85 \pm 0.41) \times 10^2$	ISO	Moór et al. (2006)
100	$(2.38 \pm 0.00) \times 10^3$	IRAS <sup>*</sup> )	Helou & Walker (1988)
100	$(3.20 \pm 0.98) \times 10^3$	IRAS <sup>*</sup> )	Moshir et al. (1990)
160	$(5.54 \pm 0.66) \times 10^2$	Spitzer	Su et al. (2009)
850	$(1.03 \pm 0.18) \times 10^1$	JCMT	Williams & Andrews (2006)
1100	$3.3 \times 10^1$	JCMT <sup>*</sup> )	Sylvester et al. (1996)
1200	$(4.8 \pm 2.7) \times 10^0$	IRAM	Sylvester et al. (1996)

Notes: IRAS fluxes are color corrected as described in the IRAS Explanatory Supplement (Beichman et al. 1988), <sup>\*</sup>) Upper limits

significantly affected dynamically by the planets. Still, the perturbed planetesimal distribution should (to some extent) be inherited by the small grains. Second, this work does not yield in finding a mathematical perfect match with the observations. It rather focuses on making some rough estimates on the location of dust belt(s) and the amount of observed dust that can later be compared to the dynamical studies on the planet and planetesimal stability in order to draw a complete picture of the system. Therefore, no sophisticated fitting algorithms will be used but all model parameters are adjusted using by-eye fitting.

The procedure then is as follows. At first four arbitrary dust rings are chosen according to the four regions where planetesimals are thought to be safe from planetary perturbations. From these first-guess rings it is to judge which dust ring (or combination of dust rings) provides most promising emission. Then, the remaining model parameters can be optimized to achieve a satisfactory agreement between model and observations. Proceeding this way of course strongly limits the degrees of freedom of the classical modeling approach and therefore the accuracy of the final model. Still, it is to stress once more that the goal of this study is not to perform a pure mathematical fit to the observations but to also use additional information available on the system to extract rough estimates on dust mass and locations to be compared to complementary investigations.

### The Modeling

To get a rough idea of the location of the dust belt(s) and the amount of dust in the HR 8799 system, the SED is modeled with *SEDUCE* assuming a double power-law surface number density of dust  $N \propto s^{-\eta} r^{-\xi}$ . Keeping in mind that SED interpretation is a degenerate problem and to decrease the number of free parameters, only  $\eta = 3.5$  and  $\xi = 1$  is considered. The dust composition is assumed to be astrosil with a bulk density of  $3.3 \text{ g cm}^{-3}$ . As the minimum grain size, the radiation pressure blowout radius, which amounts to  $\sim 5 \mu\text{m}$  for astrosilicate, is chosen. The maximum grain radius, which has little effect on the results, is arbitrarily set to  $1000 \mu\text{m}$ .

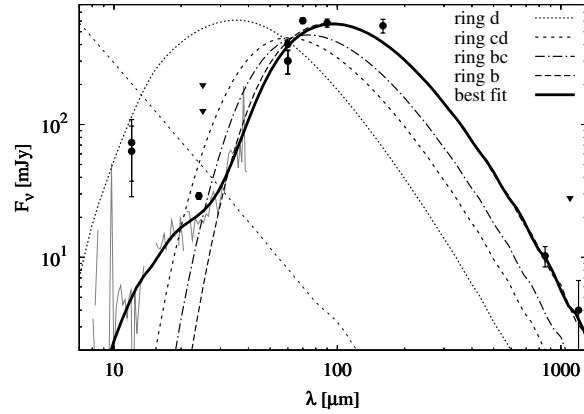


**Figure 4.1:** Excess emission of HR 8799 in the IR. The grey solid line is the *IRS* spectrum. The circles are the observed fluxes, and the triangles are upper limits. Dotted, short-dashed, dash-dotted, and long-dashed lines are the SEDs from the four first-guess dust rings (Table 4.2). The black solid line is the ‘best fit’.

**Table 4.2:** Locations and names of the first-guess dust rings.

ring location	ring extension [AU]	name
inside d	3 – 15	ring d
between d and c	28 – 32	ring cd
between c and b	45 – 60	ring bc
outside b	75 – 125	ring b

As already mentioned, at first the SEDs arising from the four hypothetical dust rings, corresponding to the four presumed stability regions for planetesimal evolution, with arbitrarily chosen extensions are calculated. In particular, the rings are located inside the orbit of the innermost planet HR 8799 d, between d and c, between c and b, and outside the orbit of the outermost planet HR 8799 b (Table 4.2). Dust masses are chosen in such a way as to reproduce the  $60 \mu\text{m}$  flux. The results are shown in Fig. 4.1.

Comparing the first-guess model SEDs with the available photometry and spectrometry observations reveals two issues. First, one single ring is not capable of reproducing the entire set of observations from the mid- to the far-IR. Even extending one of the rings inwards and/or outwards would not allow to produce the knee-like structure at  $\sim 20 - 30 \mu\text{m}$ . Second, if the  $10 \mu\text{m}$  silicate feature in the *IRS* spectrum is real, a substantial fraction of particles smaller than the blowout size are required.

Taking these discrepancies into account, two rings, ‘ring d’ and ‘ring b’, are combined and the lower size cutoffs and dust masses are fitted to the observations (recall that this is no more a degenerate task since all other parameters are fixed). In the ‘best fit’ model, which is shown as a solid line in Fig. 4.1, the minimum sizes are 2 and  $6 \mu\text{m}$  and the dust masses are  $1.4 \times 10^{-5} M_{\oplus}$  and  $4.2 \times 10^{-2} M_{\oplus}$  for the inner and outer ring, respectively. Since both dust reservoirs were considered decoupled, it is reasonable to assume two independent lower size cutoffs. As a word of caution, note that these estimates directly inherit the uncertainty of the *IRS* spectrum calibration, as mentioned above, which is a factor of several in dust mass. What is more, because the complementary investigations (see below) also are subject to large uncertainties it is refrained here to explore the confidence of the found dust disk model parameters.

### Sensibleness of the Modeling

The question arises whether these fits are physically reasonable. In particular, it is not immediately clear whether the blowout particles are really needed to reproduce the observations or not. Similar problems have already been encountered in other studies dealing with debris disks (e.g., around Vega, see Su et al. 2005). However, such inconsistencies can be overcome by considering a complete dynamical treatment of the specific disk without making significant changes in the disk location (see Chapter 5). Furthermore, the choice of power-laws for the spatial and size distributions is only a rough, albeit commonly used, approximation. More elaborate collisional studies (e.g., Krivov et al. 2006; Thébault & Augereau 2007) show clear deviations from this assumption, especially in the case of the dust size distribution where a wavy pattern arises from an underabundance of small particles induced by radiation blowout (see also Chapter 2.5.1 and 5.1). Thus, the impact of moderate variations in the slopes ( $0.1 \leq \xi \leq 1.9$  and  $2.5 \leq \eta \leq 4.5$ ) is checked. It turns out that the slope of the spatial distribution  $\xi$  has little effect on the results, moderately changing only the short-wavelength part in the SED from the inner dust ring. The size distribution slope  $\eta$ , however, affects the resulting emission appreciably. While for the inner ring the changes are still small (a steeper slope would amplify the silicate features at 10 and 20  $\mu\text{m}$  whereas a shallower distribution would wash them out, just as expected), similar changes in the outer ring would require a strong compensation by altering other disk parameters (which were fixed here for reasons of simplicity). The reason is that for the outer component both, the rise and the fall of the SED are well constrained by photometric observations. They place tight constraints on the width of the SED, in contrast to the inner ring where only the short-wavelength part of the SED is known. Since dust in the outer ring is much colder than in the inner ring it is no longer the strength of the features but the width of the SED that is affected by a different slope in the size distribution: the steeper the distribution, the narrower the SED. On any account, for the purpose of determining the rough location and mass of dust the simple fitting approach used here is sufficient.

Even ignoring the shortcomings of power-law dust distributions for the moment, uncertainties for the lower size cutoff are high. In case of the inner ring, silicate features in the IRS spectrum usually pose strong constraints on the minimum size. However, since the existence of such a feature in the HR 8799 spectrum is unclear, no firm statements can be made. For the outer dust ring, changes of the lower size cutoff can simply be compensated by changes of the upper size cutoff or outer edge of the inner ring leaving this parameter rather unconstrained. It is thus refrained here to check the impact of the minimum grain size.

Another question is, how well the edges of the outer and inner ring are constrained. To check this, these parameters are varied and, by leaving the lower cutoff size and dust mass as free parameters, the SED is fitted again. For the outer ring, reasonable fits with the inner edge between 75 and 120 AU and the outer edge between 125 and 170 AU (for  $\eta = 3.5$  and  $\xi = 1$ ) can be found. The outer edge in the inner ring can go from 15 down to 10 AU. In fact, the inner ring truncated at 10 AU provides even slightly better agreement with the IRS spectrum between 20 and 30  $\mu\text{m}$ . However, due to the calibration uncertainties it is difficult to assess the accuracy of the fit, which leaves the outer edge of the inner ring rather unconstrained. The inner edge of the inner ring can be as close to the star as 2 AU to conform to the IRS spectrum.

Concluding it is to remind that the found dust disk model is probably not the best possible fit. Considering also the parameters fixed here and exploring the whole parameter space with automated fitting routines would provide much more accurate (in a mathematical sense) models. However, since the main goal of this study is ‘just’ to get a rough insight in the possible architecture of the whole system HR 8799 (dust, planetesimals, and planets) the possibility of such a detailed fitting was abandoned. It was rather considered sufficient to implement a much



more simplistic algorithm to find rough estimates for those disk parameters most important for the comparison with the complementary information on the system: dust mass and location.

#### 4.2.4 Summary of the Results of Complementary Investigations

##### Central Star

Previous estimates of the stellar age using different methods range between 20 – 1 128 Myr, while most indicators are in favor of a rather young age. Independent from stellar properties, a statistical argument dealing with the dust disk's high infrared luminosity suggests a stellar age of  $\lesssim 50$  Myr (see Su et al. 2006, Fig. 5).

By taking the rotational period of HR 8799 and comparing it to typical periods of A-type stars, the possible range of inclinations could be restricted to  $13^\circ - 30^\circ$ . Hence, the system is seen nearly pole-on. This is in agreement with previous stability studies.

##### Planetary Evolution Models

Different evolution models were adopted to shed light on the possible planetary masses. The planets' luminosity, which were taken from the original discovery (Marois et al. 2008), and the age of the objects, which are usually interpreted as the stellar age, are required for such a prediction. Thus, accurate age determination as described above is crucial for reasonable usage of evolution models. Assuming a young age of  $\lesssim 50$  Myr leads to masses of less than 7 – 10  $M_{\text{Jup}}$ . However, ages of  $\gtrsim 160$  Myr result in companion masses above 13.6  $M_{\text{Jup}}$ , the limit for deuterium burning.

##### Stability of Planets

Using N-body simulations, the dynamical evolution of the planetary system was simulated as a function of planetary masses and the system's inclination. The configuration was assessed stable if the planets had not broken apart within 100 Myr. In the less restrictive case (low masses) inclinations of  $\lesssim 20^\circ$  were required for a stable configuration. Lower inclinations are also possible, but they would suggest masses below most model predictions. Furthermore, it turned out that the outer two planets must be locked in a 2 : 1 mean-motion resonance, while the same commensurability supports stability for the inner two planets. In many stable cases, however, only one of the resonances proves strong.

##### Stability of Planetesimals

Finally, an exemplary configuration was chosen so that the planetary distances were 24.6, 41.8, and 74.8 AU. Then, the evolution of 1 000 massless test particles (planetesimals) was followed over 100 Myr for the two cases of an intermediate-mass (7, 10, 10  $M_{\text{Jup}}$  for HR 8799 b, c, and d, respectively) and low-mass (5, 7, 7  $M_{\text{Jup}}$ ) system. From those particles, 200 were launched in the inner and 800 in the outer part of the system with initial semi-major axis of  $a_{\text{inner}} = 10 - 20$  AU and  $a_{\text{outer}} = 90 - 130$  AU. In the intermediate-mass case only 10 – 20% survived outside 120 AU in the outer ring. The region inside was almost completely cleared. Coming to the low-mass configuration, the survival fraction between 110 – 130 AU is about 15 – 70% higher. Planetesimals in the inner ring could even stay to 80 – 100% inside 11 AU. The outer edge of the inner ring changes from 13 to 15 AU for the intermediate-mass and low-mass system, respectively.

#### 4.2.5 Interpretation

##### Implications from this Study

Finally, the results for the different aspects of the system have to be gathered and compared. In particular the dust locations identified in SED fitting need to be cross-checked with planetesimal configurations which were found to be stable. As noted in Chapter 4.2.3, the far-IR to millimeter

part of the SED requires dust in the outer ring as close as 120 AU from the star. It was shown in the stability check that a significant fraction of planetesimals survives outside 120 AU after 100 Myr, at least in the low-mass case. In the nominal-mass case, the fraction of survivors is lower, but any firm conclusions appear premature, since the location of the outer ring is in fact not well-constrained (see Chapter 4.2.3). Next, the IRS spectrum interpretation requires dust in the inner ring at least 10 AU away from the star. This is comfortably within the stability zone inside the orbit of HR 8799 d for both the nominal-mass and low-mass cases. Moreover, 10 AU as quoted above is the distance where dust is required; as discussed in Chapter 4.2.3, the parent planetesimals would orbit closer to the star, being yet safer against the perturbations of the innermost planet than their dust. Summarizing, the analysis of the outer system might slightly favor the low-mass case, but would not really pose any additional strong constraints to the planetary masses.

As the investigations in Chapter 4.2.3 show, the coarse coverage of observations accounts for high uncertainties in the final results. The latter have thus to be taken with caution. New data on the dust portion of the system would be particularly promising. For instance, a better mid-IR photometry would result in more reliable predictions for the dust mass and location of the inner dust belt (“exozodi”). One could also think of near- and mid-IR interferometry observations which have proven very successful not only for exozodi studies, but also for stellar radius determination (see, e.g., Di Folco et al. 2004; Absil et al. 2006; di Folco et al. 2007; Absil et al. 2008). While HR 8799 is too faint to be observed with the presently operating CHARA/FLUOR and Keck Interferometry Nuller instruments (e.g., for CHARA the K-magnitude of  $\lesssim 4$  mag is needed, whereas HR 8799 has  $K = 5.2$  mag), this should be possible in the near future, for instance with VLTI/PIONIER and the LBTI Nuller.

More observational effort is required for the outer disk as well. Resolving the outer debris disk, especially in scattered light, would answer several key questions at a time. On the one hand, it would further constrain the inclination of the entire system and the orientation of its line of nodes on the sky plane, drastically reducing the parameter space assumed in the dynamical simulations. On the other hand, the precise location of the inner rim of the disk could place a direct upper limit on the mass of HR 8799 b, much in the same way as it was recently done for the Fomalhaut planet (Kalas et al. 2008; Chiang et al. 2009).

Once the location and masses of the dust belts are better constrained from observations, it will become possible to access the position, masses, and other properties of directly invisible planetesimal belts, that produce and sustain that dust. This could be achieved with the help of elaborate collisional models (see Chapter 5). The results could provide additional clues elucidating the formation history of the system.

### The Resolved Disk of HR 8799

Shortly after the investigations for this study had been completed, Su et al. (2009) published new *Spitzer*/IRS and *Spitzer*/MIPS observations. In particular they were able to resolve the dust disk at 24 and 70  $\mu\text{m}$ . In general, their findings are very similar to previous results. However, some differences occurred. As the inner ring could not be resolved with *Spitzer* the analysis also had to be based on the (new) IRS spectrum. The outer edge of the ring was found to be within 10 – 15 AU, in perfect agreement with the outcome in Chapter 4.2.3. The inner edge and the dust mass, however, differed with values of 6 AU and  $1.1 \cdot 10^{-6} M_{\oplus}$ . Such discrepancies stem from different assumptions for the grains’ bulk density and for the slope of the radial distribution and from a much narrower range of grain sizes (up to only 4.5  $\mu\text{m}$ ).

In terms of the outer ring, Su et al. (2009) split this component in a cold planetesimal disk with a wide range of grain sizes and an outer halo, which only comprises smaller, barely bound particles. The transition from the planetesimal belt to the halo was fixed at 300 AU. Similar

to investigations in Chapter 4.2.3, the outer truncation of the disk was not strictly constrained and was set to 1 000 AU. Given the disk is much more extended and the smallest sizes in the planetesimal ring are larger (10  $\mu\text{m}$ ), the new dust masses are about a factor of five higher ( $1.2 \cdot 10^{-1}$  and  $1.9 \cdot 10^{-2} M_{\oplus}$ ) than found in Chapter 4.2.3.

## 4.3 Discussion

### 4.3.1 Advantages

A clear advantage of this classical modeling approach is its simplicity. Analytical functions secure a quick evaluation of the dust distribution and the resulting thermal emission. This permits implementing automatic fitting routines that provide much more accurate results on a short timescale than simple eye fitting does, as it was presented above (e.g., Augereau et al. 1999; Meyer et al. 2004; Augereau et al. in prep.). Such modeling attempts can then provide first insight into the possible structure of observed disks.

### 4.3.2 Caveats and Disadvantages

In return, the model's greatest advantage is one of its largest shortcomings at the same time. Analytical expressions only partly reproduce the real distribution of dust in a debris disk and numerical simulations show clear deviations from the primarily used power-law dust distributions (Campo Bagatin et al. 1994; Durda & Dermott 1997; Thébault et al. 2003; Krivov et al. 2006; Löhne et al. 2008). Accordingly, fitting parameters are difficult to identify with underlying processes, although some values for the spatial and grain size distribution may be indicative for the leading processes like collisions, radiation pressure, or PR effect. Nevertheless, fitting results based on the classical modeling approach should always be taken with caution, and be interpreted in the light of the underlying physics. The next chapter gives an example, namely the system of Vega, of how this way of modeling can lead to dubious conclusions if the fitting results are taken too literally.

An additional disadvantage in this approach that could also be seen above, is the degeneracy of various model parameters. Changes of the lower size cutoff can for example be compensated by choosing the inner disk edge or the power-law slopes. To overcome this problem, additional information about the system is needed. Hence, resolved observations could constrain the location and the slope of the spatial distribution. The presence of planets imposes additional restrictions on the disk's extension, due to dynamical interaction between the planets and the disk (especially the planetesimals). Moreover, such knowledge limits the variability of different model parameters.

A last point is the lack of information about the planetesimal population. Analytical expressions like power-laws are only suitable to a certain extent to reproduce physical dust distributions, but there is also no reasonable way to extrapolate them to larger objects. This is especially unfortunate, because the collisional history rather shows up in the planetesimals than in smaller objects which have much shorter lifetimes. Furthermore, the impact of possible planets in a system is more direct and much stronger on the planetesimal evolution, while the distribution of small dust will mostly be affected by the changes in the planetesimal distribution and not by interaction with the planets directly. Constraints from discovered planets would therefore be more restrictive if applied to the planetesimal population.

Although all these limitations might appear too simple to account for the modeling problem, yet the application to HR 8799 is a good example of how this approach can provide an insight view into the considered system's possible structure. It therefore stresses the importance of critical cross checking and interpreting of the disk modeling results.

## Chapter 5

# Modeling from the Sources

*The most exciting phrase to hear in science, the one that heralds new discoveries, is not 'Eureka!' but 'That's funny...'*

ISAAC ASIMOV

### 5.1 The New Modeling Approach

One of the major disadvantages of the classical way of modeling is the difficulty to link results for the dust disk to the underlying processes for dust parent bodies. Nevertheless, with improving capacities of collisional debris disk codes the idea arose to use such tools to also account for the large disk constituents of observed systems (Krivov et al. 2000; Wyatt & Dent 2002; Thébault et al. 2003). During the last years these models have reached a state, where the whole disk can be simulated self-consistently (Thébault et al. 2003; Krivov et al. 2006; Thébault & Augereau 2007; Wyatt et al. 2007b; Löhne et al. 2008) and first efforts were made to combine the dynamical modeling with reproducing observed thermal emission properties in detail (Kenyon & Bromley 2008).

In the course of this work, `SEDUCE` and `SUBITO` were developed to derive observables from synthetic disk models which were produced with `ACE`. Those observables can then be used for model refinements. The modeling algorithm is as follows: Consider a debris disk system with a well covered SED and maybe also resolved images in thermal emission. Having chosen an initial distribution of planetesimals — the sources of observable dust — `ACE` can be started and after some time a complete synthetic debris disk can be compared with the observational data by extracting the dust portion and computing its thermal emission. With some experience, the found discrepancies can be connected to certain model parameters which concern either just the `ACE` simulations or both, the simulations and subsequent thermal emission calculations. After some (trial and error) iterations, the disk models will improve finally achieving a reasonable agreement with the observations. Note, that there is no way to influence the evolution of the disk, once a simulation is started. Therefore, in order to keep the number of iterations low, it is very important to make a good educated guess for the initial disk configuration. Additional knowledge about the system, like the discovery of planets, resolved observations of the disk, or the peak position in the SED, can be helpful for this purpose.

Some of the model parameters are similar to the classical way of modeling (see Chapter 4.1), but with slightly different meaning. For instance, the initial extension must be specified. This, however, does not refer to the extension of dust but of dust-producing planetesimals. Also the considered range of grain sizes is required. In contrast to the classical approach, the minimal size is usually chosen below the radiation pressure blowout, so that this particular value does not affect the simulation. The upper size cutoff is of small interest to the modeling, as it is usually large enough, so that the collisional cascade cannot reach this size regime, except for very old systems. The composition of disk constituents comes not only into play for the calculation of emission properties, but also for the dynamical interaction between stellar gravity and radiation and dust, and does thus juxtapose the classical way. Other parameters refer to the considered physical or dynamical processes, like the collisional prescription or planetesimal eccentricities, and are not included in the classical modeling approach.

Fundamental for this new approach of collisional modeling is the possibility to scale the `ACE` results as described in Chapter 2.5.2. Given an `ACE` simulation with a certain initial disk mass  $M_0$ , the SED at the given age of the system can be calculated using the `ACE-SEDUCE` interface. However, as a precise a priori estimate of the correct initial disk mass is nearly impossible, the

modeled SED typically shows a vertical offset from the observations. Using the mass scaling the number of ACE runs can be limited to a reasonable amount that makes this new collisional modeling approach feasible. This is of special importance, as this kind of modeling is much more time-consuming than the classical approach — one ACE simulation usually takes a few days, but this can be extended up to two weeks, depending on the assumed parameters and the age of the system to model.

To point out the special capacities of this modeling from the sources, Chapter 5.2 presents a first applicability check by modeling a grid of reference disks. In Chapter 5.3 a first in detail modeling of a well-observed system, namely the Vega system, is performed. Finally, Chapter 5.4 discusses the advantages and disadvantages of the new approach.

## 5.2 Application: Grid

(Results presented here are based on research that was carried out for “Krivov et al. (2008)”. The author’s contribution to this study was confined to the calculation of dust temperatures and reference SEDs, and to the selection and modeling of the observed debris disk systems. Additional results are included here for the sake of completeness. )

### 5.2.1 The Idea

Interestingly, replacing formal dust distributions with those coming out of dynamical modeling does (in first order) not increase the number of fitting parameters. In fact, just the opposite is true: the number of parameters is reduced and those parameters, still kept free, do all have clear astrophysical meaning. Most important are the location of the parent planetesimal belt and its current mass (Wyatt et al. 2007b).

However, incorporating a new disk model in a modeling approach is accompanied with a bulk of new effects of model parameters on the results, even if the parameters were already present in the old approach. Before starting with a detailed analysis of certain systems, it is therefore advisable to check the impact of the presumably most important parameters on the modeling result. To proceed in a systematic way, a grid of reference model debris disks is produced, resulting in a grid of reference model SEDs. As a byproduct, the grid can already be used to interpret available observational data.

Chapter 5.2.2 introduces the set of reference disks and specifies the model parameters. Chapter 5.2.3 presents the modeling results: size and spatial distribution of dust, dust temperatures, and the generated SEDs. Application to selected observed disks is made in Chapter 5.2.4.

### 5.2.2 Reference Disks

#### Central Star

The parameters of the central star (mass and photospheric spectrum) affect both the dynamics of solids (by setting the scale of orbital velocities and determining the radiation pressure strength) and their thermal emission (by setting the dust grain temperatures). Here the Sun (a G2 V dwarf with a solar metallicity) as a central star is chosen and its photospheric spectrum is calculated with the *NextGen* grid of stellar photosphere models (Hauschildt et al. 1999).

#### Collisions

The radii of solids in every modeled disk cover the interval from 0.1  $\mu\text{m}$  to 100 km. The upper limit of 100 km is justified by the fact that planetesimal accretion models predict larger objects to have a steeper size distribution and thus to contribute less to the mass budget of a debris disk (e.g., Kenyon & Luu 1999b). To describe the collisional outcomes, the same assumptions as presented in Chapter 2.4.2 are made. In particular  $Q_{D,s} = Q_{D,g} = 5 \times 10^6 \text{ erg g}^{-1}$ ,  $3b_g = 1.38$ , and  $3b_s = 0.37$  in Eq. (2.57) and  $\eta = 1.833$  in Eq. (2.65) are set.

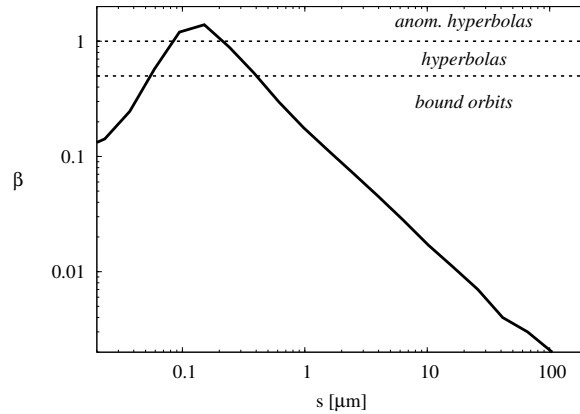


**Figure 5.1:** Radiation pressure to gravity ratio  $\beta$  for astrosil grains around the sun (G2 V star) as a function of their size. Horizontal lines at  $\beta = 0.5$  and  $\beta = 1.0$  show which particles typically move in bound elliptic orbits, in hyperbolas, as well as in anomalous hyperbolas.

**Table 5.1:** Description of reference disks.

Disk Identifier	Belt Location [AU]	Initial Disk Mass [ $M_{\oplus}$ ]	$a$ Range [AU]	$r$ Range [AU]
10EKBD @ 3AU	3	0.001	0.5 – 20	0.3 – 30
10EKBD @ 10AU	10	0.03	2 – 50	1 – 100
10EKBD @ 30AU	30	1	5 – 200	3 – 300
10EKBD @ 100AU	100	30	20 – 500	10 – 1000
10EKBD @ 200AU	200	200	30 – 1000	20 – 2000

### Optical Properties of Dust

An important issue is the choice of grain composition and morphology. These affect both the dynamical model (through radiation pressure efficiency as well as bulk density) and thermal emission model (through absorption efficiency). Here compact spherical grains composed of astrosil are assumed.

The  $\beta$  ratio for compact astrosil grains is shown in Fig. 5.1. The blowout limit,  $\beta = 0.5$ , corresponds to a grain radius of  $s = 0.4 \mu\text{m}$ . Note that the tiniest astrosil grains ( $\lesssim 0.1 \mu\text{m}$ ) would have  $\beta < 0.5$  again and thus could orbit the star in bound orbits. However, the dynamics of these small motes would be subject to a variety of effects (e.g., the Lorentz force) not included in the model, and their lifetimes may be shortened by erosion processes (e.g., stellar wind sputtering Czechowski & Mann 2010). Altogether, little contribution to the thermal emission in the mid-IR to sub-mm is expected from them. By setting the minimum radius of grains to  $0.1 \mu\text{m}$ , these grains are therefore not taken into account.

The spectral dependence of the absorption efficiency  $Q^{\text{abs}}$  of different-sized astrosil spheres is depicted in Fig. 5.2. For the sake of clarity it is preferred to show the absorption efficiency rather than the cross sections, which would span a much larger range of magnitudes.

### Parent Planetesimal Belts

To have a representative set of “reference” debris disks around sun-like stars, possible planetesimal rings centered at the semi-major axes of  $a = 3, 10, 30, 100,$  and  $200$  AU from the primary are considered. All five rings are assumed to have the same initial relative width (again, in terms of

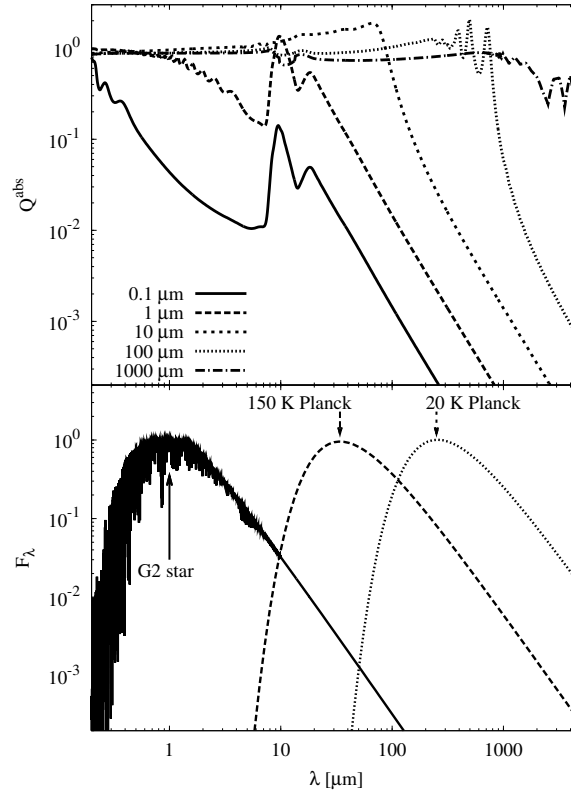


**Figure 5.2:** Top: absorption efficiency of astrosilicate compact spherical grains as a function of wavelength for different grain sizes. Bottom: the spectrum of a G2 V star and the Planck curves for 150 and 20 K (in arbitrary vertical scale) to indicate the spectral ranges most important for absorption and emission.

semi-major axis) of  $\Delta a/a = 0.2 (\pm 0.1)$  and to share the same semi-opening angle (the same as the maximum orbital inclination of the objects) of  $\varepsilon = 0.1$  rad. Orbital eccentricities of planetesimals are then distributed uniformly between 0.0 and 0.2, in accordance with the standard equipartition condition. The initial (differential) mass distribution of all solids is given by a power-law with the index 1.87, a value that accounts for the modification of the classical Dohnanyi's (1969) 1.833 through the size dependence of material strength (see, e.g., Durda & Dermott 1997).

The initial disk mass is taken to be  $1 M_\oplus$  for a 30 AU ring, roughly corresponding to ten (or slightly more) times the (Edgeworth-)Kuiper belt (EKB) mass (e.g., Gladman et al. 2001; Hahn & Malhotra 2005). For other parent ring locations, the initial mass is taken in such a way as to provide approximately the same volume density of material. Since the circumference of a ring  $2\pi a$ , its absolute width  $\Delta a$ , and vertical thickness  $2a\varepsilon$  are all proportional to  $a$ , the condition of a constant density requires the mass scaling  $\propto a^3$ . This corresponds to the initial mass ranging from  $\sim 0.001 M_\oplus$  in the 3 AU case to  $\sim 200 M_\oplus$  in the 200 AU case. With these values, all reference disks have about ten times the EKB density (10 EKBD).

That all the belts share the same volume density of material is purely a matter of convention. Instead, the surface density or the total mass could have been chosen to be the same. Given the scaling rules, as discussed in Chapter 2.5.2, none of these choices would have strong advantages or disadvantages. The same ACE runs automatically provide the results for disks of any other initial density (or mass).

All five reference disks are listed in Table 5.1. They were evolved with the collisional code, ACE, and all results were stored between the ages of 10 Myr and 10 Gyr at reasonable time steps. In what follows, self-explanatory identifiers like 10EKBD @ 10AU @ 300Myr are used to refer to a particular disk of a particular age.

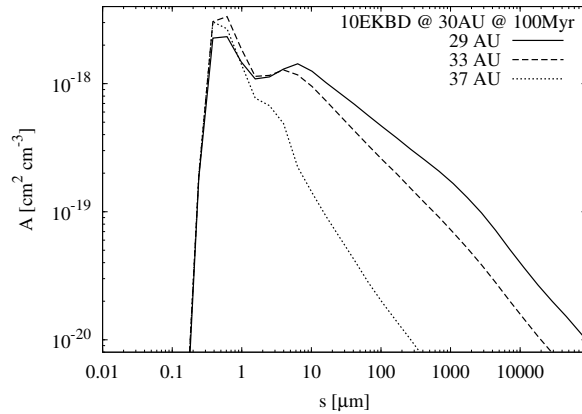


**Figure 5.3:** Size distribution in the 10EKBD @ 30AU @ 100 Myr disk at three different distances from the star.

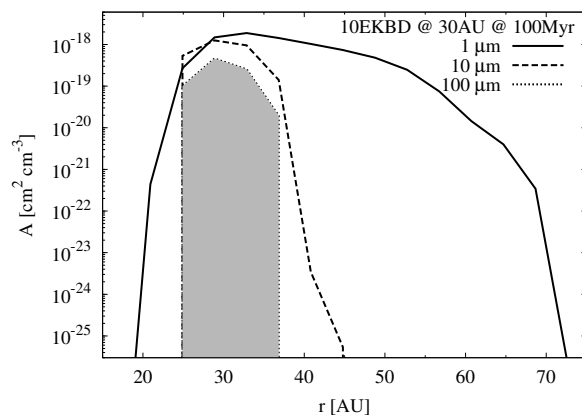


**Figure 5.4:** Spatial distribution of grains with three characteristic radii for the 10EKBD @ 30AU @ 100 Myr disk. The ring of the biggest particles shown (100  $\mu\text{m}$ , hatched area) is the narrowest. Its radial extension is nearly the same as that of the initial planetesimal ring; vertical “walls” are artifacts due to a discrete distance binning.

### 5.2.3 Results

As noted above, the collisional code ACE uses masses and orbital elements of disk particles as phase space variables. At any time instant, their phase space distribution is transformed to usual mass/size and spatial distributions. It is important to understand that mass/size distributions and spatial distributions cannot, generally, be decoupled from each other. Grains of different sizes have different radial distributions and conversely, the size distribution of material is different at different distances from the star.

A typical size distribution of solids is shown in Fig. 5.3 for one of the disks, namely 10EKBD @ 30AU @ 100Myr. Different lines correspond to different distances from the primary. As expected, the size distribution is the broadest within the parent ring of planetesimals. Farther out, it only contains grains which are small enough to develop orbits with sufficiently large apocentric distances due to radiation pressure.

The spatial distribution of material in the same disk is shown in Fig. 5.4. Here, different lines refer to different particle sizes. The ring of the biggest particles shown (100  $\mu\text{m}$ ), for which radiation pressure is negligible, nearly coincides with the initial ring of planetesimals (semi-major axes from 27 to 33 AU, eccentricities from 0.0 to 0.2, and hence radial distances from 22



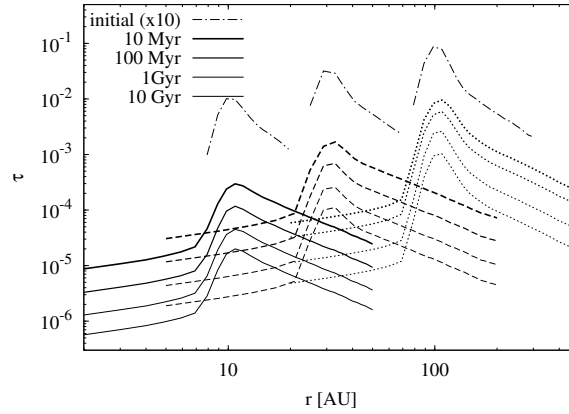


**Figure 5.5:** Radial profiles of the normal geometrical optical depth for three out of five basic runs (10EKBD @ 10AU, solid lines; 10EKBD @ 30AU, dashed; 10EKBD @ 100AU, dotted) at different ages. The thinner the line, the older the disk, as marked in the legend. The dash-dotted lines are initial optical depths, artificially enhanced by a factor of ten for a better visibility.

to 40 AU). The larger the particles, the more confined their rings. The rings are more extended outward with respect to the parent planetesimal ring than inward.

Radial profiles of the normal geometrical optical depth for three reference disks (planetesimal rings at 10, 30, and 100 AU) are depicted in Fig. 5.5. Initially, the peak optical depth of the disks is proportional to the distance of the parent ring, making the 100 AU disk ten times optically thicker than the 10 AU one. The subsequent collisional evolution of the disks depends on their initial mass and distance from the star, as explained in detail in Löhne et al. (2008) and in Chapter 2.5.2. Once a collisional steady state is reached (which is the case after 10 Myr for all three disks), the optical depth decays with time approximately as  $t^{-\xi}$ , where  $\xi \approx 0.3 - 0.4$ , i.e. roughly by one order of magnitude from 10 Myr to 10 Gyr. In a steady-state regime, the optical depth is proportional to  $r^{1+1.3\xi} \sim r^{1.5}$  (see Appendix A, Example 1 in Krivov et al. 2008). This explains why, at any age between 10 Myr and 10 Gyr, the 100 AU ring is  $\sim 30$  times optically thicker than the 10 AU one.

### Dust Temperatures

Figure 5.6 shows the dust temperatures as a function of two variables: grain distances from the star and their radii. In a parallel scale on the right, typical size distributions (cf. Fig. 5.3) are shown. Similarly, under the temperature plot, typical radial profiles of the disks are drawn (cf. Fig. 5.4). This enables a direct “read-out” of the typical<sup>1</sup> temperature in one or another disk. For example, 130 K at 10 AU, 90 K at 30 AU, and 50 K at 100 AU can be found.

These values are noticeably higher than the blackbody values of 88 K, 51 K, and 28 K, respectively. The reason for these big deviations and for the S-shaped isotherms in Fig. 5.6 is the astrosil’s spectroscopic properties with relatively high absorption at visible wavelengths and steeply decreasing absorption coefficient at longer wavelengths (see Fig. 5.2). The cross section-dominating astrosil grains are in a size range where the absorption efficiency for visible and near-IR wavelengths (around 1  $\mu\text{m}$ ) has already reached the blackbody value, while emission is still rather inefficient. With the enhancement of the emission efficiencies relative to the “saturated” absorption, temperatures drop drastically for somewhat larger grains. The larger the distance from the star (yielding lower average temperature and lower emission efficiency), the wider the size range over which the temperature decreases, and the stronger the temperature dif-

<sup>1</sup>“Typical” in the sense that it is the temperature of cross-section dominating grains in the densest part of the disk.

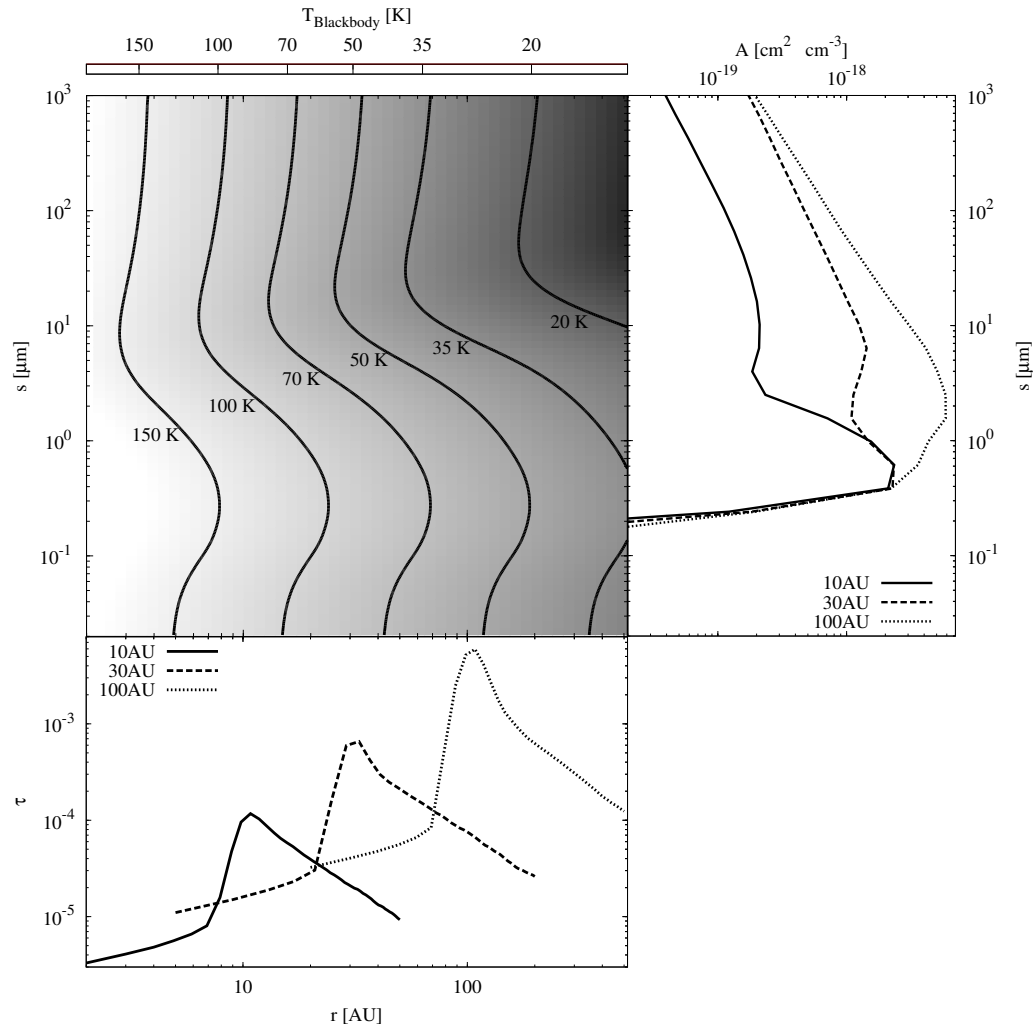


**Figure 5.6:** The left upper plot shows the equilibrium temperature of dust particles as a function of their distance from the star (horizontal axis) and size (vertical axis). Contours are isotherms. The blackbody dust temperatures are given along the upper edge of the plot for comparison. In the right-hand plot the size distribution at the “central” distance of the systems (10 AU, solid; 30 AU, dashed; and 100 AU, dotted) at 100 Myr is given. The lowest left plot gives the normal optical depth for the same three disks as a function of distance to the star. An intersection of a horizontal straight line going through the maximum of the size distribution in a disk (right) with a vertical line through the peak of its radial profile (bottom) provides the typical dust temperature in that disk.

ference between small and large grains. This explains why the S shape of the isotherms gets more pronounced from the left to the right in Fig. 5.6.

Further, note that Mie resonances can increase the absorption/emission efficiencies even beyond unity for wavelengths somewhat longer than the grain size (see 1, 10, and 100  $\mu\text{m}$  curves in Fig. 5.2). This explains the temperature maximum for grains of about 0.3  $\mu\text{m}$  radius (“resonance” with the stellar radiation maximum) and the minimum with temperatures even below the blackbody values for grains with 10 – 50  $\mu\text{m}$  radius (“resonance” with the blackbody emission peak).

### Spectral Energy Distributions

First of all a single, “typical” SED for one of the disks is considered. Fig. 5.7 shows the result of the SEDUCE calculation for the 1EKBD @ 30AU @ 100Myr disk with a thick solid line. The

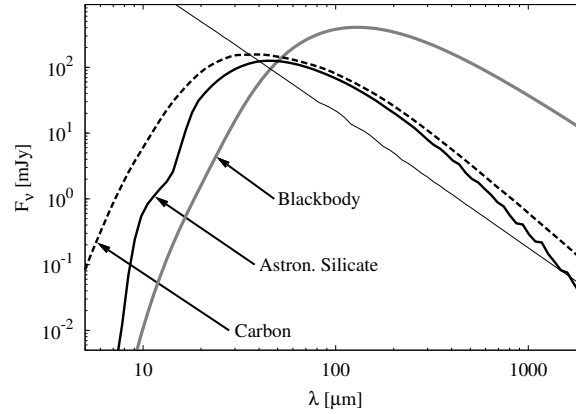


**Figure 5.7:** The emission from one and the same, 1EKBD @ 30AU @ 100Myr, disk, calculated under different assumptions about absorbing and emitting properties of dust grains: blackbody, astrosil (the nominal case), and amorphous carbon particles. Thin solid line: photosphere of a G2 V star.

SED peaks at about 50  $\mu\text{m}$ , which is consistent with the dust temperatures (Fig. 5.6). The hump at  $\sim 10$   $\mu\text{m}$  is due to a classical silicate feature, as discussed below.

For comparison, the SEDs for the same disk, but under different assumptions about the absorbing and emitting properties of grains, were calculated and over-plotted in Fig. 5.7: in a blackbody approximation (grey line) and for amorphous carbon (dashed line). Note that the difference applies only to the calculation of thermal emission. In other words, the dynamical modeling was still done by assuming the radiation pressure response of astrosil and not of perfectly absorbing or carbon particles, but it was assumed that the grains absorb and emit like a blackbody or carbon when calculating the thermal emission. There is a striking difference between the curves, especially the blackbody SED deviates from the others dramatically. The blackbody assumption leads to a strong increase of the total flux as well as to a shift of the maximum in the SED from 50 to 130  $\mu\text{m}$ ! In addition the excess drops towards longer wavelengths much slower than in the case of the astronomical silicate. In fact, it will never intersect the stellar photospheric flux.

To proceed, the set of SEDs for the grid of reference disks is inspected. Some of them are shown in Fig. 5.8. The main features of these plots reveal no surprises. The absolute level of excess emission is higher for more massive disks, as well as for distant ones (which is just the consequence of the assumed “same-density” scaling, as described in Chapter 5.2.2, see also Fig. 5.5). The amount of dust emission is roughly comparable with the photospheric emission for the mid-aged 1EKBD @ 30AU disk. This is consistent with the known fact that a several Gyr-old EKB counterpart would only slightly enhance the photospheric emission even at the “best” wavelengths. The position of the maximum emission ranges from  $\sim 30$   $\mu\text{m}$  for the 10 AU disk to  $\sim 70$   $\mu\text{m}$  for the 100 AU disk. Note that blackbody calculation would predict the emission to peak at longer wavelengths; beyond 100  $\mu\text{m}$  for a 100 AU disk.

Again, the hump seen in all SEDs slightly below 10  $\mu\text{m}$  is due to a silicate feature in  $Q^{\text{abs}}$ ; furthermore, some traces of the second feature at 20  $\mu\text{m}$  are barely visible. This explanation is supported by Fig. 5.2, which shows the absorption efficiency feature in this spectral range for small particles. This becomes even more obvious by comparing the contribution of the different grain size decades. For 0.1 – 1  $\mu\text{m}$  particles the hump is more pronounced than for larger ones (see Fig. 5.9, left), as it is the case for the absorption efficiency. Further on, the 10  $\mu\text{m}$  “excess” becomes less visible for most distant disks (Fig. 5.8, top to bottom), where the average temperatures are lower, the maximum emission shifts to longer wavelengths, and therefore the Planck curve at  $\lambda \sim 10 - 20$   $\mu\text{m}$  is steeper.

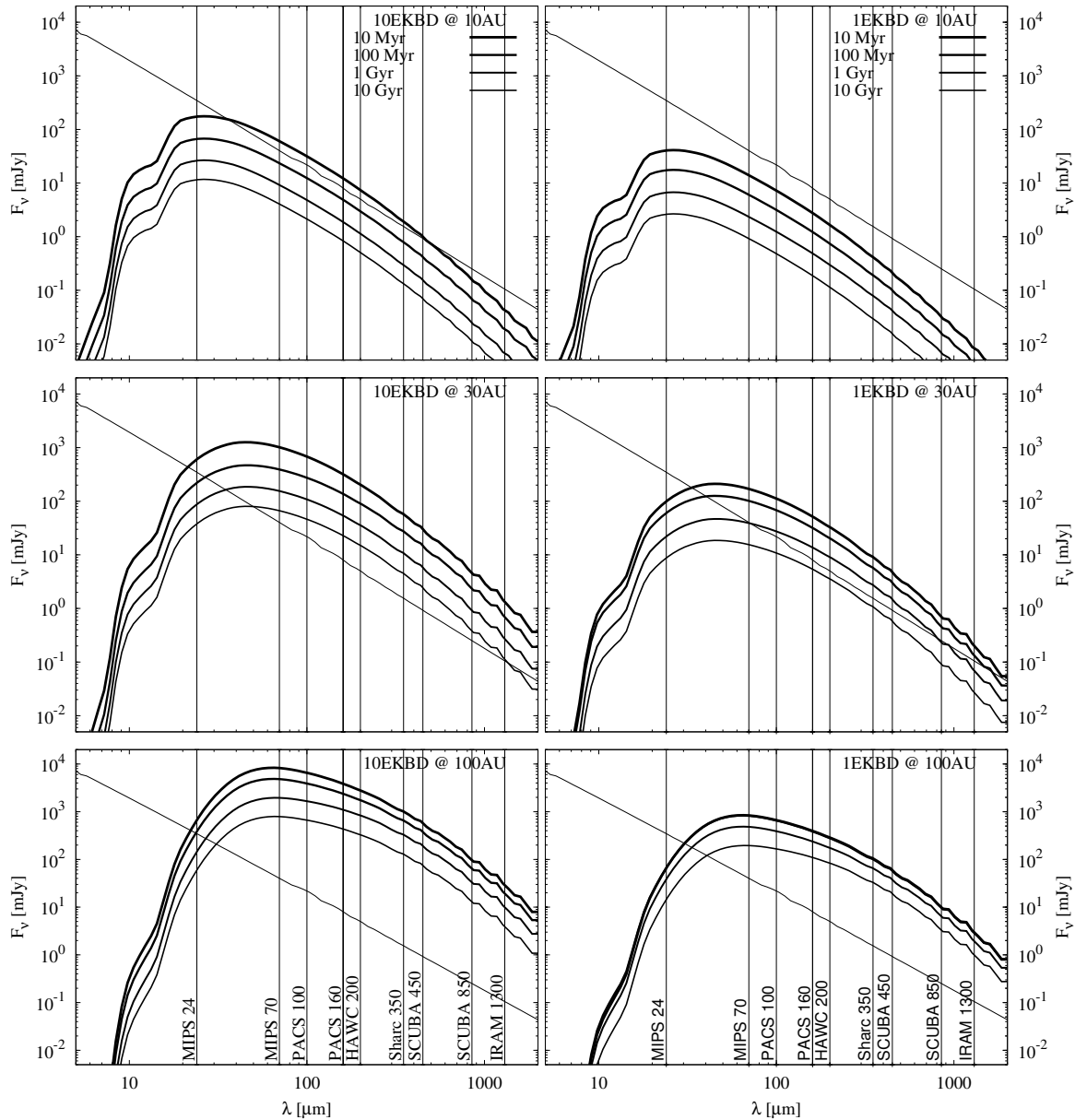


**Figure 5.8:** SEDs of disks stemming from planetesimal rings with different masses at different locations and at different time steps. To obtain the absolute values of fluxes, a distance of 10 pc was assumed. Left: reference disks (10 EKBD), right: less massive disks (1 EKBD). The results for the latter have been obtained with the aid of Eq. (3.2). From top to bottom: the SEDs of the simulated planetesimal rings at 10, 30 and 100 AU. In each panel, lines of decreasing thickness correspond to the ages of 10 Myr, 100 Myr, 1 Gyr, and 10 Gyr. Note that the evolution of the 1EKBD @ 100AU disk at the beginning is very slow, so that the SEDs at 10 and 100 Myr are indistinguishable. Vertical lines indicate centers of observational bands of several instruments (in  $\mu\text{m}$ ): Spitzer MIPS (24, 70, 160), Herschel PACS (70, 100, 160), Sofia HAWC (200), CSO Sharc (350), JCMT SCUBA/SCUBA 2 (450, 850), MPIfR IRAM (1300). A thin line from top left to bottom right is the stellar photosphere.

The left panels in Fig. 5.9 illustrate relative contributions of different-sized particles to the full SEDs. This is useful to get an idea which instrument is sensitive to which grain sizes. The blowout grains radii less than  $0.4 \mu\text{m}$  make only modest contribution to the flux even at  $10 \mu\text{m}$ . The mid-IR fluxes are always dominated by bound grains with  $0.4 - 1 \mu\text{m}$  radii (for the 10 AU and 30 AU rings) or those with  $0.4 - 10 \mu\text{m}$  (for the 100 AU ring). In the far-IR, particles up to

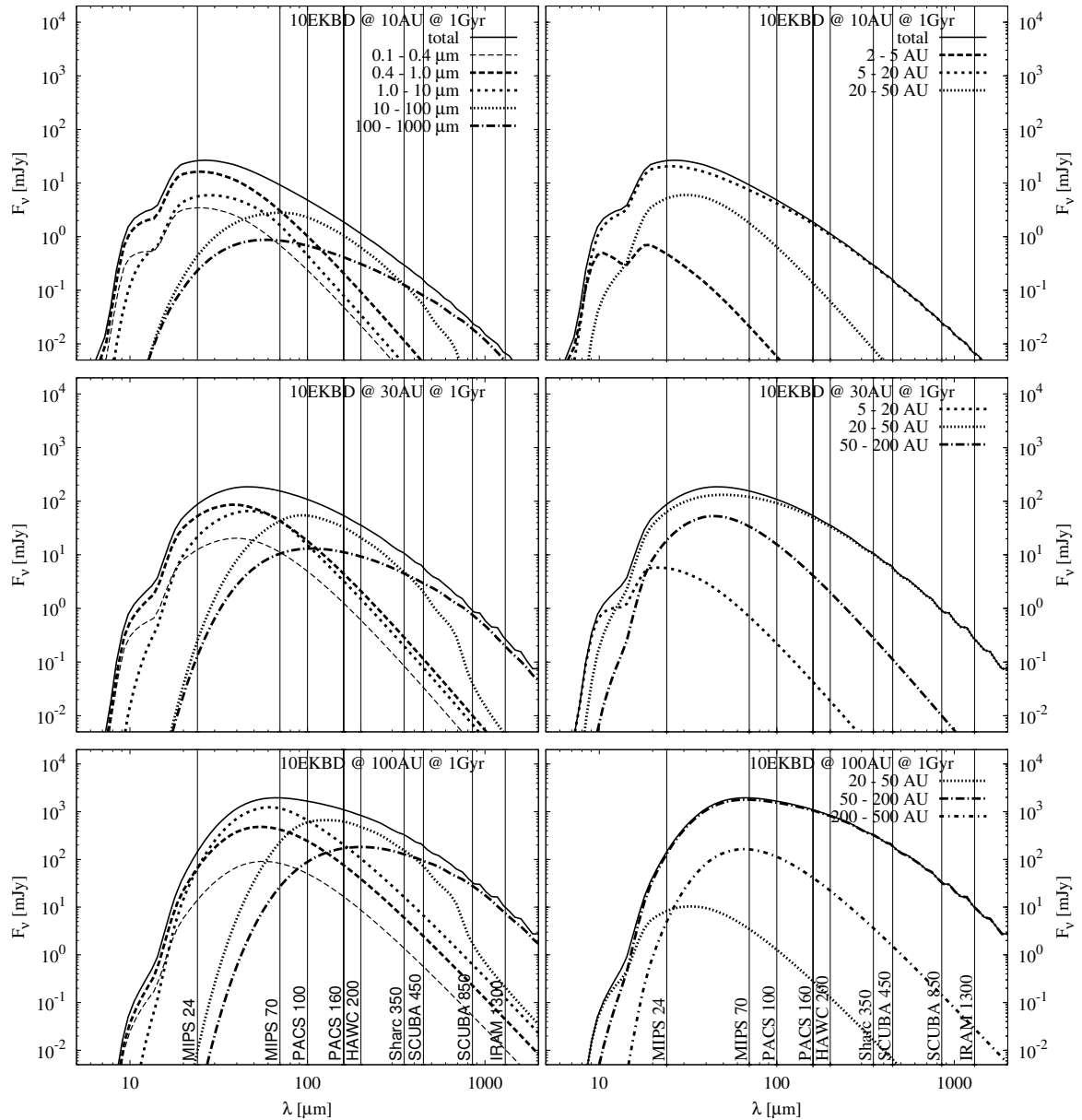


**Figure 5.9:** Contribution of individual grain size decades (shown with different line-styles in the left panel) and individual radial annuli of the disks (different line-styles, right) to the SED. As the grain blowout radius is  $\sim 0.4 \mu\text{m}$ , see Fig. 5.1, in the left panels the lowest size decade was split into blowout grains with  $s \in [0.1 \mu\text{m}, 0.4 \mu\text{m}]$  and bound ones with  $s \in [0.4 \mu\text{m}, 1.0 \mu\text{m}]$ . Panels from top to bottom correspond to planetesimal rings at 10, 30 and 100 AU. The initial density of all disks is 10 EKBD and their age is 1 Gyr.

100  $\mu\text{m}$  in size play a role. The greatest effect on the sub-mm fluxes is that of 100  $\mu\text{m}$  – 1 mm grains.

The position of the different maxima in Fig. 5.9 can be understood by comparing the size decades to the dust temperature plot (Fig. 5.6). Particles of 0.1 – 1  $\mu\text{m}$  are on the average a bit warmer than particles of 1 – 10  $\mu\text{m}$ . However, the size distribution shows that the second decade is dominated by particles only slightly larger than 1  $\mu\text{m}$ , which are still nearly as warm as the particles in the decade below. Thus, the maxima of the corresponding SED contributions are shifted only slightly. Nevertheless, the smaller motes are more sensitive to radiation pressure. A significant fraction of these is therefore located further away from the star which causes the SED

**Table 5.2:** Stellar parameters of Sun-like stars.

Star	$T_{\text{eff}}$ [K]	$\log L_*/L_\odot$	D [pc]	Age [Myr]
HD 377	5852 <sup>a)</sup>	0.09 <sup>a)</sup>	40 <sup>a)</sup>	32 <sup>a)</sup>
HD 70573	5841 <sup>a)</sup>	-0.23 <sup>a)</sup>	46 <sup>a)</sup>	100 <sup>a)</sup>
HD 72905 <sup>b)</sup>	5831 <sup>a)</sup>	-0.04 <sup>a)</sup>	13.85 <sup>c)</sup>	420 <sup>c)</sup>
HD 107146	5859 <sup>a)</sup>	0.04 <sup>a)</sup>	29 <sup>a)</sup>	100 <sup>+100</sup> <sub>-20</sub> <sup>d)</sup>
HD 141943	5805 <sup>a)</sup>	0.43 <sup>a)</sup>	67 <sup>a)</sup>	32 <sup>a)</sup>

Notes: <sup>a)</sup> Hillenbrand et al. (2008), <sup>b)</sup> A G1.5 star, <sup>c)</sup> Trilling et al. (2008), <sup>d)</sup> Moór et al. (2006).

of 0.1 – 1  $\mu\text{m}$  objects to drop slightly slower than the SED for 1 – 10  $\mu\text{m}$  particles. It is the step to the next decade where the decrease of temperature becomes very obvious by a large shift of the maximum. From that size on, the emission maxima stay nearly at the same position (in fact the maxima are shifted again to smaller wavelengths) as the temperature changes only marginally.

Similar to the contribution of the different size decades in the left panel, the right panels in Fig. 5.9 demonstrate the contribution of the different radial parts of the disk to the total SED. As expected, most of the flux comes from the medium distances as this is the location of the birth ring. The second largest contribution is made by the outer part of the ring.

## 5.2.4 Modeling of Selected Debris Disks

### Measured Fluxes

To test the plausibility of the models, several nearby sun-like stars known to possess debris dust were selected. Published datasets were used to search for stars with (i) spectral classes most likely G2 V (or very close), and (ii) unambiguous excesses probed in a wide range of wavelengths from near- to far-IR or sub-mm. The resulting five stars and their properties are listed in Table 5.2, a summary of observational data on them is given in Table 5.3, and the disk properties as derived in original papers are collected in Table 5.4. The data include those from various surveys with *IRAS*, *ISO*, *Spitzer*, *Keck II*, and *JCMT* (Table 5.3). The estimated ages of the systems range from 30 – 400 Myr (Table 5.2) and the fractional luminosities from  $\sim 10^{-5}$  –  $\sim 10^{-3}$  (Table 5.4). The collected data points for the sample stars (photosphere + dust) are plotted in Fig. 5.10.

### Observed Excesses

Symbols in Fig. 5.11 represent the observed excess emission for the sample stars. In the cases where the photospheric subtraction was done in the source papers, the published data points were used. In the cases where only the total measured flux (star + dust) was given, the procedure was as follows. Three *IRAC* points (3.6, 4.5, and 8.0  $\mu\text{m}$ ) were fitted by an appropriate *NextGen* model (Hauschildt et al. 1999), and the resulting photospheric spectrum was subtracted from the fluxes measured at longer wavelengths. As far as the data quality is concerned, the best case is clearly HD 107146, where the data points cover a broad range between 10  $\mu\text{m}$  and 1 mm. In other cases, the longest wavelengths probed lay at 70 – 160  $\mu\text{m}$ . As a result, it is sometimes unclear where exactly the excess peaks. This is exemplified by HD 70573, where the 160  $\mu\text{m}$  point has a huge error bar.

Yet before any comparison with the modeled SEDs, the resulting points in Fig. 5.11 allow several quick conclusions. Notwithstanding the paucity of long-wavelength data just discussed, in all five systems the excess seems to peak at or slightly beyond 100  $\mu\text{m}$ , suggesting a “cold EKB” as a source of dust. Additionally, in all systems except for HD 377, a warm emission at  $\lambda < 20 \mu\text{m}$  seems to be present, implying a closer-in “asteroid belt”.

**Table 5.3:** Observational data for the five G2 stars and their disks.

Star	Instrument, $\lambda$ [ $\mu\text{m}$ ]	Reference
HD 377	<i>IRAC</i> 3.6/4.5/8.0	Hillenbrand et al. (2008)
	<i>IRAS</i> 13/33	Hillenbrand et al. (2008)
	<i>IRAS</i> 60	Moór et al. (2006)
	<i>MIPS</i> 24/70/160	Hillenbrand et al. (2008)
HD 70573 <sup>a)</sup>	<i>IRAC</i> 3.6/4.5/8.0	Hillenbrand et al. (2008)
	<i>IRS</i> 13/33	Hillenbrand et al. (2008)
	<i>MIPS</i> 24/70/160	Hillenbrand et al. (2008)
HD 72905	<i>IRAC</i> 3.6/4.5/8.0	Hillenbrand et al. (2008)
	<i>IRS</i> 13/33	Beichman et al. (2006a)
	<i>IRAS</i> 12/25	Spangler et al. (2001)
	<i>ISOPHOT</i> 60/90	Spangler et al. (2001)
	<i>MIPS</i> 24	Bryden et al. (2006)
HD 107146 <sup>b)</sup>	<i>MIPS</i> 70	Hillenbrand et al. (2008)
	<i>IRAC</i> 3.6/4.5/8.0	Hillenbrand et al. (2008)
	<i>LWS</i> 11.7/17.8	Williams et al. (2004)
	<i>IRS</i> 13/33	Hillenbrand et al. (2008)
	<i>IRAS</i> 60/100	Moór et al. (2006)
	<i>MIPS</i> 24/70	Hillenbrand et al. (2008)
HD 141943	<i>SCUBA</i> 450/850	Williams et al. (2004)
	<i>IRAC</i> 3.6/4.5/8.0	Hillenbrand et al. (2008)
	<i>IRS</i> 13/33	Hillenbrand et al. (2008)
HD 141943	<i>MIPS</i> 24/70	Hillenbrand et al. (2008)

Notes: <sup>a)</sup> A planet host star (Setiawan et al. 2007) <sup>b)</sup> Resolved in V and I bands (Ardila et al. 2004), at 350 and 450  $\mu\text{m}$  (Williams et al. 2004), and at 3 mm (Carpenter et al. 2005)

### Comparison of Measured and Modeled SEDs

Now the observed dust emission and the modeled emission can be compared. The goal here is not to provide the best fit to the observations possible with the new modeling approach, but rather to demonstrate that a set of reference disks modeled in the previous sections can be used to make rough preliminary conclusions about the planetesimal families.

To make such a comparison, the following procedure is employed:

1. For each star, it is checked whether only cold or cold + warm excess emission is present. In the former case (HD 377), the data points are fitted with a single “cold” reference disk. In the latter case (all other systems), a two-component model is invoked: a close-in 3 AU disk and an appropriate cold disk.

2. The location of the cold planetesimal belt is chosen according to the measured peak wavelength: 100 AU (HD 72905 and HD 141943) or 200 AU (HD 377, HD 70573, and HD 107146).

3. Both reference SEDs, “warm” and “cold” (or only one for HD 377) are scaled vertically to come to the observed absolute flux. Physically, it necessitates a change in the initial disk mass. However, it is not sufficient to change the initial disk mass by the ratio of the observed flux and the flux from a reference disk. The reason is that a change in the initial mass also alters the rate of the collisional evolution, whereas the “right” flux at a fixed time instant, namely the age of the system (Tab. 5.2), is needed. Therefore, the scaling, as explained in Chapter 3.2.1, is applied. In

**Table 5.4:** Previously derived disk properties.

Star	$T_{\text{dust}}$ [K]	$R_{\text{dust}}$ [AU]	$M_{\text{dust}}$ [ $M_{\oplus}$ ]	$L_{\text{dust}}/L_{*}$
HD 377	58 <sup>a),1</sup>	23 <sup>a),5</sup>	$3.98 \times 10^{-4}$ <sup>a),8</sup>	$3.98 \times 10^{-4}$ <sup>a),11</sup> $(4.0 \pm 0.3) \times 10^{-4}$ <sup>f),12</sup>
HD 70573	41 <sup>a),1</sup>	35 <sup>a),5</sup>	$2.0 \times 10^{-5}$ <sup>a),8</sup>	$1.0 \times 10^{-4}$ <sup>a),11</sup>
HD 72905	103 <sup>a),1</sup>	7 <sup>a),5</sup>	$1.58 \times 10^{-6}$ <sup>a),8</sup>	$2.0 \times 10^{-5}$ <sup>a),11</sup>
	63 – 67 <sup>b),3</sup>	12.2 – 15.9 <sup>b),3</sup>	$3.3 \times 10^{-6}$ <sup>b),3</sup>	$2.9 \times 10^{-5}$ <sup>b),13</sup>
	123 <sup>g),2</sup>	6.2 <sup>g),5</sup>		$(0.6 – 1.5) \times 10^{-5}$ <sup>g),14</sup> $1.6 \times 10^{-5}$ <sup>e),15</sup> $2.8 \times 10^{-4}$ <sup>g),16</sup>
HD 107146	52 <sup>a),1</sup>	30 <sup>a),5</sup>	$1.26 \times 10^{-3}$ <sup>a),8</sup>	$4.94 \times 10^{-4}$ <sup>a),11</sup>
		13.6 – > 200 <sup>a),6</sup>	$3.2 \times 10^{-7}$ <sup>c),9</sup>	$(9.2 \pm 0.9) \times 10^{-4}$ <sup>f),12</sup>
	55 <sup>d),2</sup>	29 <sup>d),5</sup>	$8.99 \times 10^{-2}$ <sup>d),10</sup>	$9.5 \times 10^{-4}$ <sup>d),12</sup>
	51 <sup>h),4</sup>	> 31 – 150 <sup>h),7</sup>	0.1 <sup>h),4</sup>	$1.2 \times 10^{-3}$ <sup>h)</sup>
HD 141943	85 <sup>a),1</sup>	18 <sup>a),5</sup>	$7.94 \times 10^{-5}$ <sup>a),8</sup>	$1.58 \times 10^{-4}$ <sup>a),11</sup>
		8.6 – 40 <sup>a),6</sup>		

Notes: <sup>a)</sup> Hillenbrand et al. (2008), <sup>b)</sup> Beichman et al. (2006a), <sup>c)</sup> Carpenter et al. (2005), <sup>d)</sup> Rhee et al. (2007), <sup>e)</sup> Bryden et al. (2006), <sup>f)</sup> Moór et al. (2006), <sup>g)</sup> Spangler et al. (2001), <sup>h)</sup> Williams et al. (2004).

Comments: <sup>1</sup> Color temperature (33 – 70  $\mu\text{m}$ ) from blackbody SED fitting. <sup>2</sup> From SED fitting using a single temperature blackbody. <sup>3</sup> From SED fitting using 10  $\mu\text{m}$  silicate grains with a temperature profile following a power law (favored model in Beichman et al. (2006a)). <sup>4</sup> From single temperature SED fitting using a modified blackbody and a mass absorption coefficient  $\kappa_{850} = 1.7 \text{ cm}^2 \text{ g}^{-1}$ . <sup>5</sup> Derived from  $T_{\text{dust}}$  assuming blackbody (lower limit). <sup>6</sup> Extended ring derived from blackbody SED fitting assuming a constant surface density. <sup>7</sup> Inner border derived from SED fitting, outer border taken from resolved image. <sup>8</sup> Derived from fractional luminosity for an average grain size of  $\langle a \rangle = 10 \mu\text{m}$  and a density of  $\rho = 2.5 \text{ g cm}^{-3}$ . <sup>9</sup> Derived for  $T_{\text{dust}} = 40 \text{ K}$  using a frequency dependent mass absorption coefficient. <sup>10</sup> Derived from sub-mm observations using a dust opacity of  $1.7 \text{ cm}^2 \text{ g}^{-1}$  at 850  $\mu\text{m}$ . <sup>11</sup> Derived from  $T_{\text{dust}}$  and  $R_{\text{dust}}$  using Stefan-Boltzmann relation. <sup>12</sup>  $L_{\text{dust}}/L_{*} = L_{\text{IR}}/L_{\text{bol}}$ . <sup>13</sup>  $L_{\text{dust}}$  obtained by integrating *IRIS* spectrum (10 – 34  $\mu\text{m}$ ) after extrapolation to 70  $\mu\text{m}$ . <sup>14</sup>  $L_{\text{dust}}$  is derived from the SED fitting and  $L_{*}$  is obtained by integrating the corresponding Kurucz model. <sup>15</sup> Minimum value, derived from the 70  $\mu\text{m}$  measurement. <sup>16</sup>  $L_{*}$  is the stellar bolometric luminosity and  $L_{\text{dust}}$  is the sum of the luminosities in each (*IRAS*) wavelength band with a correction (for longer wavelengths).

systems with both warm and cold emission, this is done separately for the inner and outer disk.

The results presented in Fig. 5.11 with lines show that the modeled SEDs can, generally, reproduce the data points within their error bars. Again, the judgment should take into account the fact that just one or two pre-generated SEDs for a rather coarse grid of reference disks were used. Much better fits would certainly be possible if a more exact positioning of the parent bodies' belts and variation of additional model parameters were allowed (see Chapter 5.3). Dust opacities, initial distributions of planetesimals' sizes and orbital elements, as well as their mechanical properties that were fixed in modeling of the collisional outcomes would all be at disposal for this purpose. Further, more than two-component planetesimal belts could be astrophysical relevant as well, as is the case in the solar system (asteroid belt, different cometary families, and various populations in the EKB).

Finally, interpretation of the fitting results is needed, trying to recover the properties of dust-producing planetesimal belts. Table 5.5 lists them for all systems. The most important information is the deduced mass and location of the belts.



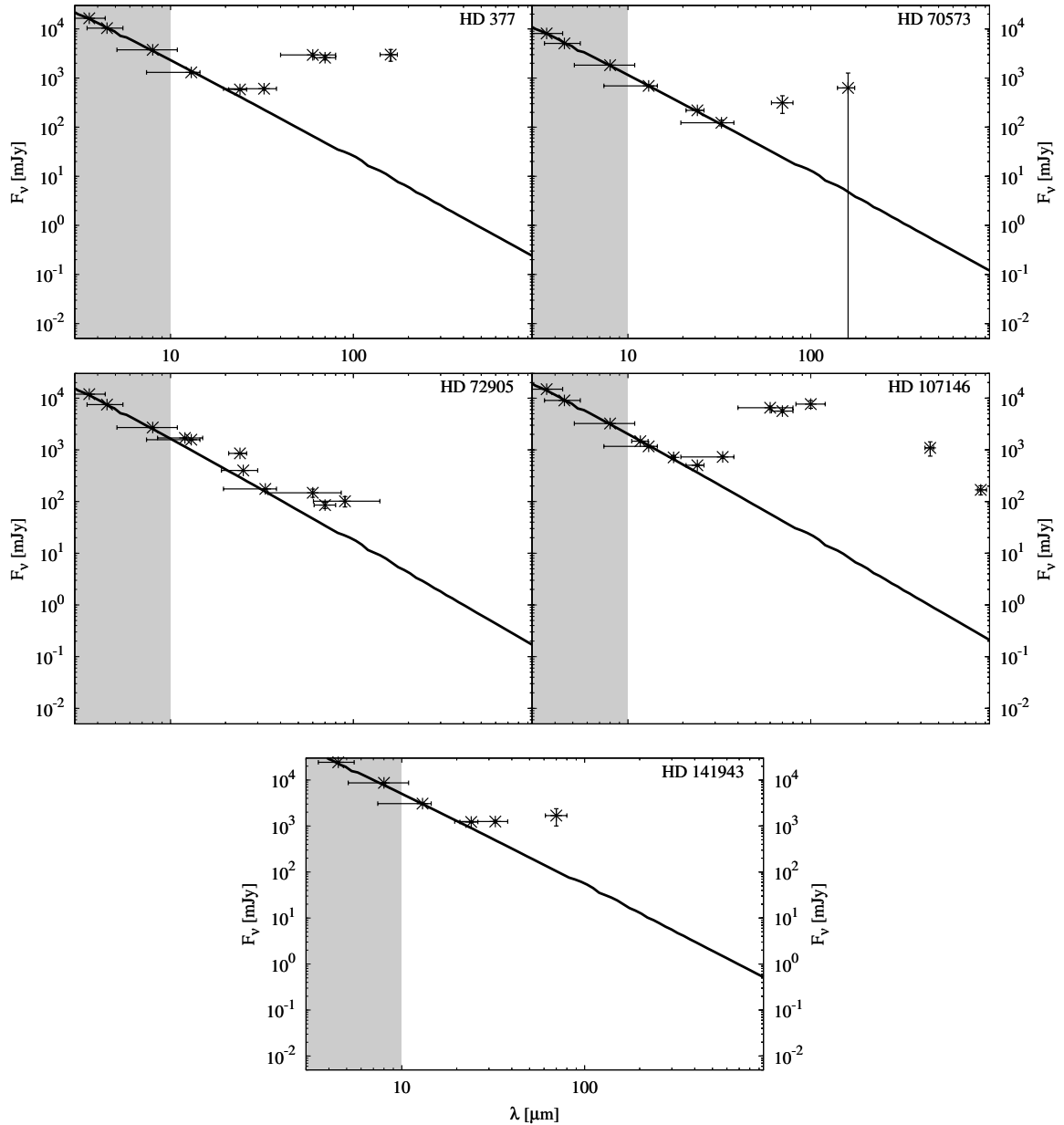


**Figure 5.10:** Observational data for five selected G2 V stars. Note that all fluxes have been scaled to the same standard distance of 10 pc. Symbols in the left-hand, grey-shaded part of each panel ( $\lambda < 10 \mu\text{m}$ ) are *IRAC* observations. They are used to find an appropriate Hauschildt model to the photosphere (thin solid line), assuming that no excess is already present in the near-IR. Vertical error bars are  $1\sigma$  observational uncertainties, taken from the source papers. Horizontal bars indicate the band width of the respective detector.

### Results for Hot Dust

As far as the hot dust components in four out of five systems are concerned, the results show that these can be explained by “massive asteroid belts” with roughly the lunar mass in bodies up to  $\sim 100$  km in size, located at 3 AU, with a width of  $\sim 1$  AU. However, the quoted distance of inner components — 3 AU — is only due to the fact that this is the smallest disk in the grid. This distance can only be considered as an upper limit: the SEDs seem perfectly compatible with disks as far in as 0.3 AU, as suggested for the case of HD 72905 (Wyatt et al. 2007b).

What is more, even the very fact that hot excess is real can sometimes be questioned, since it

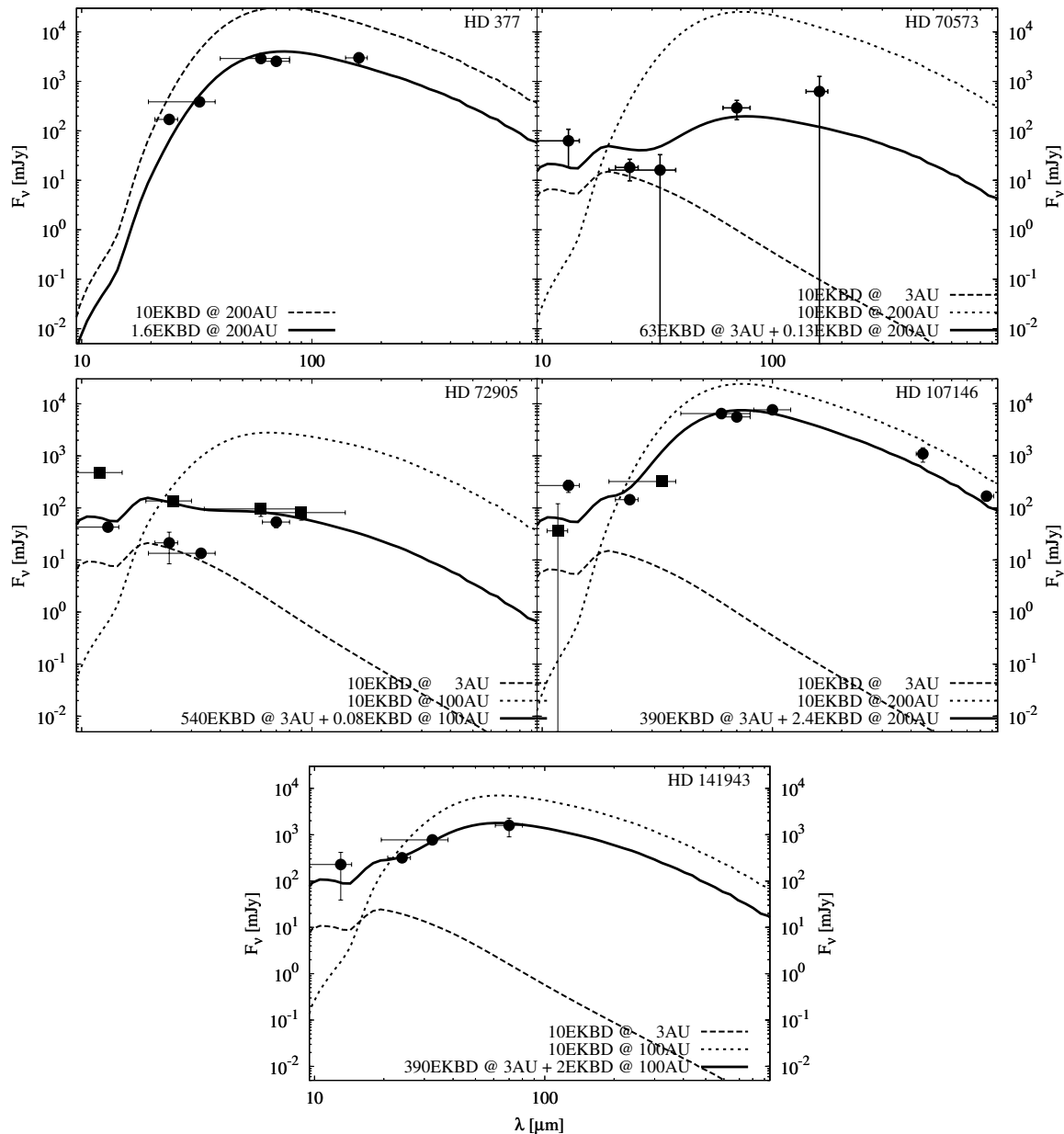


**Figure 5.11:** Observed (symbols) and modeled (lines) excess emission, scaled to the distance of 10 pc. The wavelength range matches the unshaded part of Fig. 5.10. Here, in contrast to Fig. 5.10, symbols represent the excess emission. Squares mark the cases where the scaled *NextGen* model shown on that figure was used to subtract the photosphere. Circles indicate that for these observations the stellar emission was subtracted using photospheric fluxes as given in the respective papers. Dashed lines: two “underlying” SEDs of reference disks (unscaled, i.e. with 10 EKBD), one for “cold” excess and one for “warm” excess (except for HD 377 where only a cold component is observed). Solid line: a linear combination of two scaled reference SEDs that provides a reasonable fit to the data points (except for HD 377 where a single scaled reference SED is sufficient).

can be mimicked by photospheric emission slightly larger than the assumed values. Indeed, the excesses for HD 70573 and HD 72905 at wavelengths around and below 25  $\mu\text{m}$  do not exceed 10%, which is comparable with the average calibration uncertainty and therefore has to be considered marginal (Bryden et al. 2006; Hillenbrand et al. 2008). Only in the case of HD 72905, the *Spitzer/IRS* detection of the 10  $\mu\text{m}$  emission from hot silicates provides an independent con-

**Table 5.5:** Disk properties derived in this study.

Star	Component	$M_{\text{disk}} [M_{\oplus}]$ <sup>1)</sup>	$R_{\text{belt}}$ <sup>2)</sup> [AU]	$M_{\text{dust}}$ <sup>3)</sup> [ $M_{\oplus}$ ]	$T_{\text{dust}}$ <sup>4)</sup> [K]
HD 377	Outer	(32) 32	200	$3.1 \times 10^{-2}$	40
HD 70573	Inner	(0.0063) 0.0046	3	$1.4 \times 10^{-7}$	200
	Outer	(2.6) 2.5	200	$2.0 \times 10^{-3}$	40
HD 72905	Inner	(0.054) 0.019	3	$3.4 \times 10^{-8}$	200
	Outer	(0.23) 0.23	100	$2.1 \times 10^{-4}$	50
HD 107146	Inner	(0.039) 0.023	3	$4.9 \times 10^{-7}$	200
	Outer	(47) 47	200	$4.8 \times 10^{-2}$	40
HD 141943	Inner	(0.039) 0.027	3	$8.0 \times 10^{-7}$	200
	Outer	(6.1) 6.1	100	$5.5 \times 10^{-3}$	50

Notes: <sup>1)</sup> Initial mass (in parentheses) and the current mass of the whole planetesimal disk (bodies up to 100 km in radius).

<sup>2)</sup> Location of the parent planetesimal belt.

<sup>3)</sup> Current mass of “visible” dust (grains up to 1 mm in radius).

<sup>4)</sup> Temperature of cross-section dominating astrosil grains at the location of the parent planetesimal belt, see explanation at Fig. 5.6.

firmation that the hot excess is real (Beichman et al. 2006a). However, the HD 72905 plot in Fig. 5.11 makes it obvious that some problems occurred in terms of the photosphere fitting. All data points that were obtained by subtracting the *IRAC* photospheric fluxes (squares) systematically lie above the data points where a photosphere from the literature was subtracted (circles). The origin of the difference is unclear; on any account, the problem cannot be mitigated by the assumption that an excess is already present at *IRAC* wavelengths, since this would shift the squares further upwards. Considering the circles to be more trustworthy, the shape of the SED to fit changes. Then a closer-in disk at  $\sim 0.3$  AU could better reproduce the fluxes in the near- and mid-IR, while the outer ring would have to be shifted to a distance somewhat larger than 100 AU in order not to surpass the measured flux at  $33 \mu\text{m}$ . A problem would arise with the inner disk: at  $\sim 0.3$  AU, the collisional evolution is so rapid that an unrealistically large initial belt mass would be necessary. Similar arguments have led Wyatt et al. (2007b) to the conclusion that HD 72905 must be a system at a transient phase rather than a system collisionally evolving in a steady state.

Still, treating the derived sizes and masses of the inner disks as upper limits yields physical implications. Because the collisional evolution close to the star is rapid, such belts must have lost up to two-thirds of their initial mass before they have reached their present age (cf. initial and current mass in Table 5.5). In the case of HD 70573, the known giant planet with  $a = 1.76$  AU and  $e = 0.4$  (Setiawan et al. 2007) does not seem to exclude the existence of a dynamically stable planetesimal belt either inside  $\sim 1$  AU or outside  $\sim 3$  AU.

### Results for Cold Dust

The estimated parameters of the outer components of the disks suggest “massive and large Kuiper belts”. The radii of the outer rings are larger than the radii derived in previous studies (cf. Table 5.4 and Table 5.5). This traces back to the usage of astrosil instead of blackbody when calculating the dust emission, so that the same dust temperatures are attained at larger distances (see Fig. 5.7).

Since one disk in the sample, that of HD 107146, has been resolved, it is natural to compare the derived disk radius with the one obtained from the images. Williams et al. (2004) report an outer border of the system of 150 AU based on submillimeter images. In contrast, Ardila et al. (2004) detected an 85 AU wide ring peaking in density at about 130 AU. This is comparable to,

although somewhat smaller than, the 200 AU radius found here. However, moving the outer ring to smaller distances would increase the fluxes in the mid-IR where the SED already surpasses the observations and the other way round in the sub-mm region. The resulting deficiency of sub-mm fluxes, though, could be due to roughness of Mie calculations. As pointed out by Stognienko et al. (1995), an assumption of homogeneous particles typically leads to underestimation of the amount of thermal radiation in the sub-mm region. Another explanation could be the choice of astrosil. Adopting for example ice or dirty ice would shift the location of the ring further inward, while the overall shape of the SED remains similar (Augereau et al. in prep.).

Large belt radii imply large masses. Dust masses derived here are by two orders of magnitude larger than previous estimates (cf. Table 5.5 and Table 5.4). The total masses of the belts derived with the new modeling approach range from several to several tens of earth masses, to be compared with  $\sim 0.1 M_{\oplus}$  in the present-day EKB (although there is no unanimity on that point — cf. Stern & Colwell 1997). Note that, as the collisional evolution at 100 – 200 AU is quite slow, whereas the oldest system in the sample is only 420 Myr old, the difference between the initial disk mass and the current disk mass is negligible. Assuming several times the minimum mass solar nebula with a standard surface density of solids  $\Sigma \sim 50 \text{ g cm}^{-2} (r/1\text{AU})^{-3/2}$  (e.g., Hayashi et al. 1985), the mass of solids in the EKB region would be a few tens  $M_{\oplus}$ ; and current models (e.g., Kenyon & Luu 1999b) successfully accumulate 100 km-sized EKB objects in tens of Myr. However, it is questionable whether the assumed radial surface density profile could extend much farther out from the star. As a result, it is difficult to say whether a progenitor disk could contain enough solids as far as at 200 AU from the star to form a belt of 30 – 50  $M_{\oplus}$ .

However, such questions may be somewhat premature. On the observational side, more data are needed, especially at longer wavelengths; for instance, the anticipated *Herschel* data (*PACS* at 100/160  $\mu\text{m}$  and *SPIRE* at 250 to 500  $\mu\text{m}$ ) would help a lot. On the modeling side, a more systematic study is needed to clarify, how strongly various assumptions of the current model (especially the collisional outcome prescription and the material choices) may affect the calculated size distributions of dust, the dust grain temperatures, and the amount of their thermal emission.

At this point, it can only be stated that in the five systems analyzed (with a possible exception of HD 72905) and with the caveat that available data are quite scarce, the observations are not incompatible with a standard steady-state scenario of collisional evolution and dust production. Of course, other possibilities, such as major collisional breakups (Kenyon & Bromley 2005; Grigorieva et al. 2007) or events similar to the Late Heavy Bombardment (as suggested, for instance, for HD 72905; Wyatt et al. 2007b) cannot be ruled out for the inner disks.

### 5.3 Application: Vega

(Results presented here are based on work that was carried out for “Müller et al. (2010)”. The author’s contribution to this study was confined to the actual modeling of the Vega disk. Additional analysis is included here for the sake of completeness. )

#### 5.3.1 The Vega System

##### Vega — An Agglomeration of Curiosities

For a long time, the A0 V main-sequence star Vega in a distance of 7.76 pc was considered a standard star and was used as a calibration source for photometric measurements. Ironically, this star proved the first object to unveil an IR excess over the expected stellar photosphere, indicative of debris dust (Aumann et al. 1984). Fluxes at wavelengths from mid-IR to millimeter have been measured with *IRAS* (Aumann et al. 1984; Walker & Wolstencroft 1988), *KAO* (Harper et al. 1984; Harvey et al. 1984), and *ISO* (Heinrichsen et al. 1998). As a result, its SED is known relatively well. The Vega disk has been resolved in sub-mm and mm with *JCMT* (Zuckerman & Becklin 1993; Holland et al. 1998), *OVRO* (Koerner et al. 2001), *IRAM* (Chini et al. 1990;

**Table 5.6:** Stellar parameters of Vega.

	Equator	Pole	Note
$R [R_{\odot}]$	$2.873 \pm 0.026$	$2.306 \pm 0.031$	1
$T_{\text{eff}} [\text{K}]$	$7900^{+500}_{-400}$	$10150 \pm 100$	2
$L_* [L_{\odot}]$	$28^{+8}_{-6}$	$57 \pm 3$	3
$\log(g[\text{cms}^{-2}])$	$4.074 \pm 0.012$	$3.589 \pm 0.056$	1
$M_* [M_{\odot}]$	$2.3 \pm 0.2$		2
Age [Myr]	350		

Notes: (1) From Peterson et al. (2006), (2) From Aufdenberg et al. (2006), (3) Luminosity at the equator and at the poles derived from the equatorial and polar values of the stellar radius  $R$  and effective temperature  $T_{\text{eff}}$  and from the average stellar luminosity of  $37 \pm 3 L_{\odot}$  (Aufdenberg et al. 2006) through the Stefan-Boltzmann relation.

Wilner et al. 2002), and *CSO* (Marsh et al. 2006). These observations reveal a clumpy ring of large dust grains between about 80 and 120 AU, suggesting a Kuiper belt analog. Wyatt (2003) and Reche et al. (2008) naturally explain the ring-like structure with a resonant trapping of dust parent bodies by a presumed Neptune- to Saturn-mass planet during their outward migration in the past.

Su et al. (2005) resolved the Vega system by *Spitzer/MIPS* at 24, 70, and 160  $\mu\text{m}$ . They found a featureless, huge disk extending up to  $\sim 800$  AU. Although it came as a surprise at the time when this discovery was made, it is no longer astonishing now. As noted in Chapter 1.2.3, this is exactly what is expected: a Kuiper belt-sized, clumpy ring of large dust grains seen in the sub-mm and a much more extended disk of small grains, producing a smooth brightness distribution evident in the mid- to far-IR. However, by fitting these data with power-law dust distributions, Su et al. (2005) deduced a mysterious overabundance of blowout grains of  $\sim 1 \mu\text{m}$  in radius. Under the assumption of a steady-state collisional disk evolution over the Vega age, this would imply that the disk must have lost  $\sim 3$  Jupiter masses of material, which appears unlikely. Accordingly, Su et al. suggested a recent major collisional event as a possible explanation. More exotic alternative scenarios were proposed to explain such a large fraction of blowout grains including a close stellar encounter (Makarov et al. 2005) and a dynamical instability event similar to what caused the Late Heavy Bombardment in the solar system (Wyatt et al. 2007b). However, Kenyon & Bromley (2008), who modeled the Vega debris disk as a result of icy planet formation with their hybrid multi-annulus coagulation code, found their model to be capable of reproducing the *Spitzer* fluxes, questioning the need of alternative scenarios.

However, the excessive amount of grains in blowout orbits inferred by Su et al. (2005) uncovers another problem. A steady-state collisional evolution implies a certain size distribution of dust. Typically, the amount of blowout grains instantaneously present in the steady-state system is much less than the amount of slightly larger grains in loosely bound orbits around the star. This is because the dust production of the grains of adjacent sizes is comparable, but the lifetime of bound grains (due to collisions) is much longer than the lifetime of blowout grains (disk-crossing timescale). Thus the amount of blowout grains reported by Su et al. (2005) would necessitate an unrealistic huge amount of larger grains in bound orbits. And this conclusion would not only be valid in a steady-state scenario, but also all alternative scenarios listed above would face the same problem.

Beside the outer disk, the inner part of the system reveals another peculiarity. Pioneering interferometry observations with *CHARA/FLUOR* in the near-IR (Absil et al. 2006) have led to the discovery of a dust cloud just exterior of the sublimation zone, well inside 1 AU (“exozodi”).

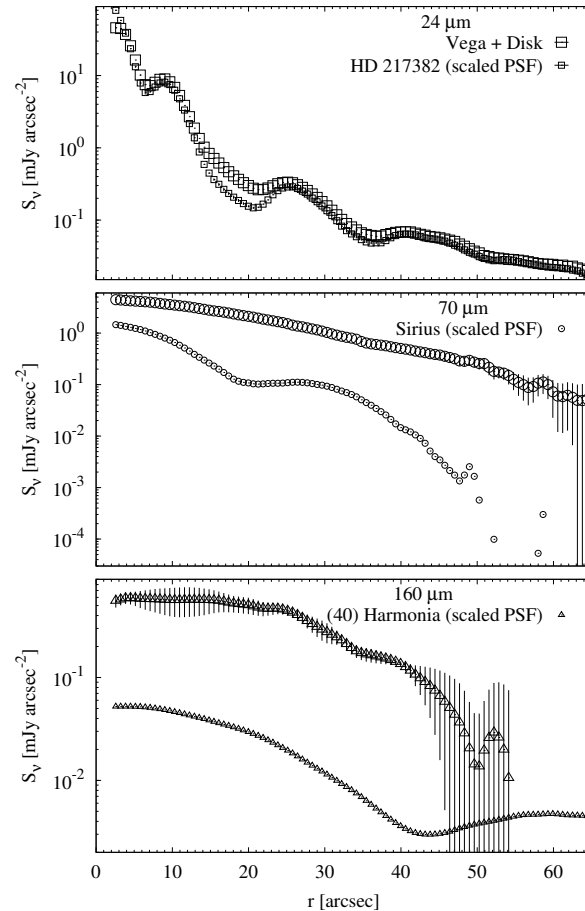


**Figure 5.12:** Radial profiles of the surface brightness for Vega as extracted from the *Spitzer MIPS* images for 24 (large squares), 70 (large circles), and 160  $\mu\text{m}$  (large triangles) from top to bottom. The standard sources HD 217382, Sirius, and (40) Harmonia used for PSF subtraction for the different wavelengths are shown as small symbols of the same shapes.

Just like the dust in the system, the central star turned out to be unusual, too. Peterson et al. (2006) and Aufdenberg et al. (2006) found Vega to be a rapid rotator, which makes stellar parameters functions of the stellar latitude. Table 5.6 summarizes the stellar parameters relevant for this study. It remains unclear whether unusual properties of the disk are somehow related to those of the star or not.

In this chapter the question is re-addressed whether the available data are compatible with a steady-state collisional scenario of dust production and evolution. Instead of simply seeking dust distributions — e.g., in the form of power-laws — that would provide the best fit to the observables, the new, collisional modeling approach is employed.

### *Spitzer/MIPS* Images

The *MIPS* images of the Vega system at 24, 70, and 160  $\mu\text{m}$  were extracted from the *Spitzer* archive, using the *Leopard* software<sup>2</sup>. A detailed description of subsequent data reduction is given in Müller et al. (2010, section 2). Fig. 5.12 shows the final radial surface brightness profiles before PSF subtraction together with the corresponding PSFs. The resulting photometric points are listed in Tab. 5.7 together with the set of photometric data from the literature.

At this point it should only be mentioned that reducing the 24  $\mu\text{m}$  profile causes special difficulties arising from saturation in the inner 4'' (30 AU) of the image. The resulting photometric

<sup>2</sup><http://ssc.spitzer.caltech.edu/mips/>

**Table 5.7:** Photometric data of Vega.

$\lambda$ [ $\mu\text{m}$ ]	$F_{disk}$ [mJy]	Instr.	Ref.
24.0	$(7.846 \pm 0.280) \times 10^3$	<i>Spitzer</i>	Müller et al. (2010)
25.0	$(2.979 \pm 0.936) \times 10^3$	<i>IRAS</i>	Walker & Wolstencroft (1988)
25.0	$(4.019 \pm 2.080) \times 10^3$	<i>ISO</i>	Heinrichsen et al. (1998)
47.0	$(6.414 \pm 1.640) \times 10^3$	<i>KAO</i>	Harvey et al. (1984)
60.0	$(7.918 \pm 0.901) \times 10^3$	<i>IRAS</i>	Walker & Wolstencroft (1988)
60.0	$(9.318 \pm 2.082) \times 10^3$	<i>ISO</i>	Heinrichsen et al. (1998)
70.0	$(9.399 \pm 1.200) \times 10^3$	<i>Spitzer</i>	Müller et al. (2010)
80.0	$(9.091 \pm 2.910) \times 10^3$	<i>ISO</i>	Heinrichsen et al. (1998)
95.0	$(6.829 \pm 1.825) \times 10^3$	<i>KAO</i>	Harvey et al. (1984)
100.0	$(7.109 \pm 0.754) \times 10^3$	<i>IRAS</i>	Walker & Wolstencroft (1988)
100.0	$(5.969 \pm 1.920) \times 10^3$	<i>ISO</i>	Heinrichsen et al. (1998)
120.0	$(4.890 \pm 1.551) \times 10^3$	<i>ISO</i>	Heinrichsen et al. (1998)
160.0	$(2.059 \pm 0.800) \times 10^3$	<i>Spitzer</i>	Müller et al. (2010)
170.0	$(2.437 \pm 0.771) \times 10^3$	<i>ISO</i>	Heinrichsen et al. (1998)
193.0	$(8.932 \pm 5.000) \times 10^2$	<i>KAO</i>	Harper et al. (1984)
200.0	$(1.321 \pm 0.408) \times 10^3$	<i>ISO</i>	Heinrichsen et al. (1998)
350.0	$(4.691 \pm 1.500) \times 10^2$	<i>CSO</i>	Marsh et al. (2006)
450.0	$(1.301 \pm 0.450) \times 10^2$	<i>CSO</i>	Marsh et al. (2006)
800.0	$(1.626 \pm 0.500) \times 10^1$	<i>IRAM</i>	Chini et al. (1990)
800.0	$(2.426 \pm 1.500) \times 10^1$	<i>JCMT</i>	Zuckerman & Becklin (1993)
850.0	$(4.086 \pm 0.540) \times 10^1$	<i>JCMT</i>	Holland et al. (1998)
870.0	$(1.721 \pm 0.900) \times 10^1$	<i>IRAM</i>	Chini et al. (1990)
1300.0	$(2.390 \pm 1.500) \times 10^0$	<i>IRAM</i>	Chini et al. (1990)
1300.0	$(1.189 \pm 0.190) \times 10^1$	<i>OVRO</i>	Koerner et al. (2001)
1300.0	$(1.140 \pm 0.170) \times 10^1$	<i>IRAM</i>	Wilner et al. (2002)

excess, obtained by integrating the subtracted profile (the Vega profile minus the scaled PSF) from  $4''$  outward, is  $0.94 \pm 0.28$  Jy. Here the formal error is determined by the standard deviations of Vega and the PSF plus an assumed systematic error of 5% in the photometry of Vega’s photosphere. However, the flux is probably even more uncertain because of the ambiguous contribution of the inner part of the disk, between  $4''$  and  $10''$  (30 – 80 AU). Thus, for a more accurate comparison with the models below, the “certain” part of the observed flux can be used by integrating the brightness profile from  $10''$  outward. This nearly halves the total  $24 \mu\text{m}$  flux, giving 0.53 Jy. This “partial” flux will later be compared with the flux predicted by the models exactly in the same range of distances, from  $10''$  (80 AU) outward. Coincidentally, it is this range where the emitting dust is only present in most of the models, because the inner edge of the birth ring is located at 80 AU. It is to stress, however, that the true total  $24 \mu\text{m}$  excess flux may be higher. It probably lies in the range 0.5 – 0.9 Jy, with no obvious possibility to narrow it because of the saturation problem described above.

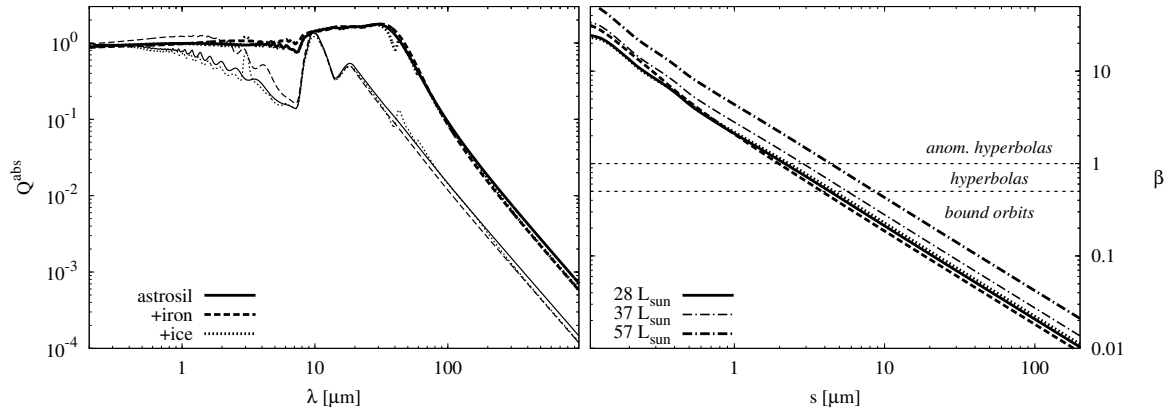


**Figure 5.13:** Left: Absorption efficiency for 1 (thin lines) and 4.9  $\mu\text{m}$  (thick lines) particles consisting of astronomical silicate (solid lines) and of an astrosil matrix with 10% iron (dashed lines) and water ice (dotted lines) inclusions. Right: The  $\beta$  ratio of the same grains as in the left panel (the same line-styles), assuming  $L_* = 28 L_\odot$ . Additionally, thin and thick dash-dotted lines show the  $\beta$  ratio for pure astrosil grains, but higher stellar luminosities of  $L_* = 37 L_\odot$  and  $57 L_\odot$  respectively.

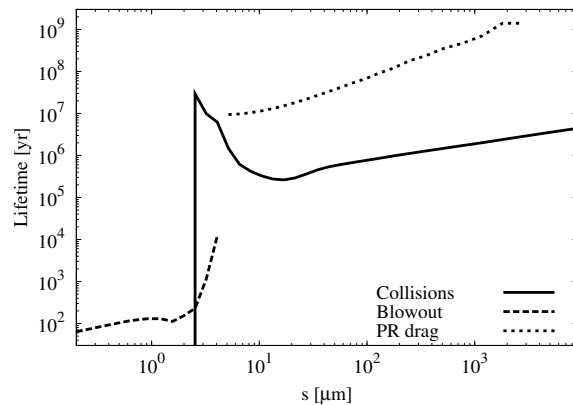


**Figure 5.14:** Timescales as functions of the grain size: collisional time (solid line), blowout time (long-dashed), and PR time (short-dashed). The collisional time is an average over the grain orbits with all possible pericentric distances  $q$  and eccentricities  $e$ , weighted with the amounts of those particles in the disk. The PR time is the time it takes for a grain to drift across the parent ring or, more exactly, the time interval over which a grain’s  $q$  reduces from 120 AU to 80 AU. It was computed by simultaneously solving the orbit-averaged equations that describe  $q(t)$  and  $e(t)$  (Burns et al. 1979). All timescales are for the parameters of the reference model.

### 5.3.2 The Reference Model

#### Choice of Model Parameters

In the reference model, a stellar luminosity at the equator of  $L_* = 28 L_\odot$  (Table 5.6) is used, and it is assumed that the collisional cascade has been operating over the entire stellar age, 350 Myr.

According to Dent et al. (2000), Su et al. (2005), Marsh et al. (2006) and Wyatt (2006) — as a “first guess” — an initial ring of parent bodies with semi-major axes ranging from 80 – 120 AU with an initially constant surface density in this range is adopted. The clumpy shape of the sub-mm ring, usually interpreted through resonant capture of planetesimals by an unseen planet interior to the ring, implies that the eccentricities of the planetesimals are not very low (Wyatt 2003; Reche et al. 2008). Further, the smooth drop of surface brightness in the far-IR images is indicative of not too low eccentricities (Thébaud & Wu 2008). On the other hand, the relatively narrow ring observed at wavelengths longer than 350  $\mu\text{m}$  indicates that eccentricities cannot be



too high. As a reasonable compromise and for the sake of simplicity, for the reference model a uniform distribution of eccentricities from 0.0 to a moderate value of 0.2 is adopted. Maximum orbital inclinations (or a semi-opening angle) are then set to 0.1 rad in accord with the energy equipartition assumption. Thus, the initial planetesimal disk resides between 64 and 144 AU from the star. This is still in agreement with the observed 80 – 120 AU as most of the material is concentrated in the central part of the initial ring. Note that these assumptions describe the initial disk extension. The subsequent collisional and dynamical evolution of the parent belt slightly changes the distributions of planetesimals.

All particles are assumed to be composed of astrosil. Mie theory is used to calculate radiation pressure and absorption efficiencies (Fig. 5.13).

The disk is modeled with ACE with grains ranging from 0.05  $\mu\text{m}$  – 67 km in radius and the mass ratio in the adjacent bins of 4. The pericenter distance grid covered 50 logarithmically spaced values from 20 – 800 AU. The eccentricity grid contained 100 linearly-spaced values between  $-5.0$  and  $5.0$  (eccentricities are negative in the case of smallest grains with  $\beta > 1$ , whose orbits are anomalous hyperbolas). The distance grid used by ACE to output distance-dependent quantities such as the size distribution is 10 AU through 600 AU at 10 AU increments. In the collisional prescription,  $Q_{D,s} = Q_{D,g} = 5 \times 10^6 \text{ erg g}^{-1}$ ,  $3b_g = 1.38$ , and  $3b_s = 0.37$  and the size distribution of fragments to be a power-law with index  $\eta = 1.833$  is set. Both disruptive and cratering collisions are switched on.

As shown in Fig. 5.14, typical timescales for PR drag in the Vega disk are much longer than collisional lifetimes, except for a very narrow size range close to the blowout limit, where both become comparable. Thus the PR effect is switched off in the ACE runs, but additional checks are made in Chapter 5.3.4. Gas drag can safely be neglected, because the Vega system with its 350 Myr age could not have retained any primordial gas, while the density of secondary gas cannot be high enough to influence the dust dynamics. As long as the drag forces are discarded, the number of parameters to vary, and thus the number of required ACE runs, can be reduced by applying scaling laws (see Chapter 3).

A set of model parameters used for the reference model is given in the first line of Tab. 5.8. The table only lists those parameters that later are varied with respect to the reference model.

### Size, Radial, and Temperature Distributions

Dust distributions in the reference model are presented in Fig. 5.15. The right panel shows the grain size distributions within and outside the birth ring. The radiation pressure blowout effect causes a steep drop between 3 and 5  $\mu\text{m}$ , which corresponds to  $\beta \approx 0.5$  (Fig. 5.13, right). As previous studies have shown, the blowout drop in the size distribution results in a more or less pronounced wavy pattern in the distribution of larger particles (e.g., Thébaud et al. 2003; Krivov et al. 2006), with the “wavelength” and amplitude of the pattern depending on material strength and impact velocities. However, compared to previous studies (e.g., see Chapter 5.2 or Krivov et al. 2006), the semi-major axis is replaced by a grid of pericentric distances as phase variables in the ACE simulations. This reduces the effects of discretization on the effective relative velocities, which is strongest for particles on highly eccentric orbits with pericenters close to the birth ring. Therefore, the waviness is washed out, especially in the reference run.

The radial distribution of different-sized grains is shown in the bottom panel of Fig. 5.15 with thin lines. As seen in Chapter 5.2.3, most of the material is located between 80 and 120 AU<sup>3</sup>. The largest particles are confined to this region as they are nearly unaffected by radiation pressure.

<sup>3</sup>Note that the ring starts at about 73 AU and not at the above-mentioned 64 AU. This is due to the eccentricity binning. Individual bins are 0.1 wide and centered at 0.05, 0.15, and so on. Thus, the largest effective eccentricity for  $e_{\text{max}} = 0.2$  is  $e = 0.15$ . The corresponding minimum pericentric distance for  $a = 80 \text{ AU}$  is  $q_{\text{min}} = 0.85 \times 80 \text{ AU} = 68 \text{ AU}$ . The next larger point in the pericenter grid is then centered at 73 AU.

**Table 5.8:** Sets of model parameters used in the simulations. The parameters of the reference model are listed in the first line. For all other models, only parameters that are different from those of the reference model are given.

Model	$L_* [L_\odot]$	$T$ [Myr]	$a_{\text{inner}}$ [AU]	$a_{\text{outer}}$ [AU]	$e_{\text{max}}$	$i_{\text{max}}$	composition	collisions	$Q_{D,s}$ [erg g $^{-1}$ ]	$3b_s$	$\eta$
ref.	28	350	80	120	0.2	0.1	no incl.	w/ cratering	$5.0 \times 10^6$	0.37	1.833
a1	—	35	—	—	—	—	—	—	—	—	—
a2	—	3.5	—	—	—	—	—	—	—	—	—
b1	—	—	50	—	—	—	—	—	—	—	—
b2	—	—	100	—	—	—	—	—	—	—	—
b3	—	—	—	100	—	—	—	—	—	—	—
b4	—	—	—	150	—	—	—	—	—	—	—
c1	37	—	—	—	—	—	—	—	—	—	—
c2	57	—	—	—	—	—	—	—	—	—	—
c3	—	—	—	—	—	—	ice incl.	—	—	—	—
c4	—	—	—	—	—	—	iron incl.	—	—	—	—
d1	—	—	71.1	130.9	0.1	0.05	—	—	—	—	—
d2	—	—	91.4	100.8	0.3	0.15	—	—	—	—	—
e1	—	—	—	—	—	—	—	w/o cratering	—	—	—
e2	—	—	—	—	—	—	—	—	$2.5 \times 10^6$	0.2	—
e3	—	—	—	—	—	—	—	—	$6.9 \times 10^6$	0.45	—
f1	—	—	—	—	—	—	—	—	—	—	1.6
f2	—	—	—	—	—	—	—	—	—	—	1.95
best fit	45	—	62	120	0.1	0.05	—	—	—	—	1.95

The smaller the particles, the wider they are spread over the disk. In addition, the bottom panel of Fig. 5.15 plots the total normal geometrical optical depth  $\tau$  (in arbitrary scale). The optical depth beyond  $\sim 120$  AU is dominated by particles just above the blowout size,  $\sim 5 \mu\text{m}$ , which are in barely bound orbits. It is only in the region of the birth ring where particles with  $s \gtrsim 10 \mu\text{m}$  make a significant contribution to the optical depth.

To judge about the dust temperatures and the thermal emission of the disk in the reference model, the left top panel of Fig. 5.15 depicts the dust temperature as a function of stellar distance and grain size. Both distance and size axes share those of the two other panels (note that the size axis is reversed compared to Fig. 5.6 to facilitate comparison with upcoming figures). Grains with  $s \sim 5 - 10 \mu\text{m}$  at  $r \sim 80 - 120$  AU are dominating the reference disk, leading to a typical temperature of about 60 K.

### Dust and Disk Masses

Then SEDUCE is used to obtain the SED of the reference disk and to fit it vertically to the available observations starting at  $25 \mu\text{m}$ . Shorter wavelengths are neglected in the fitting process as the uncertainty of the photospheric subtraction there is too high. Furthermore, the *Spitzer*  $24 \mu\text{m}$  data point is not used for fitting because of the uncertainties in converting the image into photometry as described above. In the SED calculation, the stellar parameters at the equator are adopted to obtain the photosphere seen by the dust disk, whereas the polar values are considered to calculate the observed photosphere (Tab. 5.6).

The dust, disk, and initial disk masses in the reference model are given in the first line of Tab. 5.9. The dust mass of  $7 \times 10^{-3} M_\oplus$  is by about a factor of two higher than what was derived by Su et al. (2006). The actual agreement is even better, because the upper cutoff size of  $1000 \mu\text{m}$  used here is larger than that of Su et al.. The total mass of the reference disk is about  $16 M_\oplus$ , which is 85% of its initial mass 350 Myr ago when the collisional cascade started to operate.

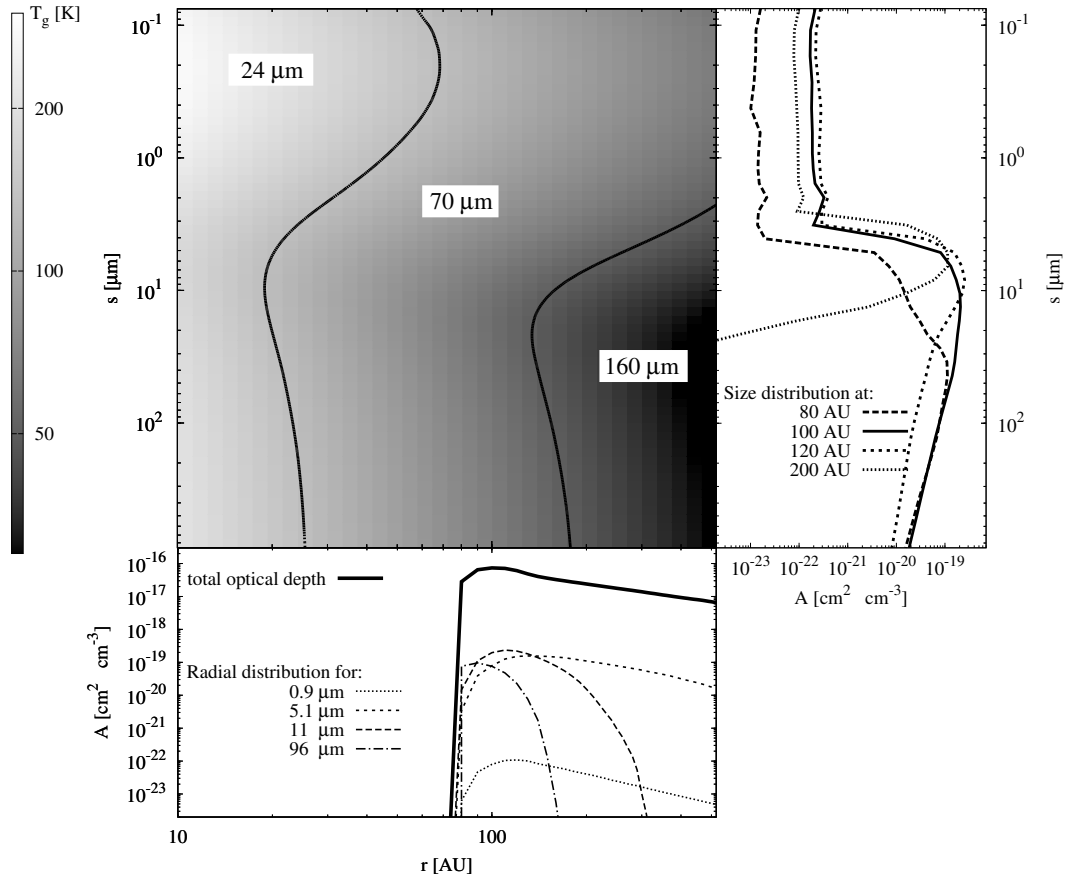


**Figure 5.15:** Left top: Disk’s temperature profile for the assumed astrosilicate grains and stellar parameters as derived for Vega’s equator. Two solid lines separate the regions of dominant emission at the three *Spitzer/MIPS* wavelengths: in the left part 24  $\mu\text{m}$  emission is more efficient than emission at the other two wavelengths, in the central part 70  $\mu\text{m}$  emission dominates, and in the right part 160  $\mu\text{m}$  emission is the strongest. Left bottom: Radial distribution in the reference model for 0.9, 5.1, 11 and 96  $\mu\text{m}$  grains (thin lines) and the resulting total optical depth in arbitrary units (thick solid line). Right: Grain size distribution in the reference disk at 80, 100, 120, and 200 AU.

### Spectral Energy Distribution

For an easier comparison between the modeled SEDs and the photometric observations in the different spectral regions, throughout this chapter the excess ratio will be used. The latter is defined as the ratio of the dust emission to the stellar photospheric emission or equivalently, as the ratio of the total flux (star + dust) to the stellar flux minus unity. The SED of the reference disk in terms of the excess ratio is presented in Fig. 5.16 (left bottom) with a solid line. Given that the reference model is a first-guess one, the agreement with the observations is already quite satisfactory.

At 24  $\mu\text{m}$  the model yields 0.43 Jy, which is at  $2\sigma$  under the *Spitzer* point of 0.94 Jy. As explained in Chapter 5.3.1, the total observed flux from 4'' outward is unsure, because of an uncertain part between 4'' and 10''. If only the observed flux from 10'' outward is considered, it reduces to 0.53 Jy. At the same time, the flux from 10'' outward in the reference model can be calculated. The result is 0.40 Jy, which is only slightly below the observed one. That value of 0.40 Jy differs insignificantly from the calculated flux from 4'' outward, 0.43 Jy, because the emitting dust in the reference model is entirely located outside 10'', and it is only the finite PSF’s width that “transfers” 0.03 Jy of the emission closer in.

As far as the *IRAS* 25  $\mu\text{m}$  flux is concerned, it is known to be quite uncertain. This is due

**Table 5.9:** Derived dust masses, disk masses, and initial disk masses for all models

runs	$M_{\text{dust}} [10^{-3}M_{\oplus}]$	$M_{\text{disk}} [M_{\oplus}]$	$M_{\text{ini}} [M_{\oplus}]$
ref.	6.63	16.3	18.9
a1	5.62	4.21	4.35
a2	3.67	3.05	3.06
b1	5.41	19.3	22.7
b2	7.34	14.1	16.2
b3	6.22	17.1	20.7
b4	7.38	14.2	15.7
c1	6.96	14.8	17.1
c2	6.59	11.9	13.6
c3	7.08	18.5	21.5
c4	7.28	16.5	19.1
d1	10.9	41.5	47.5
d2	4.74	10.5	12.6
e1	4.37	3.60	3.81
e2	8.64	51.0	62.7
e3	4.77	5.15	5.70
f1	7.09	9.31	10.5
f2	5.92	32.2	39.4
fit	5.09	46.7	55.5

to the large field of view. Anyway, this data point is inconsistent with the newer *Spitzer* 24  $\mu\text{m}$  measurement.

In the far-IR, the model emission matches the *Spitzer* fluxes perfectly and lies within the error bars of the other observations. At (sub-)millimeter wavelengths, the measurements themselves are contradictory, lying sometimes at more than  $2\sigma$  from each other, and it is difficult to judge which of them are most accurate. The model SED provides a compromise, lying in the middle of the entire set of data points.

### Radial Surface Brightness Profiles

Using SUBITO, the radial surface brightness profiles of the disk model are calculated and then convolved with the corresponding PSFs. The final profiles are presented as solid lines in the right panel of Fig. 5.16. The model profiles are not inconsistent with the *Spitzer* observations. Especially the 70  $\mu\text{m}$  profile is very close to what was measured. However, both 24 and 160  $\mu\text{m}$  curves are slightly too flat. The 160  $\mu\text{m}$  profile lies under the measurements in the inner part of the disk and above them in the outer part, explaining why the total 160  $\mu\text{m}$  flux is about right (see the bottom left panel). In contrast, most of the 24  $\mu\text{m}$  flux comes from the inner part of the disk inside 100 AU. In this region the model profile goes below the data points, so that the higher emission in the outer part of the disk cannot compensate this deficiency.

Altogether, the surface brightness profiles are more constraining for the disk model than the SED. Already the “first-guess” model satisfactorily reproduces the observed SED, but the brightness profiles reveal moderate deviations from those deduced from the observations.

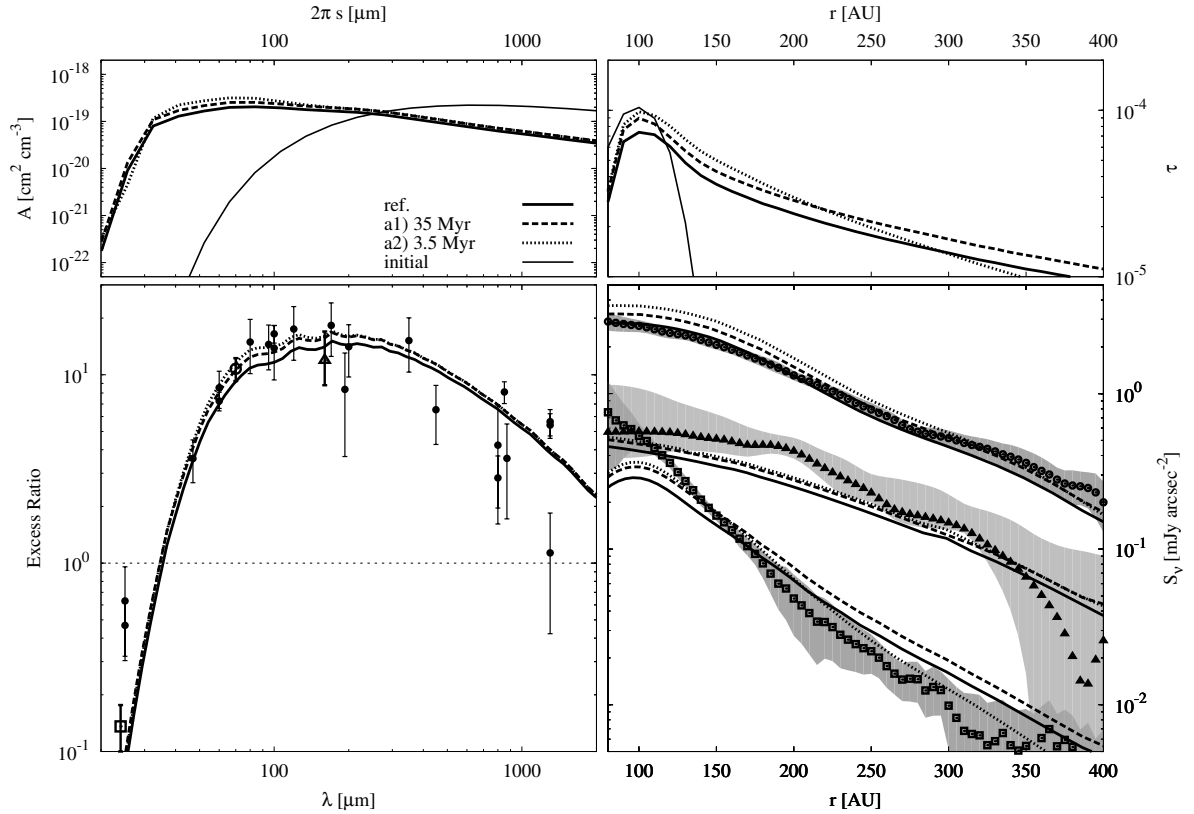


**Figure 5.16:** Top left: Grain size dust distributions of the reference model (thick solid line) and of the same model but at earlier times of 3.5 (dotted line) and 35 Myr (dashed line), all in the center of the initial planetesimal ring. The initial distribution for the simulation is plotted as thin solid line. Note the usage of  $2\pi s$  instead of  $s$  in this and subsequent size distribution plots. Since particles with the size parameter  $2\pi s/\lambda \sim 1$  emit most efficiently,  $2\pi s$  roughly gives the typical wavelength of the emission. This alleviates comparison between the size distribution and the SED (bottom left). Top right: Radial profile of the optical depth for the same disk models. Bottom left: Corresponding SEDs. Symbols with error bars are data points (large square, large circle, and large triangle mark  $24 \mu\text{m}$ ,  $70 \mu\text{m}$ , and  $160 \mu\text{m}$  excess ratios deduced from *Spitzer/MIPS* images). Bottom right: Modeled (lines) and observed (symbols) surface brightness profiles at  $24$ ,  $70$ , and  $160 \mu\text{m}$ . The shapes of symbols are the same as in the bottom left panel and in Fig. 5.12. The shaded areas around the data points indicate the errors.

### 5.3.3 Variation of Model Parameters

In this section the response of observables (SED, brightness profiles) to changes in physical parameters (those of the star, planetesimal belts, and dust, as well as the collisional prescription) is investigated. A specific goal is to check if the agreement of the modeled brightness profiles of the Vega disk with observations can be improved, preserving the agreement in the SED that was achieved in the reference model. Accordingly, a set of models is considered, the parameters of which are listed in Tab. 5.8. Most of these models differ from the reference model by one parameter. Several parameters at a time are only modified if these are physically related and this is required for consistency.

For each of the models, results are presented in the same way as for the reference one. The size distribution, optical depth profile, the SED, and the radial brightness profiles are combined into a single figure (Figs. 5.17 to 5.24), each having the same structure as Fig. 5.16. In all the figures, the reference model is over-plotted with a solid line. The resulting final dust masses, final disk masses, and initial disk masses are given in Tab. 5.9.

In the following subsections, the variations of the reference model are explained and discussed.

They are structured according to the underlying physical and astrophysical mechanisms at work.

### Delayed Stirring

Before a debris disk starts to evolve in a steady-state regime, a collisional cascade has to ignite and operate for sufficient time. Initiation of the cascade requires a mechanism to stir the disk (Wyatt 2008). This can be self-stirring by largest planetesimals (Kenyon & Bromley 2004a) or stirring by planets orbiting in the inner gap of the disk (Wyatt 2005a; Mustill & Wyatt 2009). External events such as stellar flybys can also stir the disk sufficiently. It may have been the case for Vega  $\sim 5$  Myr ago (Makarov et al. 2005). Furthermore, after the onset of the cascade, the system needs enough time to reach a steady-state collisional regime at dust sizes (e.g., Löhne et al. 2008). Thus the duration of a steady-state disk evolution is generally shorter than the system's age. It is unclear which particular mechanism may have triggered the cascade in the Vega disk and how long it is already at work. It may have started either shortly after the primordial gas dispersal or much later in the Vega history.

To investigate the effect of the unknown “collisional age” of the Vega disk, the reference disk model is simply used to calculate the SEDs and surface brightness profiles at earlier time steps. Fig. 5.16 shows the results at 3.5, 35 and 350 Myr. At earlier times, the maximum of the size distribution is slightly more pronounced (top left). This results in a moderate enhancement of thermal emission between 50 and 500  $\mu\text{m}$ , which is still in agreement with the observations (bottom left). The optical depth profile (top right) shows that 3.5 Myr of collisional evolution is not sufficient to bring enough particles on highly eccentric orbits, so that the profile is steeper than in the reference model. The 24 and 70  $\mu\text{m}$  profiles steepen (bottom right), the latter being no longer compatible with observations. At 35 Myr, the optical depth profile is only shifted vertically compared to the reference model, which indicates that the spatial distribution has already reached an equilibrium (top right). The final and initial disk masses (Tab. 5.9) are close to each other, which is natural as younger disks have spent less material in collisions. Besides, the estimated total masses of younger disks are smaller than in the reference model. The reason is that younger disks that are not in a steady-state regime yet are “dustier” than older disks of the same total mass (Krivov et al. 2006).

An overall conclusion is that at least several tens of Myr of collisional evolution seem to be required to make observables consistent with observations.

### Disk Location

The choice of the initial disk extension in the reference model comes from resolved images in the sub-mm and radio. However, a low resolution of these observations still leaves room for reasonable modifications. Hence, the initial semi-major axis range of planetesimals is varied, intentionally pushing them to the limits posed by the images, in order to see the effects more clearly.

First, it is focused on the inner disk edge. By placing additional material closer in, an increase of warm emission is expected which prevents the brightness profile from dropping off towards the star too early. Thus, a shift of the inner edge inward down to 50 AU is tried. For completeness, also the case with the inner edge at 100 AU is added. The results are presented in Fig. 5.17.

As expected, taking  $a_{\text{inner}} = 50$  AU slightly shifts the SED to shorter wavelengths and strongly depresses the sub-mm emission. Taking  $a_{\text{inner}} = 100$  AU yields the opposite, although the effect is weaker. This traces back to the under- or overabundance of larger grains, hundreds of micrometers in size (top left). The reason for that, in turn, is the existence of two distinct dynamical regimes for bound dust grains. Large grains with no or little response to the stellar radiation pressure essentially inherit their orbital eccentricities from the parent bodies. For small, barely bound grains, radiation pressure is the dominant effect, pushing them to wide, highly eccentric

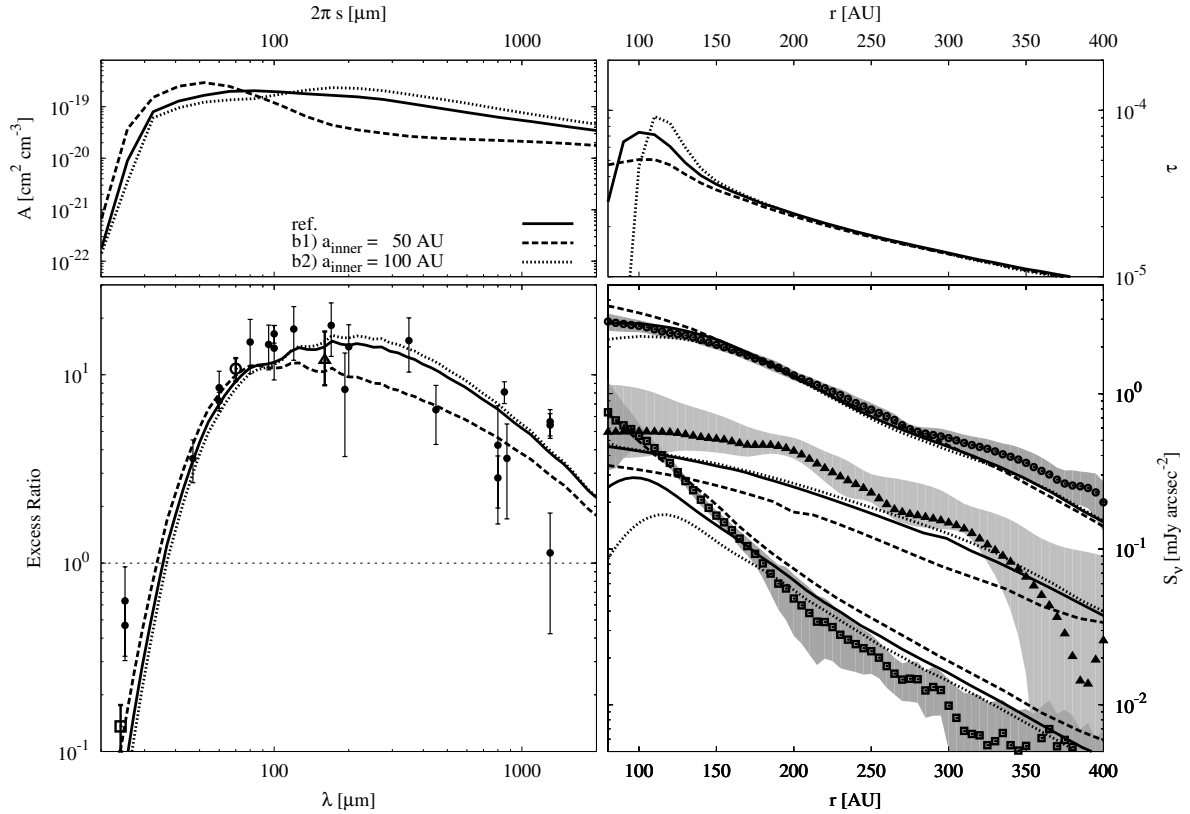


**Figure 5.17:** Same as Fig. 5.16, but with the inner edge of the disk shifted inward (dashed lines) and outward (dotted).

orbits. Shifting the disk further in increases the average collisional velocities, and lowers the collisional lifetime of larger grains — but not of smaller ones. As a result, the relative abundance of larger grains is reduced.

In terms of the surface brightness profiles, it is mostly the  $24 \mu\text{m}$  profile that is affected. It rises significantly inside 200 AU, reproducing perfectly the observations. However, in the outer part of the disk it becomes flatter so that the emission here is overestimated. The  $70 \mu\text{m}$  profile remains almost unaffected, except for the inner part within 150 AU, which responds to  $a_{\text{inner}}$  in the same manner the  $24 \mu\text{m}$  does, albeit less strongly. Finally, the  $160 \mu\text{m}$  profile preserves its slope, but shifts downwards ( $a_{\text{inner}} = 50$  AU) or slightly upwards ( $a_{\text{inner}} = 100$  AU).

Second, similar to the inner edge, an inward shift of the outer edge would lower the amount of cold dust, enhancing the warm emission. So  $a_{\text{outer}}$  was changed to 100 and 150 AU to find similar modifications in the dust distribution and thermal emission as above (Fig. 5.18). Decreasing  $a_{\text{outer}}$  makes the ring narrower and shifts the bulk of the material closer in. The maximum in the size distribution becomes more pronounced and shifts to smaller grains. The entire SED slightly shifts towards shorter wavelengths. The peak of the optical depth profile becomes stronger and moves closer to the star. This directly translates to the radial surface brightness profiles, especially at  $24 \mu\text{m}$ , which becomes appreciably steeper. Increasing  $a_{\text{outer}}$  naturally has opposite effects.

On the whole, it seems that shifting the inner edge of the belt inward has a clear potential of getting a  $24 \mu\text{m}$  profile that would better match the observed one. However, the shift from 80 AU down to 50 AU that was tested here may be too strong, because it may contradict the sub-mm images.

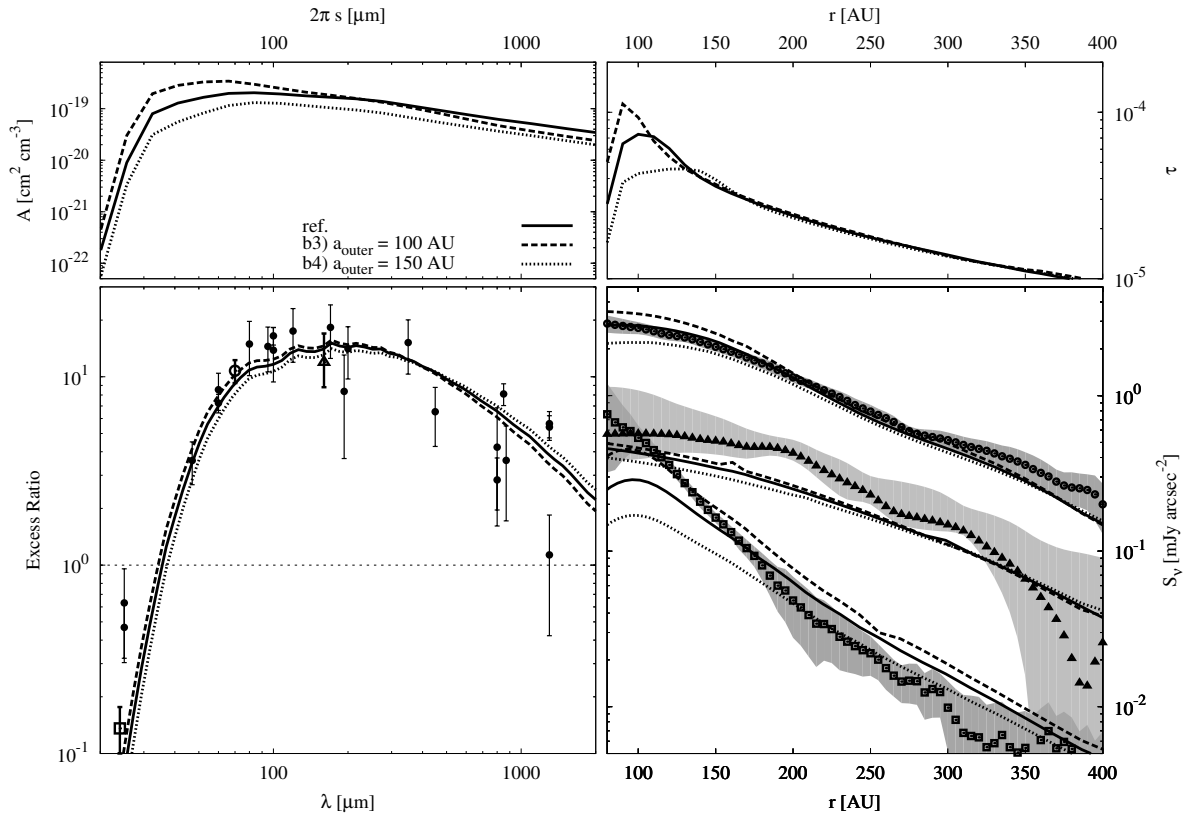


**Figure 5.18:** Same as Fig. 5.16, but with the outer edge of the disk shifted inward (dashed lines) and outward (dotted).

### Dynamical Excitation

Now the dynamical excitation of the disk is considered. It is parameterized by the maximum orbital eccentricities  $e_{\text{max}}$  that planetesimals had at the onset of the collisional cascade. This value does not change considerably in the course of the subsequent evolution (under the assumptions of the model, e.g., without planets), and it is approximately the same for disk solids of all sizes except for the smallest dust particles that are vulnerable to radiation pressure. From the dynamical point of view, higher eccentricities increase the collisional velocities (although the collisional rates remain nearly the same, see, e.g., Queck et al.2007) and thus the efficiency of the collisional cascade.

Two simulations are performed: one with reduced ( $e_{\text{max}} = 0.1$ ) and one with increased eccentricity ( $e_{\text{max}} = 0.3$ ). The inclination of the disk is taken to fulfill the energy equipartition condition,  $i_{\text{max}} = e_{\text{max}}/2$ . Since changing  $e_{\text{max}}$ , but maintaining the same distribution of semi-major axes would change the radial extension of the disk,  $a_{\text{inner}}$  and  $a_{\text{outer}}$  are chosen in such a way as to preserve the radial extension of the reference model disk. (Strictly speaking, all this applies to the initial disk, because there is no control over the disk extension at later times in the course of its dynamical evolution.)

The size distribution in Fig. 5.19 shows that higher eccentricities lead to a depletion of larger grains ( $> 30 - 60 \mu\text{m}$ ) and in return to an overabundance of smaller grains close to the blowout size. Consequently, the SED drops beyond  $\sim 200 \mu\text{m}$  and rises at shorter wavelengths becoming more narrow. In contrast, with lower eccentricities more grains of radii  $> 100 \mu\text{m}$  survive, so that fewer particles with  $15 \mu\text{m} < s < 100 \mu\text{m}$  are created in collisions, which results in a more pronounced maximum between the blowout and  $30 \mu\text{m}$ . This yields an enhancement of the radio emission and an overall flatter shape of the SED.



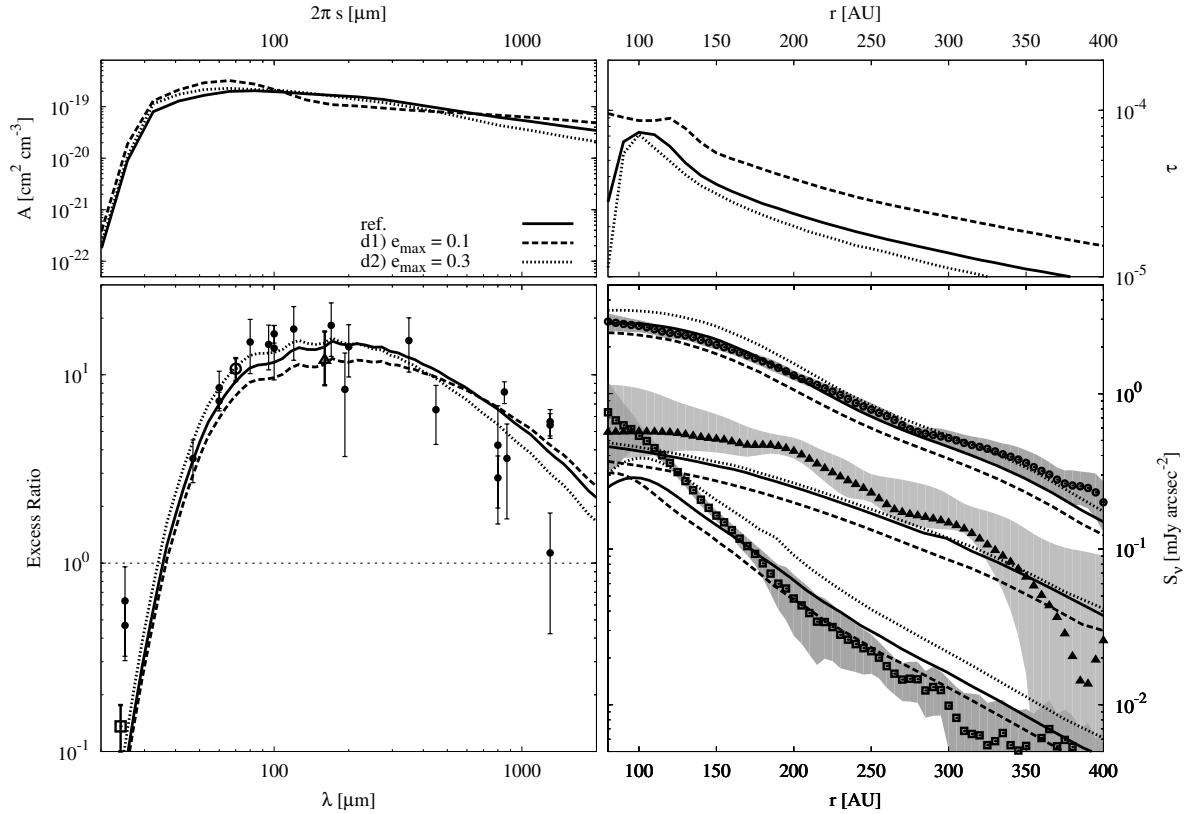


**Figure 5.19:** Same as Fig. 5.16, but for dynamically less (dashed lines) and more (dotted lines) excited model disks.

The slope of the optical depth profile in the outer part of the disk remains nearly unchanged, and it just shifts vertically. However, in the range of the birth ring the optical depth profiles for different  $e_{\text{max}}$  are different: the lower  $e_{\text{max}}$ , the broader the maximum. It is because for higher  $e_{\text{max}}$ , the distribution of semi-major axes is narrower and the collisional production of dust near the center of the ring is much higher than elsewhere. For lower  $e_{\text{max}}$ , the semi-major axes are distributed more broadly and dust is collisionally produced at comparable rates everywhere in the ring.

The brightness profiles respond to the changes in the disk excitation in a similar way. In the outer part they just shift vertically, and most of the changes are in the birth ring region. When  $e_{\text{max}}$  is reduced to 0.1, in the outer disk the  $24 \mu\text{m}$  profile matches the observed profile closely. In the region of the birth ring it is still too low, as is the reference profile. However, the emission now keeps rising inward down to 80 AU, i.e. all the way through the birth ring, as does the observed emission.

### Stellar Luminosity

Changing the stellar luminosity has a two-fold effect on the results. First, it alters the  $\beta$  ratio of the dust grains, affecting their dynamics. Second, a different luminosity impacts the temperature of the dust grains, thereby changing the SED and brightness profiles. Note that all these changes influence only the dust portion of the disk, not the larger objects.

As mentioned above, Vega is a rapid rotator and so the radiation flux emitted from its surface varies with stellar latitude. In the reference model, the “equatorial luminosity” of  $28 L_{\odot}$  was adopted. However, the dust disk “sees” not only the stellar equator, but also receives stellar radiation from higher altitudes. Thus, now the average luminosity of  $37 L_{\odot}$  as derived by Aufdenberg et al. (2006) and, as an extreme case, the canonical polar value of  $57 L_{\odot}$  (used by many modelers

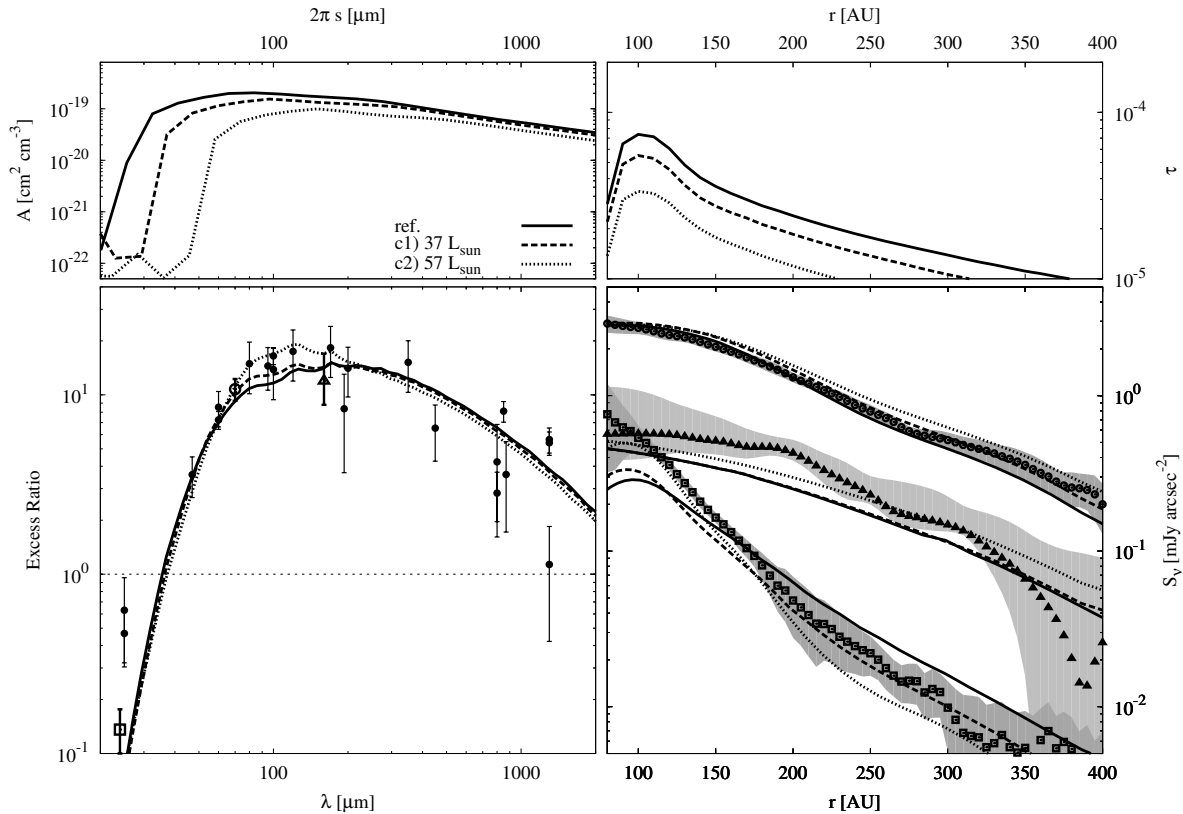


**Figure 5.20:** Same as Fig. 5.16, but assuming a more luminous central star with luminosity of 37 (dashed lines) and  $57 L_{\odot}$  (dotted lines).

before) are tested.

As the luminosity gets higher, the blowout size increases (Fig. 2.1, right), reaching  $10 \mu\text{m}$  for a  $57 L_{\odot}$  central star. The entire size distribution shifts horizontally towards larger sizes and the jump at the blowout radius becomes more abrupt (Fig. 5.20). The optical depth profile preserves its shape, but moves downward. The reason for the decrease of the optical depth level at higher luminosities is simply the increase of the grains' blowout size, so that there are fewer grains that could stay in bound orbits.

Interestingly, the SED in Fig. 5.20 (bottom left) does not change substantially, as to expect from dramatic changes in the size distribution. The reason for moderate changes seen in the figure can be found by analyzing the size distribution (Fig. 5.15, top right) and the temperature plot (Fig. 5.15, top left). Since for a larger  $L_*$  the size distribution is shifted to larger particles, the temperature range of the smallest particles, which affects the outer part of the disk the most, becomes narrower. Consequently, the SED slightly narrows, too, and the maximum at  $\sim 100 \mu\text{m}$  becomes more pronounced.

The changes in the surface brightness profiles are two-fold. While the  $24 \mu\text{m}$  profile steepens with increasing luminosity, the  $160$  and especially the  $70 \mu\text{m}$  curves flatten. The explanation for this behavior is as follows. The farther out from the star, the faster the temperature decreases with increasing grain size (Fig. 5.15, top left). A comparison with the position of the maxima in the size distribution at different distances and for different luminosities (Fig. 5.15, top right) demonstrates that an average temperature in the region of the birth ring increases with increasing  $L_*$ . In the outer disk the effect is reverse: far from the star, a higher stellar luminosity lowers the typical dust temperatures. These effects explain why for higher luminosities the mid-IR emission rises in the inner disk and drops in the outer one, steepening the  $24 \mu\text{m}$  profile. At the same time, the far-IR emission becomes more efficient farther out, which flattens the  $70$  and  $160 \mu\text{m}$  profiles.

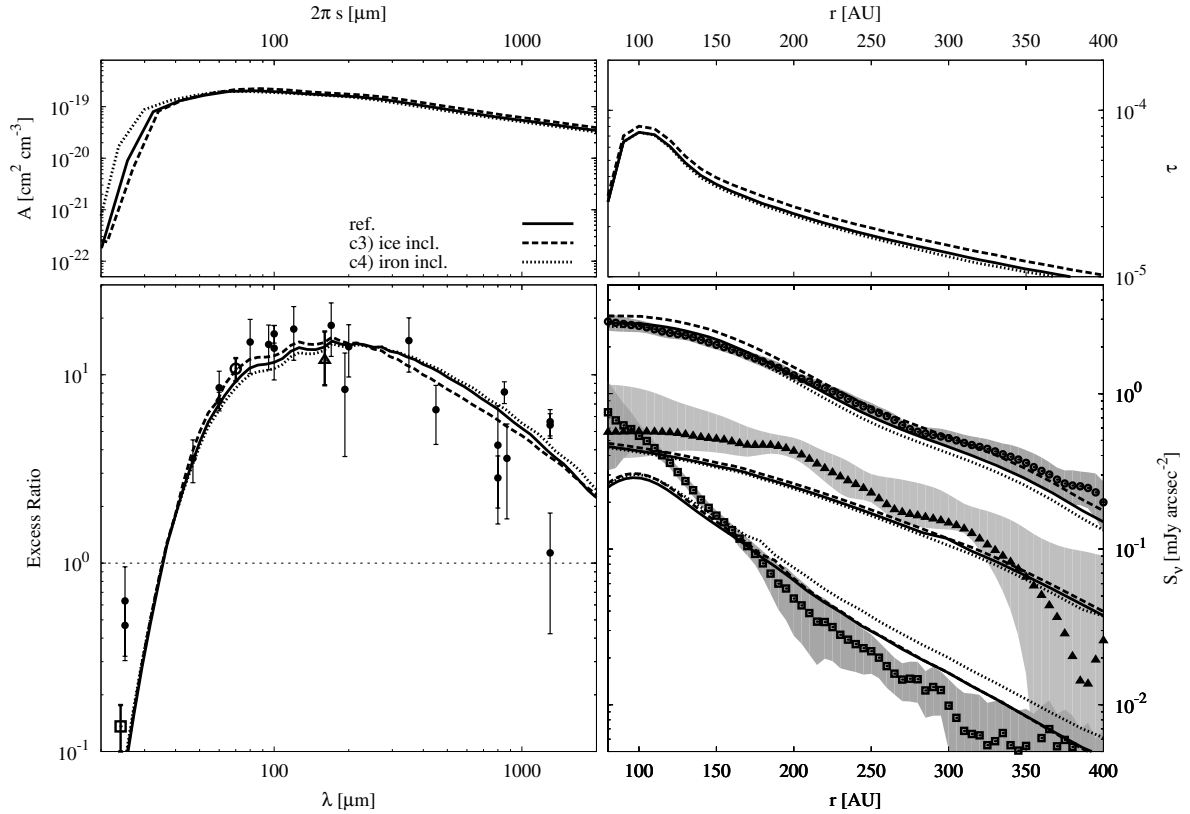


**Figure 5.21:** Same as Fig. 5.16, but for disk of particles consisting of an astrosilicate matrix with 10 % water ice (dashed lines) and iron inclusions (dotted lines).

This analysis definitely favors an intermediate value of the Vega luminosity, exemplified by  $L_* = 37 L_\odot$  in the tests. First, this choice is well justified physically. Indeed, dust is exposed to stellar light coming from a range of latitudes, thus the “right” luminosity should be between the equatorial and polar one. Second, it does provide a better agreement with observations. Changes in the 70 and 160  $\mu\text{m}$  profiles are only marginal, so that they still match the observations well enough, while the 24  $\mu\text{m}$  profile steepens inside  $\sim 250$  AU, coming much closer to the observed profiles.

### Chemical Composition

Like the stellar luminosity, the chemical composition of grains affects both the  $\beta$  ratio (through the radiation pressure efficiency and bulk density) and dust temperatures (through the absorption efficiency).

Mid- and far-IR spectra of some debris disks reveal distinctive features (e.g., Jura et al. 2004; Chen et al. 2006), which allow insight into the mineralogy of the dust grains. For example, spectra of several disks were matched by a mixture of amorphous and crystalline silicates, silica, and several other species (Schütz et al. 2005; Beichman et al. 2005a; Lisse et al. 2007, 2008a), including possibly water ice (Chen et al. 2008). Unfortunately, the spectra of the Vega disk (available in the *Spitzer* archive) do not exhibit unambiguous features, which poses no observational constraints on its composition.

In the reference model pure astrosil was used. To test possible effects of chemical composition, an astrosilicate matrix with water ice (Warren 1984) and iron (Lynch & Hunter 1991) inclusions are considered. The refractive indices are calculated according to the Maxwell-Garnett theory. The amount of inclusions was limited to 10%, which is an upper limit for which the effective medium theory still provides accurate results (Kolokolova & Gustafson 2001). The resulting

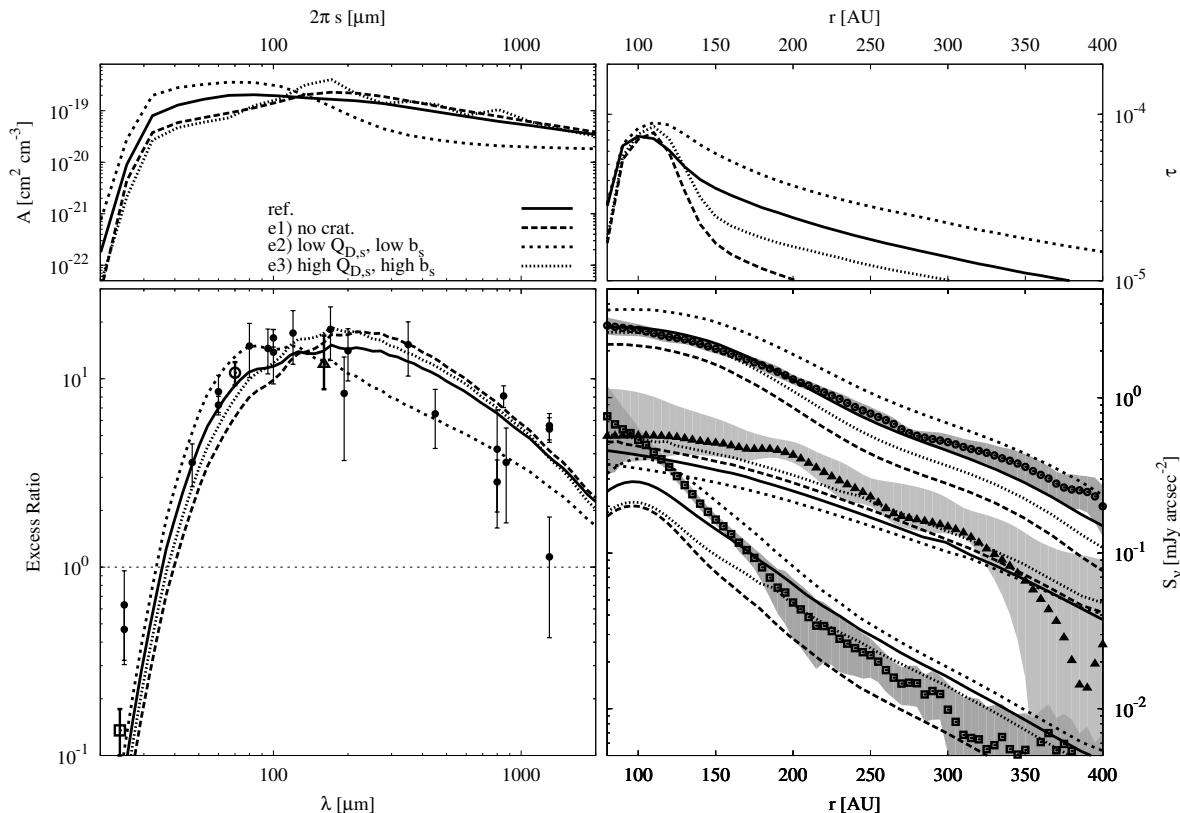


**Figure 5.22:** Same as Fig. 5.16, but for a disk without cratering collisions (long dashed) and for a disk material with lower (short dashed) and higher critical shattering energy (dotted).

bulk densities for the mixtures with ice and iron are  $3.062 \text{ g cm}^{-3}$  and  $3.757 \text{ g cm}^{-3}$ , respectively (compared to  $3.3 \text{ g cm}^{-3}$  for pure astrosilicate). Most of the difference in the size distributions considering the inclusions (Fig. 5.21, top left) comes from the changes in the bulk density and is in agreement with the small modifications of the  $\beta$  ratio (Fig. 5.13). The blowout for grains with iron inclusions is slightly shifted to smaller sizes and the whole distribution is stretched, while in the case of water inclusions the opposite is true. The radial distribution of dust (top right) remains virtually the same.

In terms of thermal emission, the influence of inhomogeneity is very weak, too. This is expected from the minor effects on the absorption efficiencies (except for small grains in the near-IR, Fig. 5.13). Consistently with the modifications in the size distribution, the SED is narrower for ice and slightly broader for iron inclusions. The surface brightness profiles retain their overall shape. Only the  $24 \mu\text{m}$  emission in the outer disk becomes slightly stronger and more gently sloping, when iron inclusions are present.

The conclusion is that inclusions at a 10% level have only minor effect on the observables. It cannot be excluded that more radical changes in the composition would affect the results substantially, but there is currently no observational evidence that would justify such changes.

### Cratering Collisions

Now an analysis of the underlying collisional model implemented in ACE is performed. The detailed physics and outcomes of binary collisions under the conditions of debris disks are poorly known, which represents one of the major sources of uncertainty in the simulation results. Accordingly, in this and subsequent sections, three key parameters that control the treatment of collisions are varied.

First of all a hypothetical collisional cascade is explored, in which only disruptive collisions

operate and the cratering collisions do not occur. This means that only collisions with specific impact energies above the threshold value ( $Q_D^*$ ) are considered, which shatter both colliders completely. All collisions at lower energies (that would in reality erode one or both of the colliders) are simply ignored.

Thus, an efficient way of eroding larger objects by collisions with much smaller grains is switched off. As a result, grains with  $20 \mu\text{m} < s < 300 \mu\text{m}$  are more abundant than in the reference model (Fig. 5.22). And conversely, the number of grains with  $s < 20 \mu\text{m}$  decreases, so that the maximum of the size distribution is now effectively shifted to about  $30 \mu\text{m}$ . The explanation is simple. Excluding cratering collisions prolongs the collisional lifetime of larger grains, because smaller impactors that cannot disrupt but would efficiently erode them, now leave them intact (see, e.g., Thébault & Augereau 2007, and references therein).

The change in the size distribution shifts the SED toward longer wavelengths and slightly narrows it. There is now a lack of emission in the mid- and far-IR up to  $100 \mu\text{m}$  and an excess emission at sub-mm. The resulting SED clearly violates the data.

Given the deficiency of small particles on highly eccentric orbits, it is not surprising that the optical depth profile becomes very steep. As a consequence, the  $70 \mu\text{m}$  brightness profile steepens significantly. In addition, all three profiles fall too low. Like the SED, they are no longer consistent with the observations.

It can be concluded that cratering collisions cannot be ignored. They seem mandatory to reproduce the observations of the Vega disk with collisional simulations.

### Energy Threshold for Fragmentation

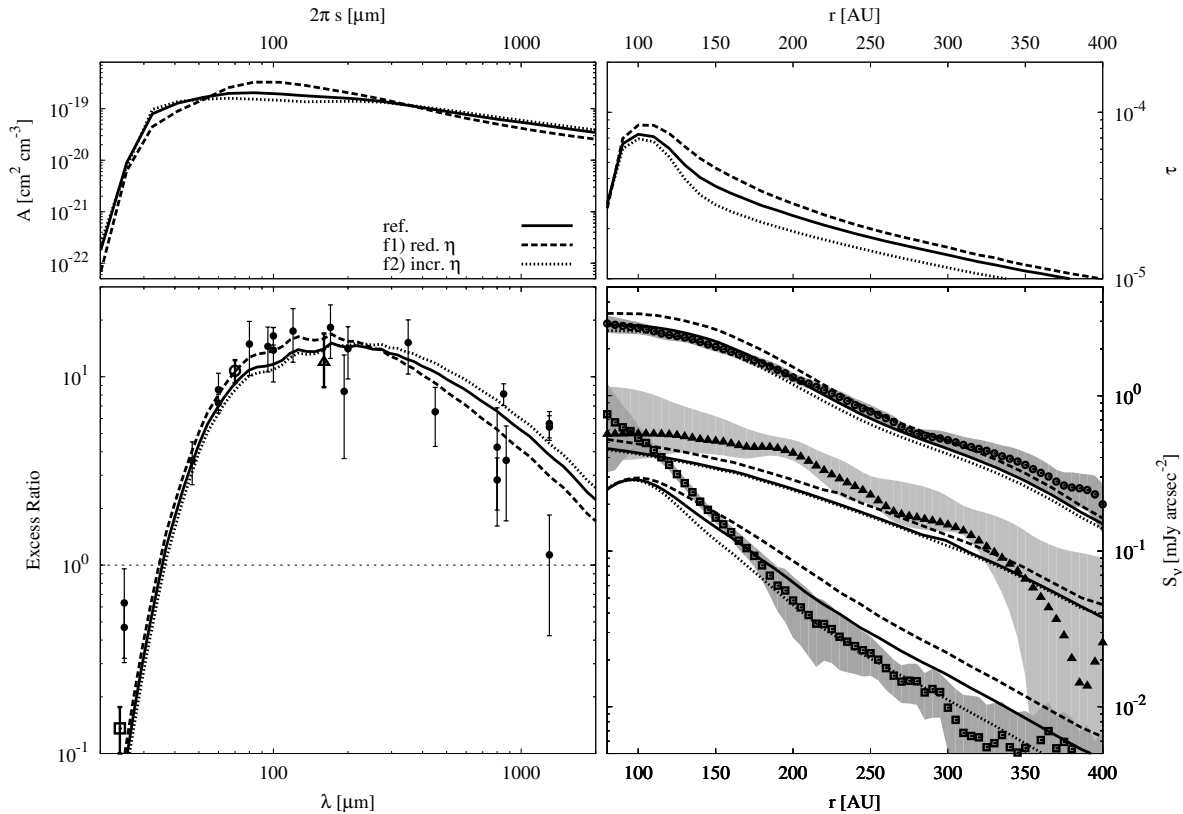
In this subsection, the role of the (unknown) tensile strength of the solids, parameterized by the shattering energy  $Q_D^*$  in the strength regime, is explored. To this end,  $Q_{D,s}$  and  $b_s$  in Eq. (2.57) are decreased in one simulation (“weak material”) and increased in another one (“hard material”).

Figure 5.22 shows that larger grains benefit from an increase of the energy threshold in a similar way they do from neglecting cratering collisions or from lowering the average impact energies. Their collisional lifetime becomes longer and their amount increases. And conversely, a lower  $Q_D^*$  reduces the amount of larger particles. For smaller grains, the number of potentially hazardous impactors is not determined by the change in the critical impactor mass for disruption (that comes along with the change in critical energy) but by the blowout limit, which remains unchanged. Consequently, decreasing  $Q_D^*$  “supports” smaller grains, producing a more pronounced first maximum in the size distribution.

In the SED, a lower critical energy leads to a strong shift of the maximum to about  $80 \mu\text{m}$ , and makes the rise in the mid- to far-IR steeper, whereas the sub-mm and millimeter part lowers and flattens. The opposite changes, albeit less pronounced, are seen for a higher critical energy. In both cases, the agreement between the modeled and observed SED becomes rather worse.

Similar to the size distribution, the optical depth profile responds to a harder material in nearly the same way as to excluding the cratering collisions. As far as the surface brightness profiles are concerned, the only real improvement can be found in the  $160 \mu\text{m}$  profile for larger  $Q_{D,s}$  and  $b_s$ . However, this is accompanied with a steepening and flattening of the  $70$  and  $24 \mu\text{m}$  profiles, respectively, which are then clearly inconsistent with the observations.

Concluding, the usage of “weak” or “hard” material with respect to the nominal one does not generally improve agreement with the observations. When improving one of the three surface brightness profiles, for instance, this makes one or two of the others worse. It was found, however, that results are very sensitive to the critical energy. Thus moderate modifications in the critical energy can be useful for “fine-tuning” of the models.



**Figure 5.23:** Same as Fig. 5.16, but for model disks with a flatter (dashed) and steeper distribution of fragments (dotted).

### Fragment Distribution

One more essential part of the collisional description is the distribution of fragments produced in a single collision. In the reference model their mass distribution was assumed to follow a power-law with an index  $\eta = 1.833$  retrieved from experiments (Fujiwara et al. 1977), but the experimental conditions do not necessarily reproduce the conditions of debris disks. Here, another two disk models are tried, one with an enhanced production of small particles ( $\eta = 1.95$ ) and one with a reduced production ( $\eta = 1.6$ ).

The effect on the size distribution in Fig. 5.23 is not very strong. An increase of  $\eta$  enhances the production of small particles so that the total distribution becomes flatter. This makes the SED broader: the far-IR emission decreases while the sub-mm fluxes are enhanced. Reducing  $\eta$ , however, trims the production rate of small particles, so that the maximum in the size distribution becomes broader and is shifted to about  $15 \mu\text{m}$ . Consequently, the SED becomes somewhat narrower, with a steeper rise in the mid-IR, stronger emission in the far-IR, and a steeper fall-off in the sub-mm. These changes are minor, so that the SEDs for both  $\eta$  values are consistent with the observed SED, as is the SED in the reference model.

Changes in the optical depth are subtle, but not unimportant, particularly at the outer edge of the birth ring. While a lower  $\eta$  makes the optical depth profile smoother, a higher  $\eta$  creates a slight dip at the outer end of the planetesimal belt. In this radial zone, emission stems predominantly from intermediate-sized grains, which are placed by radiation pressure in moderately eccentric orbits, but still cannot reach the outermost regions of the disk. Reducing  $\eta$  increases the amount of these particles compared to the reference model, which smoothens the optical depth profile in this region. And conversely, an increase of  $\eta$  depresses the population of intermediate-sized grains, causing the dip.

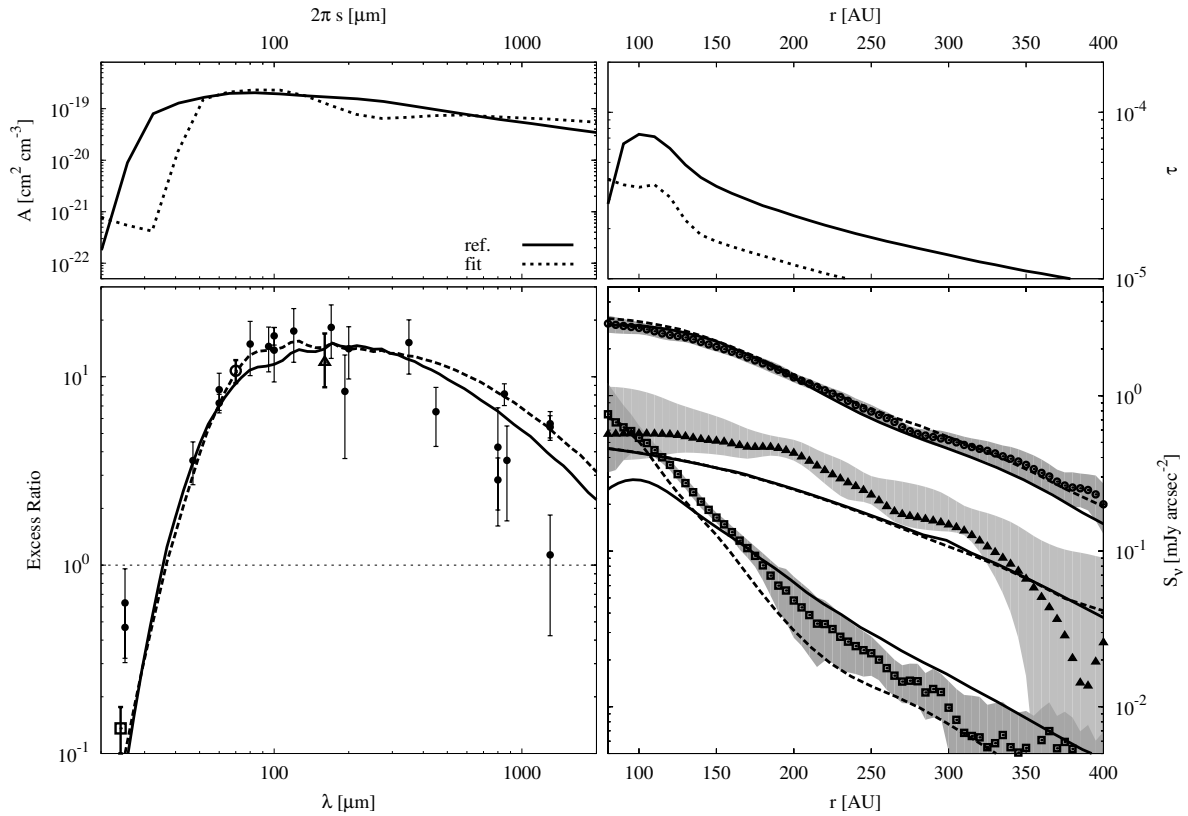


**Figure 5.24:** Same as Fig. 5.16, but for the best-fit model (dashed lines).

In the radial surface brightness profiles these changes are evident in the 24  $\mu\text{m}$  profile, which becomes flatter for small  $\eta$  and steeper for high  $\eta$  in the region up to  $\sim 200$  AU. The vertical shifts are in agreement with the modifications in the SED.

A conclusion is that a steeper size/mass distribution of fragments with  $\eta = 1.95$  makes the 24  $\mu\text{m}$  brightness profile more consistent with the observed ones, without causing new discrepancies in the other two profiles and the SED.

### Best Fit

Different modifications in the previous section have shown no simple way of further improving the agreement of the reference model with the observations. However, it was found that variation of some parameters is able to change the results in the desired direction. It is now to combine several of the modifications that looked promising: the disk is extended inwards, the eccentricities are reduced, the luminosity increased, and a steeper fragment distribution is assumed. Specific parameter values are listed in the last line of Tab. 5.8.

The result is depicted in Fig. 5.24 with dashed lines; as always, solid line shows the reference model for comparison. In terms of the SED (bottom left), all photometry data (aside from the *IRAS* 25  $\mu\text{m}$  points) are reproduced within the error bars shortward of 200  $\mu\text{m}$ . At longer wavelengths, the observational data themselves split into groups that are not in agreement with each other. The model perfectly matches the upper set of points.

In terms of the radial surface brightness profiles, the 160  $\mu\text{m}$  profile is nearly the same as in the reference model. The 24  $\mu\text{m}$  profile is at about  $1\sigma$  in all regions of the disk. From all three curves the 70  $\mu\text{m}$  profile is the closest to the observed one.

### 5.3.4 Discussion

#### Blowout or Bound Grains?

It is interesting to trace, why Su et al. (2005) needed an extremely high amount of blowout grains to explain the *MIPS* observations, whereas the collisional approach was capable of reproducing the same data without any blowout grains (in the models they make a negligible contribution to the SED and radial brightness profiles at all wavelengths considered and at any distance in the disk). By fitting the *MIPS* photometry and radial profiles with a single power-law size distribution, Su et al. (2005) found the best fit to be  $s_{\min} = 1 \mu\text{m}$  and  $s_{\max} = 50 \mu\text{m}$ , with a slope of  $-3.0$ . Assuming nominal stellar luminosity of  $L_* = 60 L_{\odot}$ , already the compact grains have a blowout limit of  $\sim 8 \mu\text{m}$ . However, if the grains are highly porous, which of course they may, then the blowout limit will shift to much larger sizes, so that all grains with  $1 - 50 \mu\text{m}$  could indeed be in unbound orbits. An additional argument to favor the radiation pressure-induced outflow seemed to be the deduced brightness profile at  $24 \mu\text{m}$  with a slope of  $-3$  to  $-4$ , since a  $-3$  slope is what blowout particles with nearly constant “terminal” velocities would produce. At that time, it was not yet realized that slopes in the range  $-3$  to  $-4$  would equally be typical of an extended disk of small bound grains in elliptic orbits around a parent planetesimal ring, as was found later numerically (Krivov et al. 2006; Thébault & Augereau 2007) and analytically (Strubbe & Chiang 2006).

In this study, compact grains and  $L_* = 28 L_{\odot}$  were assumed in the reference model (the very idea to reduce the stellar luminosity would sound strange at the time of the Su et al. (2005) study, because the fast rotation of Vega was not yet discovered). As a result, the blowout radius reduces to  $\sim 4 \mu\text{m}$ . Hence, where Su et al. had  $1 - 50 \mu\text{m}$  grains, here  $4 - 50 \mu\text{m}$  ones are primarily present. For a  $-3.0$  size distribution slope, the emitting cross section area is equally distributed over the sizes. Thus, even taking into account that smaller grains are somewhat hotter than larger ones, by excluding the  $1 - 4 \mu\text{m}$  subrange not much of the  $24 \mu\text{m}$  emission is lost compared to Su et al.. The radial distribution of dust in the new model, as explained above, is not very different either. That is why a similar level of  $24 \mu\text{m}$  emission is found. In terms of dust mass, the difference is even smaller. Indeed, the dust masses derived here ( $6.6 \times 10^{-3} M_{\oplus}$  in the reference model, see Tab. 5.9) are close to those derived by Su et al. ( $2.8 \times 10^{-3} M_{\oplus}$ ).

#### Mass Loss from the Disk

To estimate the mass loss from the disk, the total mass of dust (up to  $1 \text{ mm}$ ) in the reference model is considered  $\sim 7 \times 10^{-3} M_{\oplus}$  (Table 5.9). Assuming for simplicity that the size distribution follows a  $-3.5$  power-law, the mass of the smallest bound grains (say, up to  $10 \mu\text{m}$ ) is  $\sim 7 \times 10^{-3} M_{\oplus} \times \sqrt{10 \mu\text{m}/1 \text{ mm}} \sim 7 \times 10^{-4} M_{\oplus}$ . The steady-state mass of blowout grains is then by a factor of 100 smaller (a strength of the dip in the size distribution, which is the ratio of the collisional lifetime of bound grains to the disk-crossing time of unbound ones, see Fig. 5.15 right), giving  $\sim 7 \times 10^{-6} M_{\oplus}$ . Their lifetime is  $\sim 1000 \text{ yr}$ , so that the mass loss rate is  $\sim 7 \times 10^{-9} M_{\oplus} \text{ yr}^{-1}$ . Therefore, over the system’s age,  $350 \text{ Myr}$ , the disk must have lost  $\sim 2 M_{\oplus}$  of material. This estimate is consistent with the difference between the initial and final disk masses given in Tab. 5.9, typically a few  $M_{\oplus}$ .

#### The $24 \mu\text{m}$ Emission

It was “the  $24 \mu\text{m}$  problem” — an apparently too strong and radially extended  $24 \mu\text{m}$  emission compared to what was expected from dust in bound orbits — that triggered debate on whether the Vega disk contains an excessive number of small blowout grains, incompatible with a steady-state collisional cascade (Su et al. 2005). Thus, now it is discussed in more detail how the  $24 \mu\text{m}$  flux predicted by the models above compares to *Spitzer* data.

Although the models presented here are in a reasonable agreement with observations, most



of them somewhat underestimate the observed 24  $\mu\text{m}$  emission in the parent ring region, at 80 – 120 AU or  $10'' - 15''$ , while slightly overestimating it farther out from the star. As a result, the total flux outside  $10''$ , which is dominated by the flux from the ring region, is slightly below the observed value. For example, the reference model predicts 0.40 Jy outside  $10''$ , while the observed flux is 0.53 Jy. These deviations are subtle and probably not of serious concern. It may be argued that they may simply be caused by the roughness of the model (see Chapter 5.4.2). Indeed, it was possible to find a combination of model parameters (Chapter 5.3.3) which reproduced the observed 24  $\mu\text{m}$  profile outside  $10''$  quite well.

However, the question of 24  $\mu\text{m}$  emission from the inner system ( $< 10''$ ) remains open. Data reduction as summarized in Chapter 5.3.1 yields a total 24  $\mu\text{m}$  flux from  $4''$  (30 AU) outward of 0.94 Jy, although the true value may be lower, because central part of the *MIPS* images is saturated. Assuming, however, the data to be accurate, the rise of the 24  $\mu\text{m}$  flux from  $10''$  inward can hardly be explained with the models presented here. A natural explanation would be an additional dusty belt in the system at  $\sim 10$  AU. Such a belt could enhance the 24  $\mu\text{m}$  emission coming from the “main” disk. As yet it is not clear, however, if any constraints on such a belt can be found in the *Spitzer/IRS* spectrum of Vega. Nor is it clear whether the inner system may accommodate such a belt if, as conjectured, it hosts one or more close-in planets. In the future, this simple hypothesis could be checked or falsified directly, for instance with mid-IR interferometry.

### The 850 $\mu\text{m}$ Emission

So far, sub-mm and radio images have not been considered explicitly. The main reason for that is a low resolution of such measurements, implying that only weak constraints can be put on the radial brightness profiles at long wavelengths. However, at least the total flux at sub-mm wavelengths derived from the images serves as an additional test to the models.

In an analysis by Su et al. (2005), the observed sub-mm emission could not be reproduced with a two-component dust disk (2  $\mu\text{m}$  and 18  $\mu\text{m}$  in radius) that was sufficient to fit all available data at shorter wavelengths. To cope with the problem, they artificially added a population of larger grains, with a radius of 215  $\mu\text{m}$ . In this new approach, solids from dust to planetesimals have a continuous size distribution, which is not postulated, but physically modeled. From Figs. 5.16 – 5.24 (left bottom panels), it is apparent that the simulations naturally reproduce the sub-mm flux with a reasonable accuracy. An additional consistency check is to calculate the 850  $\mu\text{m}$  profile of the best-fit model (Chapter 5.3.3) and convolve it with a Gaussian of  $16''$  beam size. The resulting profile is then compared with the *SCUBA* profile extracted by Su et al. (2005) from the original images published by Holland et al. (1998). The modeled profile is slightly narrower than that observed and the maximum between 50 and 100 AU is by a factor of two lower. Given the large width of the PSF and calibration uncertainties of *SCUBA* observations, and that Mie calculations likely underestimate sub-mm emission (as discussed in Chapter 5.4.2), the agreement with the data is deemed satisfactory.

### The Role of the Poynting-Roberston Effect

PR drag mostly affects smallest particles and thus emission at shortest wavelengths considered. The PR force moves such grains inward, placing some of them interior to the inner edge of the birth ring. The warm emission of these particles especially around the inner edge of the birth ring should increase.

However, with the Vega disk’s relatively high optical depth ( $8.3 \times 10^{-4}$  at 100 AU in the reference model), the collisional timescales of dust grains are shorter than timescales over which PR drag causes their appreciable radial displacement (Fig. 5.14). Thus the Vega disk can be referred to as a collision-dominated, rather than transport-dominated disk (Krivov et al. 2000;

Wyatt 2005b). Still, it is useful to check to what extent PR drag may affect the results in terms of SED and brightness profiles.

To this end, PR drag is switched on in the reference model. Unfortunately, when a drag force, the PR force in this case, is added to a collisional model, the mass-time scaling law (Chapter 2.5.2) is no longer valid. The initial disk mass is required that yields a disk with the “correct” dust mass after 350 Myr, i.e. the dust mass that gives the maximum of the SED at the level actually observed. This means trial and error, i.e. several *ACE* runs with different initial disk masses followed by *SEDUCE* and *SUBITO* runs. What makes the modeling even more demanding, is that the presence of a drag force implies diffusion in the phase space of pericenters and eccentricities, which slows down each *ACE* run appreciably. Four *ACE* runs had to be performed, each of which took about 20 core-days CPU time.

The “right” dust mass after 350 Myr of evolution with PR is achieved when the initial disk mass is set to  $20.5 M_{\oplus}$  (instead of  $18.9 M_{\oplus}$  in the reference model without PR), and the final disk mass is  $18.0 M_{\oplus}$  (instead of  $16.3 M_{\oplus}$  without PR). As expected, the influence of PR on the  $160 \mu\text{m}$  and  $70 \mu\text{m}$  turns out to be completely negligible. At  $24 \mu\text{m}$ , the emission in the outer disk increases by  $\sim 10\%$  and in the birth ring (at 80 AU) by  $\sim 60\%$ . Thus the whole  $24 \mu\text{m}$  profile gets somewhat steeper, and agrees with observations slightly better than the original profile in the reference model (solid lines in Figs. 5.16–5.24). However, the improvement is only minor, and it is to conclude that the PR effect can safely be neglected in modeling the Vega system.

### Presumed Planets in the Vega System

One major caveat not discussed yet is that the collisional model, implemented in the *ACE* code, ignores effects of a possible planet (or planets) interior to the planetesimal belt. Below, the facts that point to the presence of such planets in the Vega system are briefly outlined, and it is discussed to what extent these perturbers may affect the observed properties of the debris disk.

Asymmetries in the Vega disk were first discovered by Holland et al. (1998) in a *SCUBA*  $850 \mu\text{m}$  image, and subsequent sub-mm and radio observations have confirmed a clumpy ring structure. Wilner et al. (2002) introduced the idea of a Jupiter-mass planet trapping dust in mean-motion resonances. They applied *N*-body simulations and thermal emission calculations to model this scenario and achieved a reasonable agreement with their *IRAM* map. An in-depth investigation on the Vega system dynamics was performed by Wyatt (2003) who suggested that a Neptune-mass planet, migrating outward from 40 to 65 AU over a time span of  $\sim 56$  Myr, may have cleared the inner part of the assumed planetesimal disk and trapped a significant amount of material in the 3 : 2 and 2 : 1 resonances, thus creating two clumps as seen by Holland et al. (1998). Later on, Reche et al. (2008) generalized this theory to account for eccentric planetary orbits. Their findings are similar to those of Wyatt (2003) with the difference that they require a Saturn-mass planet on a low-eccentricity orbit to account for the brightness asymmetry. For the clumps to be visible against the non-resonant background, low planetesimal eccentricities of  $< 0.1$  are necessary. Planets with masses greater than  $\sim 2 M_{\text{Jupiter}}$  would raise planetesimal eccentricities to about 0.2. Besides, too massive planets would quickly deplete the disk.

As shown in Chapter 5.3.3, the simulations slightly favor low planetesimal eccentricities up to 0.1. This is in agreement with the limit given by Reche et al. (2008). Still, a question arises whether non-inclusion of the azimuthal structure in the simulations (*ACE* treats rotationally symmetric disks) is a reasonable assumption. Indeed, Wyatt (2006) investigated the dust production in a clumpy disk of resonant planetesimals and showed that local dust production from the clumps is strongly enhanced and conversely, it is depressed between the clumps. However, the net effect on the SED and radial profiles of brightness is much weaker, because these depend on the azimuthally averaged dust production rates. Queck et al. (2007) found that the average collisional rate in a resonant planetesimal belt is typically not more than twice as high as in a similar

non-resonant belt, while the average collisional velocities are nearly unaffected by the resonant clumping. Thus a collisional cascade in a resonant, clumpy belt can be approximated by a cascade in a non-resonant, rotationally symmetric belt with the same mass at the same location, but somewhat higher orbital eccentricities of planetesimals to mimic moderately enhanced collisional rates. Note that this is only valid when considering azimuthally averaged observables, not the azimuthally resolved structure seen in the images. For example, the collisional approach is not suitable to make predictions for spiral structure expected to emanate from the clumps. Wyatt (2006) argues that such structure should be seen in mid- to far-IR images, and that it is not, may simply be due to insufficient resolution of the *Spitzer/MIPS* images or confusion in the photospheric subtraction.

Throughout the study, the initial eccentricities and inclinations of the parent bodies in the planetesimal belt were assumed to be distributed according to energy equipartition. This assumption would be reasonable if the distribution of orbits was controlled by mutual collisions and gravitational scattering among planetesimals, but it may not hold as soon as resonant interaction with planets occurs. A well-known example is the Kuiper belt, in which the eccentricities and inclinations of objects are distributed differently (e.g., Brown 2001).

Apart from the suspected planet that sculpts the main belt, the Vega system may contain more planets closer in. In fact, a damped outward migration of the presumed planet that explains the clumps requires the presence of another, more massive planet in the system closer in (e.g., Gomes et al. 2004). An inner planet, or planets, could stir the disk (Mustill & Wyatt 2009). Furthermore, several planets together could produce intricate combined dynamical effects on the main planetesimal belt and its dust. However, it seems premature to discuss them until new observations have delivered evidence for these planets.

### The Exozodi in the Vega System

As mentioned in the Chapter 5.3.1, dust was surprisingly discovered in the innermost part of the Vega system, inside 1 AU (Absil et al. 2006). Although reminiscent of the zodiacal cloud of the solar system, this “exozodi” of Vega remains a mystery. It seems to be far too dusty, and the grain sizes retrieved from observations far too small, to be explained by collisions in an “asteroid belt” or evaporation of comets. One possibility would be a transport of planetesimals from the “main” debris disk inward and their subsequent disruption or evaporation. Such a transport would require the presence of at least two planets. In fact, a two-planet configuration — a “Jupiter” inside and a “Saturn” outside that shapes the main disk — could suffice (Vandepoort et al., in prep.). Thus, the very existence of the exozodi may strengthen the expectation that Vega hosts several planets, as discussed above.

The direct contribution of the exozodi to the emission at 24  $\mu\text{m}$  amounts to  $\sim 0.6$  Jy. This is about the emission which is lacking provided the used photometry data are accurate. However, as the exozodi could not be resolved with *Spitzer* and the image is saturated at the stellar position, this very inner part of the Vega disk cannot have affected the observation in the outer parts of the system and can therefore be considered negligible. Still, if not directly, the Vega exozodi could have an indirect impact on the measured dust emission. Dust inside 1 AU could have a shielding effect on dust located farther out. However, a simple estimate shows that the amount of stellar radiation to which outer dust is exposed would only reduce by a factor of  $\sim 10^{-5}$ . Thus, the conclusion is that the very inner part of the system has no impact on the outer disk’s emission analyzed in this work.

## 5.4 Discussion

### 5.4.1 Advantages

One major advantage of the new way of modeling debris disks is that all model parameters are physically motivated and describe certain physical effects and processes. Therefore the resulting distribution of dust and planetesimals spares additional interpretation of its sensibleness. Furthermore, a successful fit does not only provide information about disk location and dust masses, as was the main result in the classical approach, but also provides direct insight into the processes at work in the considered disk. Hence, best fit parameters for example for the collisional prescription as found for the Vega system can now be used as the standard choice for upcoming modeling attempts.

Including the disk's dynamical evolution into the fitting process ends up in additional knowledge about valuable planetesimal properties. That, first, makes the modeling more self-consistent, as it includes the sources of dust, which is finally fitted to the observations. Second, it opens the door to draw conclusions concerning earlier stages of the disk's evolution. Adopting a "collisional age" of the system and provided the relative velocities in the debris disk phase prevent the material from growing any further, the found initial mass of planetesimals in the debris disk modeling gives an estimate on the amount of planetesimals formed in the protoplanetary disk. In the future it may even be possible to unravel initial sizes of planetesimals.

Like for every multi-parameter fitting approach, here a degeneracy occurs, too. However, compared with classical modeling attempts, this degeneracy is not so pronounced: although different modifications may have similar effects on the resulting thermal emission, almost every parameter has a unique impact on SED and surface brightness profiles. This allows to find strong constraints at least for those parameters to which the model is very sensitive.

### 5.4.2 Caveats and Disadvantages

The most apparent disadvantage of this collisional modeling approach is the long computation time. To model an observed system in detail may take several weeks, depending on the amount of observational data. However, as shown in Chapter 5.2 a pre-modeled grid of reference disks can already be used to quickly deduce first estimates on important disk properties. Besides that, it is not possible to control the dust's size and spatial distribution within this approach. Only initial planetesimal properties are subject to modifications. Hence, it is not to be expected that final fitting results can compete with those obtained in the classical way in terms of fitting accuracy.

Further, this approach, as every other, involves a number of simplifying assumptions that may limit the applicability and influences the results. Here, the most important caveats are listed.

Many assumptions have been made in describing collisional physics. The collisional prescription approximates the critical shattering energy with two power laws (Eq. (2.57)), which may be particularly crude at dust sizes (e.g., Thébault & Augereau 2007). Further on, any dependence of  $Q_d^*$  on impact velocity (e.g., Benz & Asphaug 1999; Stewart & Leinhardt 2009) was neglected. The mass of the largest fragment and the distribution of smaller debris may deviate from what was assumed here, and any real disk should be composed of objects whose mechanical properties (and even the bulk density) vary from one object to another (e.g., pre-shattered objects could be less dense and more loosely bound than pristine ones).

A major simplifying assumption in treating the dynamics of planetesimals and their dust is that alleged planetary perturbers interior to the main belt were ignored. The consequences are already exemplarily discussed in Chapter 5.3.4 for the Vega system<sup>4</sup>. At dust sizes, PR drag was not taken into account, its role was discussed in Sect. 5.3.4. Small dust particles were assumed to be

---

<sup>4</sup>In principle the kinetic theory is also capable of handling such asymmetry inducing effects. However, this means an extension of the phase space making simulations even more computationally demanding.

released with the same inclinations as their parent bodies. However, radiation pressure increases relative velocities especially of small particles. Thus, by scattering in mutual collisions these grains reach higher inclinations (Thébault 2009). On the one hand, this will increase relative velocities, but on the other hand decrease collisional probabilities. It is difficult to predict the impact on the modeling results a priori.

While calculating the radiation pressure force acting on dust grains, the particles were assumed to be compact and spherical, thus ignoring possible non-radial effects (e.g., Kimura et al. 2002). Like mechanical properties, optical properties of dust may vary from one grain to another, resulting in different response to radiation pressure, different temperatures, and different thermal fluxes even for like-sized particles (Krivov et al. 2006). Furthermore, even spherical particles are treated in an approximate way. Mie theory was applied to model the emission properties. Although this method is classical and commonly used, it should be treated with caution. One particular concern is that Mie calculations probably underestimate the emission in the sub-mm and radio due to neglected shape effects (Stognienko et al. 1995; Krivov et al. 2008).

The modeling approach used here is based on the (mass) scalability of the ACE simulations. As mentioned before, scaling laws as presented in Chapter 2.5.2 only hold in the absence of transport mechanisms, thus excluding earlier-type stars (see Chapter 5.4.3).

### 5.4.3 Possible Model Extensions

#### Transport Mechanisms

As described in detail in Chapter 5.1, the possibility of making use of the scaling laws, especially the mass scaling, limits the computational requirements to a reasonable amount. However, this is only of use, if transport mechanisms like PR or wind drag can be neglected. This is no longer the case, first, when the systems become tenuous so that (at least for small grains) collisional destruction can only work on larger timescales than the inward spiraling due to drag forces (e.g., Minato et al. 2006). Second, transport processes become important for late-type stars. In such systems, stellar winds become strong enough to have an appreciable effect on the disk dynamics (e.g., Mukai & Yamamoto 1982; Augereau & Beust 2006).

Taking these processes into account demands a number of additional simulations, once a set of parameters is chosen, in order to find the appropriate mass at the given age of the system of interest (remember, that only initial conditions can be fixed, but the disk's evolution is autarkic). To make the situation even worse, simulations including transport mechanisms are typically more time-consuming. Thus, modeling a transport-dominated debris disk is a very cumbersome task, provided computational capabilities do not improve dramatically in the near future. Chapter 5.3.4 has already delivered a brief insight into the expected obstacles.

However, there is a possibility to model such disk systems with a reasonable computational expenditure. Therefore, the idea of a grid of reference disks as presented in Chapter 5.2 is picked up. As preparation for the detailed modeling of transport-dominated disks, a set of disks with a much larger parameter space has to be compiled. The minimum choice of parameters would be stellar spectral type (with typical values for stellar masses, luminosities, and wind strength), disk location (considering typical extensions for the given distance), and of course initial disk mass. Especially the last parameter grid has to be quite fine-meshed, since the final spatial and grain size distributions are very sensitive to the initial mass in the presence of transport mechanisms. Besides that, it would be helpful, to extend the grid in the way it was performed in Chapter 5.3 for the Vega disk for single reference disks, to see in how far the effects of these additional parameters depend on the parameters of the superordinate grid. If equipped in such a way, the best-fit reference run can be sought, and based on this, additional modifications are straight forward. As minor changes in the disk parameters are not expected to result in essential changes of the disk and dust masses, computational efforts due to the additional mass fitting are kept low.

## Porosity

So far, all disk constituents were considered solid, compact spheres. Unfortunately, there is no reliable source of information that gives any hint about particle shapes and structures in debris disks. Nevertheless, a glimpse of a debris disk's analog in the solar system shows a large variety of features. In this section, porosity is in the focus of interest. However, here only a brief insight in this complex field can be provided. For a more detailed discussion of how to include porosity in debris disk modeling see Müller et al. (in prep.).

Britt et al. (2002) have estimated porosities for a set of 23 asteroids based on bulk densities, reflectance spectrum, and grain density and average porosity of analog meteoroids. In general they found high porosities ranging up to 75% with an accumulation at 25 – 55%. Also meteorites, which are believed to stem from asteroids, show proof of porosity. Nevertheless, depending on the meteorite type, it is very difficult to estimate reliable porosities as it is not clear in how far such objects have been altered by contamination (weathering) and microporosity. Taking all these issues into account, Consolmagno et al. (1998) estimated an average porosity of  $\sim 11\%$  for ordinary chondrites.

The situation is more difficult when coming to objects in the outer part of the solar system. Taking the orbits of KBOs and comparing them to measured light curves allows a density estimate (e.g., Trilling & Bernstein 2006; Duffard et al. 2009). The found densities lie in the range of the bulk density for ice or even below. This is indicative for an appreciable porosity of more than 10%. Still, results are highly uncertain.

Besides that, cometary dust was found to be porous. Different kinds of observations, like in-situ (e.g., Divine et al. 1986; Lamy et al. 1987), polarimetric or spectroscopic measurements (e.g., Jewitt 2004; Harker et al. 2005; Jones et al. 2008) for different comets were indicative of the dust, which emanates from the evaporating core, not being solid.

Observations in the solar system and laboratory and numerical studies on the formation and growth of dust and planetesimals suggest particles to have a considerable porosity (e.g., Witten & Cates 1986; Shen et al. 2008, 2009; Wada et al. 2009).

All these are strong indications that also material around other stars may be porous. Hence, in the following a simple approach will be introduced, how this effect can be incorporated in the framework of the collisional modeling approach.

**A simple porosity model** needs to be implemented, to make it applicable for the modeling approach. Analyzing Comet Halley ejecta, Divine et al. (1986) and Lamy et al. (1987) found the ejecta bulk density to be a function of grain size. This can be rewritten in terms of porosity  $p$ :

$$p(s) = p_{\text{start}} + \frac{s}{s_0 + s}(1 - p'), \quad (5.1)$$

with  $p' = 1 + p_{\text{start}} - p_{\text{max}}$ ,  $p_{\text{start}}$  the smallest considered porosity for small particles,  $p_{\text{stop}}$  the upper porosity limit, and  $s_0$  the grain size where porosity reaches the intermediate value between  $p_{\text{start}}$  and  $p_{\text{max}}$ . This of course cannot hold for infinitely large objects as larger bodies will be compacted due to self gravity (Housen et al. 1999). Unfortunately, no measurements are available, showing a clear trend of how porosity reduces with the object's size. Therefore, the model from Eq. (5.1) is simply reversed for larger particles, so that it becomes

$$\tilde{p}(s) = p_{\text{max}} - \frac{s}{\tilde{s}_0 + s}(1 - \tilde{p}') \quad (5.2)$$

with  $\tilde{p}' = 1 - p_{\text{max}}$  and  $\tilde{s}_0 = 1$  km. In general, porosity  $P(s)$  as a function of grain size can then be expressed as

$$P(s) = \min(p(s), \tilde{p}(s)). \quad (5.3)$$

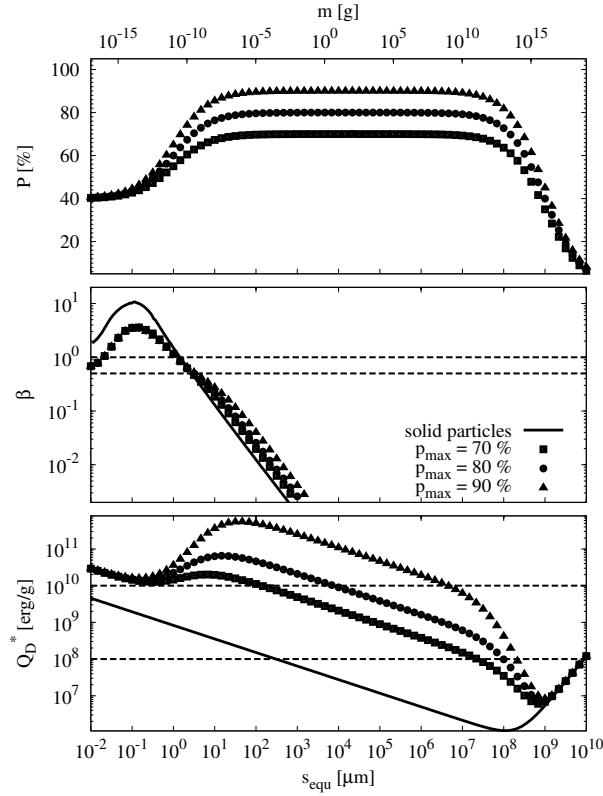


**Figure 5.25:** Top: Porosity as a function of (mass equivalent) grain size for upper porosity limits of 70 (squares), 80 (spheres), and 90% (triangles). Middle:  $\beta$  ratio for the three porosity cases. The  $\beta$  ratio for solid particles (solid line) is added for comparison. Horizontal, dashed lines are the same as in Fig. 5.13. Bottom: Critical specific energy threshold  $Q_D^*$  for fragmenting collisions for the same three porosity cases. The solid line again gives the results for solid particles. The area between the horizontal, dashed lines indicates the region of typical impact energies.

The upper plot in Fig. 5.25 shows the result of Eq. (5.3) for  $p_{\max} = 70, 80,$  and  $90\%$ , with  $p_{\text{start}} = 40\%$  and  $s_0 = 1 \mu\text{m}$ .

**Thermal emission properties** for particles of irregular shape and structure are in principle difficult to compute because very sophisticated emission models need to be applied in order to achieve a satisfactory accuracy. However, Mukai et al. (1992) studied the emission properties of porous dust aggregates and found that in a first approximation Mie theory with some minor modifications can be considered to mimic the more elaborate approaches. Therefore, some definitions are necessary.

For a particle of mass  $m$ , the mass equivalent grain size is given as

$$s_{\text{equ}} = \sqrt[3]{\frac{3m}{4\pi\rho}}, \quad (5.4)$$

where  $\rho$  is the material's bulk density, not the body's averaged density. This is the size which a sphere would have, if all material was compacted. Note that the grain size in Eqs. (5.1) – (5.3) has to be interpreted as mass equivalent size. Another important size definition is the characteristic size

$$s_{\text{char}} = \frac{s_{\text{equ}}}{(1 - P(s_{\text{equ}}))^{1/3}}, \quad (5.5)$$

which can be interpreted as the averaged geometrical grain size of a sphere for an object of mass

$m$  and porosity  $P(s_{\text{equ}})$ . Using these definitions, emission properties, in particular absorption and radiation pressure cross sections were found to resemble more accurate calculations if the characteristic size instead of the mass equivalent size is used (e.g., Hage & Greenberg 1990; Mukai et al. 1992; Kimura et al. 1997; Shen et al. 2009). As an example, Eq. (2.38) changes to

$$F_{\lambda,\text{disk}}^{\text{tot}} = \frac{2\pi}{D^2} \int r(T_g) \frac{dr(T_g)}{dT_g} dT_g \int ds_{\text{equ}} N(r, s_{\text{equ}}) C_{\lambda}^{\text{abs}}(s_{\text{char}}(s_{\text{equ}})) B_{\lambda}(T_g). \quad (5.6)$$

Effective medium theory (Maxwell-Garnett mixing rule) was applied to derive refractive indices. Porosity is imitated by vacuum inclusions with the volume fraction  $f_{\text{vac}}(s_{\text{equ}}) = 1 - P(s_{\text{equ}})$ .

**Dynamics** are affected in two ways. First, the response to stellar radiation changes. Following Mukai et al. (1992), this can be implemented in the same way as for the thermal emission properties by simply replacing  $s$  by  $s_{\text{char}}$  in Eq. (2.48). Applying the three cases with maximum porosity of 70, 80, and 90% from above together with the stellar parameters for Vega, leads to the middle plot of Fig. 5.25. As to be expected,  $\beta$  decreases with increasing porosity, shifting the blowout slightly to larger (or better: more massive) particles.

Second, impact probabilities are altered due to the modified cross section of porous grains. Thus, both geometrical ( $\sigma = \pi s_{\text{char}}^2$ ) and gravitational cross section (Safronov factor) must be adjusted. Consequentially, due to the larger cross section areas, the impact probability increases.

**The collisional outcome** is most likely subject to massive changes, if porosity effects are taken into account. One of the most impressive examples is the C-type asteroid Mathilde. With its  $66 \times 48 \times 46$  km scale and a measured density of  $\sim 1.3 \text{ g cm}^{-3}$ , its porosity is estimated to  $\sim 50\%$  (Britt et al. 2002). Mathilde's surface exhibits an unusual high number of large craters with diameters exceeding the asteroid's size. Surprisingly, still all these craters are relatively well preserved, which is not consistent with the outcome of collisional events among objects with compact structure but requires high porosities (Chapman et al. 1999).

As shown in laboratory experiments and numerical simulations, responsible for such dramatic changes is dissipation of an appreciable amount of impact energy in compaction (e.g., Housen et al. 1999; Jutzi et al. 2008; Fujii & Nakamura 2009). As a consequence, the specific energy threshold for fragmentation increases. Love et al. (1993) found in hypervelocity experiments with porous, sintered glass aggregate targets  $Q_{D,s}$  to scale with

$$Q_{D,s} \propto (1 - P)^{-3.6}. \quad (5.7)$$

Applying this to the three cases from above and adopting the same parameters as presented in Chapters 5.2.2 and 5.3.2,  $Q_D^*$  values as shown in the bottom plot of Fig. 5.25 arise. The values increase dramatically with porosity, which will yield a decrease of ejected material. This is supported by laboratory studies (Housen et al. 1999) and numerical investigations (Jutzi et al. 2008). However, Eq. (5.7) has to be taken with caution as it is highly uncertain.

This unveils an inconsistency which is connected to the scaling in Eq. (5.7). Compaction should lead to a successive decrease of porosity in the course of the disk evolution, so that at older ages the average porosity should be below the initial one. Dealing properly with this problem would require to implement porosity as a new phase space variable. In the numerical model, due to the lack of reliable collisional data and computational capacities, such an extension is not feasible.

Beyond the critical specific energy threshold, there are, unfortunately, no other reliable information available about possible changes in the other parts of the collisional prescription. This is specially a miserable coincidence regarding the sensitivity of the modeling results towards the slope of the fragment distribution (see Chapter 5.3.3).



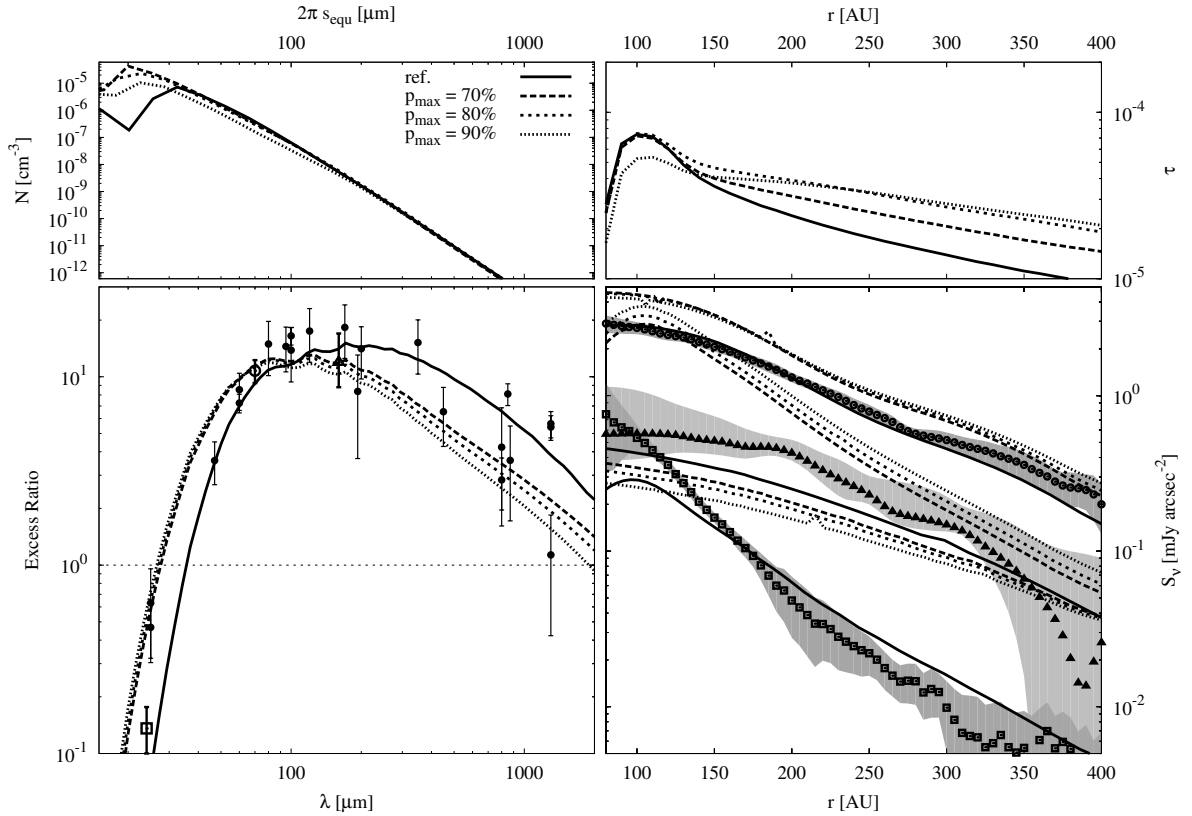


**Figure 5.26:** Same as Fig. 5.16, but for porous disk constituents with upper porosity limits of 70, 80, and 90%. In contrast to previous plots, the size distributions here are given in terms of the surface number density as a function of  $2\pi s_{\text{sph}}$ .

**New Disk Models** are simulated with a modified ACE version that includes all changes described above. The Vega reference model (see Chapter 5.3.2) is taken for a starting point. With changes as shown in Fig. 5.25 for the  $\beta$  and  $Q_D$  values and with the modifications in the particles' cross sections the dust distributions depicted in the upper panel of Fig. 5.26 emerge. In contrast to earlier size distribution plots it is no longer the cross section surface density per unit size decade but the surface number density that is used. The reason is simply that due to the porosity, it is no longer the particles' mass alone that expands into the cross section area but also the porosity (characteristic size) is a determining factor. Thus, it is more convenient to compare the number of particles with a given mass / mass equivalent size.

Increasing porosity results in a shift of the blowout towards smaller particles. This is contradictory to what is expected from the calculated  $\beta$  values (Fig. 5.25) where the size with  $\beta = 0.5$  is shifted to larger grains. However, the shape of the  $\beta$  ratio is flatter and therefore sizes with  $\beta = 1$  decrease with porosity. In the above definition for the blowout (see Chapter 2.4.1) as  $s_{\text{blowout}} = s(\beta = 0.5)$  it was assumed that the particle was released on a circular orbit. However, when considering eccentric orbits on which the particles are released, the blowout occurs somewhere between  $\beta = 0.5$  and  $1^5$ . In fact, some orbit geometries can even produce unbound trajectories for  $\beta < 0.5$  (for a short discussion see Wyatt 2006). Thus, it is not surprising that radiation pressure cannot remove smaller particles that were formerly absent.

The changes in the SED are dramatical: Emission is shifted to shorter wavelength and especially the maximum is narrowed. One reason is of course the overabundance of smaller particles that heat up the disk. However, when taking porosity into account, the comparison between size

<sup>5</sup>As up to now the  $\beta$  ratios were parallel between  $\beta = 0.5$  and 1 for all considered dust compositions, it was absolutely appropriate to define the blowout as  $s_{\text{blowout}} = s(\beta = 0.5)$ .

distribution and SED may be misleading. It is a well known feature for highly porous particles that their emission properties are rather independent of grain size and all objects behave like small grains, which can be considered as the components put together to the grain/aggregate (Kimura et al. 1997). Thus, the temperature range in the disk narrows at higher temperatures and therefore also the SED narrows at warmer emission. Seen from this perspective it is not a surprise that the SED does not significantly shift among the three porosity models — the small components determine the upper temperature in the disk and therefore the rise of the SED. In contrast, with increasing porosity even larger particles behave more and more like small motes, narrowing the temperature range and with it the SED.

Going to the radial profile of the optical depth, most significant changes occur in the outer part of the disk beyond the birth region where the slope flattens with increasing porosity. This part is dominated by small, barely bound particles (see Chapter 5.3.4). As compared to the Vega reference model, there is an overabundance of formerly blowout grains (in terms of the grain mass) that at the same time have a larger geometrical cross section. Thus, the total disk cross section and therefore the optical depth increases.

As implied by the optical depth, the radial surface brightness profiles flatten for all three *MIPS* wavelengths with increasing porosity. Furthermore, like in the SED, emission at 24 and 70  $\mu\text{m}$  is enhanced, while the 160  $\mu\text{m}$  profile drops.

**Preliminary Conclusions** can be drawn for the applicability of this approach to include porosity into the collisional way of modeling debris disks. Although placed in the context of the Vega disk investigations, this study was not intended to improve the fit found in Chapter 5.3.3, so that the changes with regards to the observations will not be discussed here. The idea was rather to check the overall impact of porosity on the modeling results. As can be clearly seen in Fig. 5.26 this impact is striking. Very efficiently the SED is shifted to shorter wavelengths and at the same time narrows significantly. However, this effect appears too extreme taking into account that the Vega SED is not exceptionally broad. Hence, this may imply that either the considered porosities here are too high, or the porosity model is oversimplified (or both).

Still, the results are not completely unrealistic. The famous system of HR 69830 may be an excellent application to highly porous dust: both SED and mid-IR spectrum are indicative of hot, small silicate dust, producing a very narrow excess between about 10 and 70  $\mu\text{m}$ . However, it is questionable, whether the collisional modeling approach with the assumption of a steady-state collisional cascade can hold for this extraordinary system. This will be subject to upcoming investigations.

## Chapter 6

# Conclusions

*The treasures hidden in the heavens are so rich that the human mind shall never be lacking in fresh nourishment.*

JOHANNES KEPLER

### 6.1 Summary

This work focused on modeling thermal emission of circumstellar debris disks. The disk constituents' wide range in size from very small dust grains up to planetesimals of hundreds of km makes this task especially challenging. What is more, observations are only sensitive to the dust's thermal emission while larger objects remain invisible. In turn typical dust lifetimes are relatively short meaning that small grains must steadily be replenished by planetesimals which can survive over much longer time scales. Therefore, the latter are more significant for the disks' longterm evolution. Several mechanisms are thinkable of how dust is produced. However, especially for all disks observed so far, mutual collisions between planetesimals are believed to be the leading process, justifying the name debris disks.

In the course of this work a new approach of modeling debris disks has been developed. It is based on simulating the disks collisional evolution. However, before introducing this, the classical way of modeling was summarized. The classical modeling approach concentrates on the dust portion to reproduce the observed emission. Therefore, analytical expressions, usually power-laws, are applied to describe the dust's spatial and grain size distributions. The most important model parameters are the slopes of the distributions, the inner and outer edge of the disk, the lower and upper size cutoff, and the dust mass.

This approach was applied to the planetary system HR 8799, which is one of the few systems, where dust emission and three planets, were detected. However, since this was part of a comprehensive study that also focused on planetary and planetesimal stability, no "naive" fit independent on the known (or rather presumed) parameters of the other system's components was performed. From the beginning constraints on the dust distribution from these components were taken into account. Therefore, as a first attempt, four arbitrary dust distributions with typical parameters were chosen with locations in accordance to stable regions for planetesimals towards planetary perturbations. The comparison of modeled and observed SED directly revealed that two components — a warm inner and a cold outer dust ring — are required to reproduce the warm emission as measured with *Spitzer/IRS* and the photometric data from the far-IR on. The most natural combination is to consider a very inner dust ring inside the innermost planet and a cold dust ring outside the outermost planet. Subsequent parameter variations indicate that dust in the inner part of the system can in its maximum extension lie between 2 and 15 AU, while in the outer part the location is less restricted. Reasonable outer edges were found out to 170 AU but also larger values are possible. The inner edge of the outer dust component could be varied between 70 and 120 AU. Dust masses of the inner and outer dust reservoirs are about  $1.4 \times 10^{-5} M_{\oplus}$  and  $4.2 \times 10^{-2} M_{\oplus}$ , respectively.

Complementary studies on the star, the planets, their dynamical stability, and finally the planetesimals' stability were performed. The stable zones for planetesimal evolution which were found in this work showed good agreement with the results of the SED modeling. Therefore, the derived ring locations can be considered as a robust statement for the system's architecture. Results from an analysis of resolved images of the HR 8799 disk, which were taken after this investigation was already completed, were in agreement with the findings of this study (Su et al. 2009).

The second, new modeling approach was developed in recent years, motivated by the progress in debris disk simulations. It is based on the code `ACE` that follows the collisional evolution of the whole disk, from planetesimals to dust. Taking the tools `SEDUCE` and `SUBITO`, thermal emission properties of the disk's dust portion can be calculated and compared to observations. The model parameters, which are all linked to certain physical effects and processes, can be adjusted so that in the end a good agreement between model and observations can be achieved. Although the fitting itself only concentrates on the disk's dust, `ACE` models the whole disk. It is therefore possible to “climb up” the ladder of the collisional cascade and also draw conclusions on the planetesimal population. Two examples were given to show the applicability of the new modeling approach.

First, a grid of reference disks around sun-like stars with locations from 3 to 200 AU were modeled. Given the possibility to follow the disk evolution on a Gyr timescale and to scale the results with the disk mass, the grid which was initially a one dimensional one becomes three dimensional. The final grid of reference disks can be transformed into a grid of reference SEDs that can be used to fit observed debris disk observations quickly. This was exemplified on five well observed G2 V debris disk systems. The fitting results imply the presence of large (100 – 200 AU) and massive ( $0.2 - 50 M_{\oplus}$ ) Kuiper belt analogs around all five stars with parameters (typical ring extensions and dust masses) close to those found in previous investigations. In particular, the *HST* image of HD 107146 shows a ring location close to the best disk model found here.

Second, an in-depth modeling of the archetypal system Vega was performed, aiming at reproducing the SED and the three surface brightness profiles observed with *Spitzer/MIPS*. This was motivated by claims of several authors stating that a standard steady-state collisional evolution is not capable of explaining the observed emission properties. A first-guess model already showed a surprisingly good agreement with the observed SED, however revealing some inconsistencies in the surface brightness profiles. Taking the first-guess model as a reference, various model parameters were modified, on the one hand checking the robustness of the reference model, on the other hand exploring the possibility of improving the agreement with the observations. All these models show disk masses of  $\sim 10 M_{\oplus}$  in objects  $\lesssim 100$  km.

In the end, a best fit was found by locating the planetesimal ring between 62 and 120 AU with eccentricities of up to 0.1. Besides that, the most important results are that the system must be relatively old (at least several tens of Myr) provided that the collisional cascade was operating over much of the Vega age. This is in agreement with the estimated stellar age of 350 Myr. Additionally, the luminosity, as seen from the disk, is supposed to lie between the nominal values for the pole and the equator. This can be seen as a natural consequence of the star's rapid rotation. Cratering collisions were discovered to be mandatory as well. From all that it could be concluded that the Vega observations can be explained with a steady-state standard disk model. In particular it was shown that especially the *Spitzer* images are not indicative of a mysterious overabundance of blowout grains, but rather uncover the question for the presence of an additional, unconstrained inner disk component.

Both applications of the new, collisional modeling approach have proven this method capable of providing reasonable results for observed debris disk systems. Advantages and disadvantages of this approach, but also of the classical way of modeling have already been discussed separately in Chapters 4.3 and 5.4. In the following section the pros and cons of the two approaches will be compared.

## 6.2 Comparison of the Two Approaches

One of the clear advantages of the new modeling approach is that it self-consistently includes the planetesimal population. In contrast, the classical method requires additional extrapolation

from the fitted dust distributions towards larger disk constituents. This is not only a difficult task in terms of the size distribution. Also the expected planetesimal locations are not necessarily identical to the found dust ring extensions (see typical size and spatial distributions in Chapter 5). Thus, comparisons between dust emission modeling and planetesimal stability analysis like in Chapters 4.2.4 and 4.2.5 can be very enlightening for deciphering the presumable architecture of a debris disk system.

Furthermore, all new model parameters in the collisional modeling are directly related to real, physical processes giving some insight into the mechanisms at work. In the classical way of modeling additional, subsequent interpretation is needed (see, e.g., discussion in Chapter 4.3 and application in Chapter 4.2). This has to be taken with caution, though, as conclusions may in some cases be misleading (see, e.g., the alternating views on the Vega system, Chapter 5.3).

In return, the computational efforts in the collisional approach are much more intense, making the whole method much more unhandy than the classical modeling. This holds all the more taking into account that for ACE simulations only initial conditions can be fixed but the evolution cannot be influenced in any direction. Thus, the expected accuracy of a fit cannot compete with those of the well optimized fitting algorithms based on the classical modeling approach.

One problem concerning both approaches is the degeneracy of model parameters. Especially power-law dust distributions provide several different parameters that change the resulting SED in a similar way. Thus, the importance of using as many observational data as possible is to stress. In particular resolved disk observations help to disentangle the spatial and grain size distribution effects. However, provided only few observations are available for a system to model, the classical modeling approach outmatches the new approach. This is true because complexity can easily be reduced. For example, the disk can be thought to be concentrated at a single, infinitesimally small ring. Particles may be of single size, or even blackbody particles can be considered. Such simplifications are unphysical and thus difficult to implement in the combination of the tools ACE and SEDUCE/SUBITO.

Concluding, it is to think about which approach is most promising for which application. As already mentioned several times, the classical way of modeling is a very fast method. Thus, it is the first choice to get first, quick estimates on some properties of an observed debris disk, like the dust mass or the probable dust location. Also, if just a limited set of observations is available, the classical approach with a decreased complexity is favored. The same holds for large number statistics of debris disks, which mostly combine both prerequisites: a quick method is needed to extract information of systems for which mostly only few data are available. However, if a system's SED is well covered and possibly also resolved observations are available, the new modeling approach is a good alternative. Especially if not only dust properties but also information about the planetesimal population and its evolution is sought, this method is the only reasonable possibility.

### 6.3 Outlook

Vital for good and reliable disk models is the quantity and quality of available observations. *Spitzer* has already revolutionized knowledge about debris disks. Similar effects are expected from the just started *Herschel* (full name: *Herschel Space Observatory*) mission. *Herschel*, with its instruments *HIFI* (*Heterodyne Instrument for the Far Infrared*, 157 – 625  $\mu\text{m}$ ), *PACS* (*Photodetector Array and Camera and Spectrometer*, 60 – 90  $\mu\text{m}$  / 90 – 130  $\mu\text{m}$  / 130 – 210  $\mu\text{m}$ ), and *SPIRE* (*Spectral and Photometric Imaging REceiver*, 250 / 350 / 500  $\mu\text{m}$ ) designed for photometry, spectroscopy, and imaging, is the most sensitive IR telescope to date, which will allow debris disk detections down to the level of a few Kuiper belts.

Two Open Time Key Programmes — *DUNES* (*DUst around NEarby Stars*, PI: C. Eiroa) and *DEBRIS* (*Disc Emission via a Bias-free Reconnaissance in the Infrared/Sub-millimetre*, PI: B.

Matthews) — deal with the analysis of already known and the detection of new debris disk systems. This implies two things. First, the new instruments cover very interesting wavelength regions. Typically, SEDs peak in the far-IR and start dropping in the sub-mm. Observations at these wavelengths are thus probing those particles that dominate the disks' optical depth. Unfortunately, the number of measurements longwards the far-IR was quite limited, as all huge surveys concentrated on shorter wavelengths. Thus, the SED coverage of many already known debris disk systems will improve. Furthermore, several objects are expected to be resolved at the different wavelengths in the far-IR and sub-mm. Estimation of a certain number is difficult. However, within the *DUNES* project 10 – 30% of the targets are believed to be resolvable (J. Rodmann, priv. comm.). This will allow application of the collisional modeling approach, as it was used for Vega (see Chapter 5.3), to other systems.

Another benefit of *Herschel's* unprecedented sensitivity is the possibility of far-IR spectroscopy at the level of the bright debris disk systems. Especially in the region around 70  $\mu\text{m}$  spectral features of water ice and several silicates are expected. Such spectroscopic observations will pose new constraints on the composition of debris disk dust and could therefore help reducing the tedious degeneracy in the modeling of these systems.

What is more, with *Herschel* the boundary towards transport-dominated disks (at least for small dust particles) will probably be penetrated. This will be a good opportunity to extend the new modeling approach and find a way to also model such objects with reasonable computational efforts.

Besides *Herschel*, also other new promising facilities are coming up soon or have just started operating recently:

- *SOFIA* (*Stratospheric Observatory for Infrared Astronomy*, 5 – 8  $\mu\text{m}$  / 17 – 25  $\mu\text{m}$  / 25 – 40  $\mu\text{m}$ ) is an airborne telescope designed for photometry onboard a Boeing 747-SP. It is the successor of *KAO* (*Kuiper Airborne Telescope*). In December 2009 the first test flight with completely opened telescope door was performed successfully. Basic science observations are planned for spring 2011.
- *SCUBA 2* (*Submillimetre Common-User Bolometer Array*, 450 and 850  $\mu\text{m}$ ) is a new camera for the *JCMT* at the Mauna Kea Observatory in Hawaii. Due to its huge field of view and quick read-out of the CCD-like detector it is designed for an all-sky survey (Matthews et al. 2007). Since late 2009 science observations can be performed.
- *ALMA* (*Atacama Large Millimeter/submillimeter Array*) is an interferometric array in the northern Chilean Atacama desert. It was initially planned with as much as 66 high-precision antennas of different size for observations in different wavelength bands in the sub-mm and millimeter. The first four antennas have already been installed and successfully tested. For completion it will take until 2012.

Thus, in the foreseeable future the agglomeration of observational data will have made it possible to model an appreciable set of debris disks with the new, collisional modeling approach. This provides the chance to draw first statistical conclusions on some model parameters that are yet rather unconstrained. For example, planetesimal properties (like typical masses, locations, and dynamical excitations) that were almost completely out of reach before will be in the field of investigation. Thus, similar findings like for the dust disk as presented in Chapter 1.2 may be possible.

The increasing number of modeling targets will finally prove the accuracy of the new modeling approach. It is therefore very likely that upcoming modeling efforts will reveal the necessity for different improvements in the approach. The area most in need of revision is the treatment of collisions. Currently, immense efforts are undertaken to overcome the limitations of laboratory and numerical investigations to provide more accurate and reliable collisional prescriptions, applicable for numerical tools like the ACE code (e.g., Stewart & Leinhardt 2009; Jutzi et al.

2010, 2009). The biggest problem here, however, is that the diversity of the collisional outcome is huge, depending on the assumed setup, which makes a simple prescription, as required for modeling a whole disk, very difficult.

With current models, it is already possible to constrain basic planetesimal properties, like their expected masses and typical eccentricities (Chapter 5). Furthermore, interaction between the disk and planets can to some extent be taken into account (Chapter 4.2). With the increasing number of modeling targets and improving modeling techniques, more properties will be subject to investigations, contributing to the understanding of planetesimal and planet formation. In particular, the initial sizes of planetesimals in the debris disk collisional evolution are of special interest, as it directly traces back to the formation scenarios at work, which are still under debate.

On a longer timescale, a combination of all phases of the disk evolution, starting from the disk sedimentation with the growth of dust aggregates, over the growth of planetesimals and planets, the disk dispersal, and finally the collisional debris disk evolution can be sought. Working mechanisms at different evolutionary stages are very different, implying the choice of different model approaches. It is immensely challenging to find a unified description covering all important processes. However, first steps have been taken to link single disk phases. Kenyon & Bromley (2008) for example were able to model the final assembly of terrestrial planets together with the collisional evolution of the associated debris disk. At even earlier disk stages, efforts are made to model the transitional state between primordial and debris disks by modeling the (gas) disk dispersal (e.g., Alexander & Armitage 2009; Owen et al. 2010) and interaction between the evolution of solids and a possible remaining gas fraction (Krivov et al. 2009). This however, is also just one step towards answering the original question of how earth has become what it is today and therefore where we come from.

# Bibliography

- Absil, O., et al. 2006, *Circumstellar material in the Vega inner system revealed by CHARA/FLUOR*, *Astronomy & Astrophysics*, 452, 237–244
- . 2008, *A near-infrared interferometric survey of debris disc stars. II. CHARA/FLUOR observations of six early-type dwarfs*, *Astronomy & Astrophysics*, 487, 1041–1054
- Adams, F. C., & Lin, D. N. C. 1993, *Transport processes and the evolution of disks*, in: *Protostars and Planets III*, ed. E. H. Levy & J. I. Lunine, 721–748
- Akeson, R. L., et al. 2009, *Dust in the inner regions of debris disks around a stars*, *The Astrophysical Journal*, 691, 1896–1908
- Alexander, R. 2008, *From discs to planetesimals: Evolution of gas and dust discs*, *New Astronomy Review*, 52, 60–77
- Alexander, R. D., & Armitage, P. J. 2009, *Giant Planet Migration, Disk Evolution, and the Origin of Transitional Disks*, *The Astrophysical Journal*, 704, 989–1001
- Alibert, Y., Mordasini, C., Benz, W., & Winisdoerffer, C. 2005, *Models of giant planet formation with migration and disc evolution*, *Astronomy & Astrophysics*, 434, 343–353
- Anandarao, B. G., & Vaidya, D. B. 1986, *The infrared excess of Alpha Lyrae*, *Astronomy & Astrophysics*, 161, L9–L11
- Arakawa, M. 1999, *Collisional Disruption of Ice by High-Velocity Impact*, *Icarus*, 142, 34–45
- Ardila, D. R., et al. 2004, *A Resolved Debris Disk around the G2 V Star HD 107146*, *The Astrophysical Journal Letters*, 617, L147–L150
- Armitage, P. J. 2010, *Astrophysics of Planet Formation* (Cambridge University Press)
- Artymowicz, P., Burrows, C., & Paresce, F. 1989, *The structure of the Beta Pictoris circumstellar disk from combined IRAS and coronagraphic observations*, *The Astrophysical Journal*, 337, 494–513
- Aufdenberg, J. P., et al. 2006, *First Results from the CHARA Array. VII. Long-Baseline Interferometric Measurements of Vega Consistent with a Pole-On, Rapidly Rotating Star*, *The Astrophysical Journal*, 645, 664–675
- Augereau, J.-C., & Beust, H. 2006, *On the AU Microscopii debris disk. Density profiles, grain properties, and dust dynamics*, *Astronomy & Astrophysics*, 455, 987–999
- Augereau, J. C., Lagrange, A. M., Mouillet, D., Papaloizou, J. C. B., & Grorod, P. A. 1999, *On the HR 4796 A circumstellar disk*, *Astronomy & Astrophysics*, 348, 557–569
- Augereau, J. C., Nelson, R. P., Lagrange, A. M., Papaloizou, J. C. B., & Mouillet, D. 2001, *Dynamical modeling of large scale asymmetries in the beta Pictoris dust disk*, *Astronomy & Astrophysics*, 370, 447–455
- Augereau, J.-C., et al. in prep., *PACS images of a Kuiper-like Belt around the planet-host star  $\rho$ 1 Eri analyzed with the DUNES modeling toolbox*, *Astronomy & Astrophysics*
- Aumann, H. H., et al. 1984, *Discovery of a shell around Alpha Lyrae*, *The Astrophysical Journal Letters*, 278, L23–L27
- Backman, D., et al. 2009, *Epsilon Eridani's Planetary Debris Disk: Structure and Dynamics Based on Spitzer and Caltech Submillimeter Observatory Observations*, *The Astrophysical Journal*, 690, 1522–1538
- Backman, D. E., & Paresce, F. 1993, *Main-sequence stars with circumstellar solid material - The VEGA phenomenon*, in: *Protostars and Planets III*, ed. E. H. Levy & J. I. Lunine, 1253–1304
- Becklin, E. E., & Neugebauer, G. 1967, *Observations of an Infrared Star in the Orion Nebula*, *The Astrophysical Journal*, 147, 799–803
- Begelman, M. C., McKee, C. F., & Shields, G. A. 1983, *Compton heated winds and coronae above accretion disks. I Dynamics*, *The Astrophysical Journal*, 271, 70–88
- Beichman, C. A., Neugebauer, G., Habing, H. J., Clegg, P. E., & Chester, T. J., eds. 1988, *Infrared astro-*



- nomical satellite (IRAS) catalogs and atlases. Volume 1: Explanatory supplement*, ed. C. A. Beichman, G. Neugebauer, H. J. Habing, P. E. Clegg, & T. J. Chester, Vol. 1
- Beichman, C. A., et al. 2005a, *An Excess Due to Small Grains around the Nearby K0 V Star HD 69830: Asteroid or Cometary Debris?*, *The Astrophysical Journal*, 626, 1061–1069
- . 2005b, *Planets and Infrared Excesses: Preliminary Results from a Spitzer MIPS Survey of Solar-Type Stars*, *The Astrophysical Journal*, 622, 1160–1170
- . 2006a, *IRS Spectra of Solar-Type Stars: A Search for Asteroid Belt Analogs*, *The Astrophysical Journal*, 639, 1166–1176
- . 2006b, *New Debris Disks around Nearby Main-Sequence Stars: Impact on the Direct Detection of Planets*, *The Astrophysical Journal*, 652, 1674–1693
- Benz, W., & Asphaug, E. 1999, *Catastrophic Disruptions Revisited*, *Icarus*, 142, 5–20
- Blum, J., & Wurm, G. 2008, *The Growth Mechanisms of Macroscopic Bodies in Protoplanetary Disks*, *Annual Review of Astronomy and Astrophysics*, 46, 21–56
- Bodenheimer, P., Hubickyj, O., & Lissauer, J. J. 2000, *Models of the in Situ Formation of Detected Extrasolar Giant Planets*, *Icarus*, 143, 2–14
- Bohren, C. F., & Huffman, D. R. 1983, *Absorption and scattering of light by small particles* (New York: Wiley, 1983)
- Bonnor, W. B. 1956, *Boyle's Law and gravitational instability*, *Monthly Notices of the Royal Astronomical Society*, 116, 351–359
- Booth, M., Wyatt, M. C., Morbidelli, A., Moro-Martín, A., & Levison, H. F. 2009, *The history of the Solar system's debris disc: observable properties of the Kuiper belt*, *Monthly Notices of the Royal Astronomical Society*, 399, 385–398
- Boss, A. P. 1997, *Giant planet formation by gravitational instability.*, *Science*, 276, 1836–1839
- Brauer, F., Dullemond, C. P., & Henning, T. 2008, *Coagulation, fragmentation and radial motion of solid particles in protoplanetary disks*, *Astronomy & Astrophysics*, 480, 859–877
- Brauer, F., Dullemond, C. P., Johansen, A., Henning, T., Klahr, H., & Natta, A. 2007, *Survival of the mm-cm size grain population observed in protoplanetary disks*, *Astronomy & Astrophysics*, 469, 1169–1182
- Britt, D. T., Yeomans, D., Housen, K., & Consolmagno, G. 2002, *Asteroid Density, Porosity, and Structure*, in: *Asteroids III*, ed. W. F. Bottke, A. Cellino, P. Paolicchi, & R. Binzel, 485–500
- Brown, M. E. 2001, *The Inclination Distribution of the Kuiper Belt*, *The Astronomical Journal*, 121, 2804–2814
- Bryden, G., et al. 2006, *Frequency of Debris Disks around Solar-Type Stars: First Results from a Spitzer MIPS Survey*, *The Astrophysical Journal*, 636, 1098–1113
- . 2009, *Planets and Debris Disks: Results from a Spitzer/MIPS Search for Infrared Excess*, *The Astrophysical Journal*, 705, 1226–1236
- Buitrago, J., & Mediavilla, E. 1985, *Dynamics of the dust material surrounding VEGA*, *Astronomy & Astrophysics*, 148, L8–L10
- . 1986, *Inversion equation for the study of circumstellar dust shells - Application to Beta Pictoris*, *Astronomy & Astrophysics*, 162, 95–98
- Burns, J. A., Lamy, P. L., & Soter, S. 1979, *Radiation forces on small particles in the solar system*, *Icarus*, 40, 1–48
- Cameron, A. G. W. 1978, *Physics of the primitive solar accretion disk*, *Moon and Planets*, 18, 5–40
- Campbell, B., Walker, G. A. H., & Yang, S. 1988, *A search for substellar companions to solar-type stars*, *The Astrophysical Journal*, 331, 902–921
- Campo Bagatin, A., Cellino, A., Davis, D. R., Farinella, P., & Paolicchi, P. 1994, *Wavy size distributions for collisional systems with a small-size cutoff*, *Planetary and Space Science*, 42, 1079–1092

- Carpenter, J. M., Wolf, S., Schreyer, K., Launhardt, R., & Henning, T. 2005, *Evolution of Cold Circumstellar Dust around Solar-type Stars*, *The Astronomical Journal*, 129, 1049–1062
- Carpenter, J. M., et al. 2009, *Formation and Evolution of Planetary Systems: Properties of Debris Dust Around Solar-Type Stars*, *The Astrophysical Journal Supplement*, 181, 197–226
- Chambers, J. 2008, *Oligarchic growth with migration and fragmentation*, *Icarus*, 198, 256–273
- Chambers, J. E. 2006, *Planet Formation with Migration*, *The Astrophysical Journal Letters*, 652, L133–L136
- Chambers, J. E., & Wetherill, G. W. 1998, *Making the Terrestrial Planets: N-Body Integrations of Planetary Embryos in Three Dimensions*, *Icarus*, 136, 304–327
- Chapman, C. R., Merline, W. J., & Thomas, P. 1999, *Cratering on Mathilde*, *Icarus*, 140, 28–33
- Chen, C. H., Fitzgerald, M. P., & Smith, P. S. 2008, *A Possible Icy Kuiper Belt around HD 181327*, *The Astrophysical Journal*, 689, 539–544
- Chen, C. H., et al. 2006, *Spitzer IRS Spectroscopy of IRAS-discovered Debris Disks*, *The Astrophysical Journal Supplement*, 166, 351–377
- Chiang, E. 2008, *Vertical Shearing Instabilities in Radially Shearing Disks: The Dustiest Layers of the Protoplanetary Nebula*, *The Astrophysical Journal*, 675, 1549–1558
- Chiang, E., Kite, E., Kalas, P., Graham, J. R., & Clampin, M. 2009, *Fomalhaut's Debris Disk and Planet: Constraining the Mass of Fomalhaut b from disk Morphology*, *The Astrophysical Journal*, 693, 734–749
- Chini, R., Kruegel, E., & Kreysa, E. 1990, *Large dust particles around main sequence stars*, *Astronomy & Astrophysics*, 227, L5–L8
- Cieza, L. A., et al. 2010, *The Nature of Transition Circumstellar Disks. I. The Ophiuchus Molecular Cloud*, *The Astrophysical Journal*, 712, 925–941
- Clarke, C. J., Gendrin, A., & Sotomayor, M. 2001, *The dispersal of circumstellar discs: the role of the ultraviolet switch*, *Monthly Notices of the Royal Astronomical Society*, 328, 485–491
- Close, L. M., & Males, J. R. 2010, *A Search for Wide Companions to the Extrasolar Planetary System HR 8799*, *The Astrophysical Journal*, 709, 342–348
- Consolmagno, G. J., Britt, D. T., & Stoll, C. P. 1998, *The porosities of ordinary chondrites: Models and interpretation*, *Meteoritics and Planetary Science*, 33, 1221–1229
- Currie, T. 2010, *The Morphologies and Lifetimes of Transitional Protoplanetary Disks*, ArXiv e-prints
- Currie, T., & Kenyon, S. J. 2009, *Deep MIPS Observations of the IC 348 Nebula: Constraints on the Evolutionary State of Anemic Circumstellar Disks and the Primordial-to-Debris Disk Transition*, *The Astronomical Journal*, 138, 703–726
- Cuzzi, J. N., Dobrovolskis, A. R., & Champney, J. M. 1993, *Particle-gas dynamics in the midplane of a protoplanetary nebula*, *Icarus*, 106, 102–134
- Czechowski, A., & Mann, I. 2010, *Formation and Acceleration of Nano Dust in the Inner Heliosphere*, *The Astrophysical Journal*, 714, 89–99
- D'Angelo, G., Lubow, S. H., & Bate, M. R. 2006, *Evolution of Giant Planets in Eccentric Disks*, *The Astrophysical Journal*, 652, 1698–1714
- Davison, T. M., Collins, G. S., & Ciesla, F. J. 2010, *Numerical modelling of heating in porous planetesimal collisions*, *Icarus*, 208, 468–481
- Dent, W. R. F., Walker, H. J., Holland, W. S., & Greaves, J. S. 2000, *Models of the dust structures around Vega-excess stars*, *Monthly Notices of the Royal Astronomical Society*, 314, 702–712
- Di Folco, E., Thévenin, F., Kervella, P., Domiciano de Souza, A., Coudé du Foresto, V., Ségransan, D., & Morel, P. 2004, *VLT/IR interferometric observations of Vega-like stars. Radius and age of  $\alpha$  PsA,  $\beta$  Leo,  $\beta$  Pic,  $\epsilon$  Eri and  $\tau$  Cet*, *Astronomy & Astrophysics*, 426, 601–617
- di Folco, E., et al. 2007, *A near-infrared interferometric survey of debris disk stars. I. Probing the hot dust content around  $\epsilon$  Eridani and  $\tau$  Ceti with CHARA/FLUOR*, *Astronomy & Astrophysics*, 475, 243–250

- Divine, N., et al. 1986, *The Comet Halley dust and gas environment*, Space Science Reviews, 43, 1–104
- Dohnanyi, J. W. 1969, *Collisional models of asteroids and their debris*, Journal of Geographic Research, 74, 2531–2554
- Dominik, C., & Decin, G. 2003, *Age Dependence of the Vega Phenomenon: Theory*, The Astrophysical Journal, 598, 626–635
- Draine, B. T. 1985, *Tabulated optical properties of graphite and silicate grains*, The Astrophysical Journal Supplement, 57, 587–594
- . 2003a, *Scattering by Interstellar Dust Grains. I. Optical and Ultraviolet*, The Astrophysical Journal, 598, 1017–1025
- . 2003b, *Scattering by Interstellar Dust Grains. II. X-Rays*, The Astrophysical Journal, 598, 1026–1037
- Draine, B. T., & Lee, H. M. 1984, *Optical properties of interstellar graphite and silicate grains*, The Astrophysical Journal, 285, 89–108
- Duffard, R., Ortiz, J. L., Thirouin, A., Santos-Sanz, P., & Morales, N. 2009, *Transneptunian objects and Centaurs from light curves*, Astronomy & Astrophysics, 505, 1283–1295
- Dullemond, C. P., & Dominik, C. 2005, *Dust coagulation in protoplanetary disks: A rapid depletion of small grains*, Astronomy & Astrophysics, 434, 971–986
- Durda, D. D., & Dermott, S. F. 1997, *The Collisional Evolution of the Asteroid Belt and Its Contribution to the Zodiacal Cloud*, Icarus, 130, 140–164
- Faber, P., & Quillen, A. C. 2007, *The total number of giant planets in debris discs with central clearings*, Monthly Notices of the Royal Astronomical Society, 382, 1823–1828
- Fabrycky, D. C., & Murray-Clay, R. A. 2010, *Stability of the Directly Imaged Multiplanet System HR 8799: Resonance and Masses*, The Astrophysical Journal, 710, 1408–1421
- Fernandez, J. A., & Ip, W. 1984, *Some dynamical aspects of the accretion of Uranus and Neptune - The exchange of orbital angular momentum with planetesimals*, Icarus, 58, 109–120
- Font, A. S., McCarthy, I. G., Johnstone, D., & Ballantyne, D. R. 2004, *Photoevaporation of Circumstellar Disks around Young Stars*, The Astrophysical Journal, 607, 890–903
- Freistetter, F., Krivov, A. V., & Löhne, T. 2007, *Planets of  $\beta$  Pictoris revisited*, Astronomy & Astrophysics, 466, 389–393
- Fujii, Y., & Nakamura, A. M. 2009, *Compaction and fragmentation of porous gypsum targets from low-velocity impacts*, Icarus, 201, 795–801
- Fujiwara, A. 1986, *Results obtained by laboratory simulations of catastrophic impact*, Mem. Soc. Astron. Ital., 57, 47–64
- Fujiwara, A., Kamimoto, G., & Tsukamoto, A. 1977, *Destruction of basaltic bodies by high-velocity impact*, Icarus, 31, 277–288
- Fukagawa, M., Itoh, Y., Tamura, M., Oasa, Y., Hayashi, S. S., Fujita, Y., Shibai, H., & Hayashi, M. 2009, *H-Band Image of a Planetary Companion Around HR 8799 in 2002*, The Astrophysical Journal Letters, 696, L1–L5
- Gaidos, E., & Koresko, C. 2004, *A survey of 10- $\mu$ m silicate emission from dust around young sun-like stars*, New Astronomy, 9, 33–42
- Gautier, III, T. N., et al. 2007, *Far-Infrared Properties of M Dwarfs*, The Astrophysical Journal, 667, 527–536
- Gladman, B., Kavelaars, J. J., Petit, J., Morbidelli, A., Holman, M. J., & Loredó, T. 2001, *The Structure of the Kuiper Belt: Size Distribution and Radial Extent*, The Astronomical Journal, 122, 1051–1066
- Goldreich, P., & Ward, W. R. 1973, *The Formation of Planetesimals*, The Astrophysical Journal, 183, 1051–1062
- Gomes, R., Levison, H. F., Tsiganis, K., & Morbidelli, A. 2005, *Origin of the cataclysmic Late Heavy Bombardment period of the terrestrial planets*, Nature, 435, 466–469

- Gomes, R. S., Morbidelli, A., & Levison, H. F. 2004, *Planetary migration in a planetesimal disk: why did Neptune stop at 30 AU?*, *Icarus*, 170, 492–507
- Gorlova, N., Balog, Z., Rieke, G. H., Muzerolle, J., Su, K. Y. L., Ivanov, V. D., & Young, E. T. 2007, *Debris Disks in NGC 2547*, *The Astrophysical Journal*, 670, 516–535
- Goździewski, K., & Migaszewski, C. 2009, *Is the HR8799 extrasolar system destined for planetary scattering?*, *Monthly Notices of the Royal Astronomical Society*, 397, L16–L20
- Greaves, J. S. 2005, *Disks Around Stars and the Growth of Planetary Systems*, *Science*, 307, 68–71
- Greaves, J. S., Fischer, D. A., & Wyatt, M. C. 2006, *Metallicity, debris discs and planets*, *Monthly Notices of the Royal Astronomical Society*, 366, 283–286
- Greaves, J. S., Holland, W. S., Jayawardhana, R., Wyatt, M. C., & Dent, W. R. F. 2004, *A search for debris discs around stars with giant planets*, *Monthly Notices of the Royal Astronomical Society*, 348, 1097–1104
- Greaves, J. S., & Wyatt, M. C. 2003, *Some anomalies in the occurrence of debris discs around main-sequence A and G stars*, *Monthly Notices of the Royal Astronomical Society*, 345, 1212–1222
- Greaves, J. S., et al. 2005, *Structure in the  $\epsilon$  Eridani Debris Disk*, *The Astrophysical Journal Letters*, 619, L187–L190
- Grigorieva, A., Artymowicz, P., & Thébault, P. 2007, *Collisional dust avalanches in debris discs*, *Astronomy & Astrophysics*, 461, 537–549
- Grün, E., Zook, H. A., Fechtig, H., & Giese, R. H. 1985, *Collisional balance of the meteoritic complex*, *Icarus*, 62, 244–272
- Hage, J. I., & Greenberg, J. M. 1990, *A model for the optical properties of porous grains*, *The Astrophysical Journal*, 361, 251–259
- Hahn, J. M., & Malhotra, R. 2005, *Neptune’s Migration into a Stirred-Up Kuiper Belt: A Detailed Comparison of Simulations to Observations*, *The Astronomical Journal*, 130, 2392–2414
- Harker, D. E., Woodward, C. E., & Wooden, D. H. 2005, *The Dust Grains from 9P/Tempel 1 Before and After the Encounter with Deep Impact*, *Science*, 310, 278–280
- Harper, D. A., Loewenstein, R. F., & Davidson, J. A. 1984, *On the nature of the material surrounding VEGA*, *The Astrophysical Journal*, 285, 808–812
- Harvey, P. M., Wilking, B. A., & Joy, M. 1984, *On the far-infrared excess of VEGA*, *Nature*, 307, 441–442
- Hauschildt, P. H., Allard, F., & Baron, E. 1999, *The NextGen Model Atmosphere Grid for  $3000 \leq T_{\text{eff}} \leq 10,000$  K*, *The Astrophysical Journal*, 512, 377–385
- Hayashi, C., Nakazawa, K., & Nakagawa, Y. 1985, *Formation of the solar system*, in: *Protostars and Planets II*, ed. D. C. Black & M. S. Matthews, 1100–1153
- Heinrichsen, I., Walker, H. J., & Klaas, U. 1998, *Infrared mapping of the dust disc around VEGA*, *Monthly Notices of the Royal Astronomical Society*, 293, L78–L82
- Helou, G., & Walker, D. W. 1988, *Infrared Astronomical Satellite (IRAS), Catalogs and Atlases. Vol. 7. The Small Scale Structure Catalog.*, in: *NASA RP-1190, Vol. 7 (1988)*, 0–+
- Hildebrand, R., & Kirby, L. 2004, *Polarization of FIR/Sub-mm Dust Emission*, in: *Astronomical Society of the Pacific Conference Series, Vol. 309, Astrophysics of Dust*, ed. A. N. Witt, G. C. Clayton, & B. T. Draine, 515–527
- Hildebrand, R. H. 1983, *The Determination of Cloud Masses and Dust Characteristics from Submillimetre Thermal Emission*, *Quarterly Journal of the Royal Astronomical Society*, 24, 267–282
- Hillenbrand, L. A., et al. 2008, *The Complete Census of 70  $\mu\text{m}$ -bright Debris Disks within “the Formation and Evolution of Planetary Systems” Spitzer Legacy Survey of Sun-like Stars*, *The Astrophysical Journal*, 677, 630–656
- Holland, W. S., et al. 1998, *Submillimetre images of dusty debris around nearby stars*, *Nature*, 392, 788–791

- Hollenbach, D., Johnstone, D., Lizano, S., & Shu, F. 1994, *Photoevaporation of disks around massive stars and application to ultracompact H II regions*, *The Astrophysical Journal*, 428, 654–669
- Honda, M., et al. 2004, *Crystalline Silicate Feature of the Vega-like Star HD 145263*, *The Astrophysical Journal Letters*, 610, L49–L52
- Horányi, M. 1996, *Charged Dust Dynamics in the Solar System*, *Annual Review of Astronomy and Astrophysics*, 34, 383–418
- Housen, K. R., Holsapple, K. A., & Voss, M. E. 1999, *Compaction as the origin of the unusual craters on the asteroid Mathilde*, *Nature*, 402, 155–157
- Hubickyj, O., Bodenheimer, P., & Lissauer, J. J. 2005, *Accretion of the gaseous envelope of Jupiter around a 5–10 Earth-mass core*, *Icarus*, 179, 415–431
- Ida, S., & Makino, J. 1993, *Scattering of planetesimals by a protoplanet - Slowing down of runaway growth*, *Icarus*, 106, 210–227
- Jewitt, D. 2004, *Looking through the HIPPO: Nucleus and Dust in Comet 2P/Encke*, *The Astronomical Journal*, 128, 3061–3069
- Johansen, A., Oishi, J. S., Low, M., Klahr, H., Henning, T., & Youdin, A. 2007, *Rapid planetesimal formation in turbulent circumstellar disks*, *Nature*, 448, 1022–1025
- Jones, T. J., Stark, D., Woodward, C. E., Kelley, M. S., Kolokolova, L., Clemens, D., & Pinnick, A. 2008, *Evidence of Fragmenting Dust Particles from Near-Simultaneous Optical and Near-Infrared Photometry and Polarimetry of Comet 73P/SCHWASSMANN-WACHMANN 3*, *The Astronomical Journal*, 135, 1318–1327
- Jura, M., et al. 2004, *Mid-Infrared Spectra of Dust Debris around Main-Sequence Stars*, *The Astrophysical Journal Supplement*, 154, 453–457
- Jutzi, M., Benz, W., & Michel, P. 2008, *Numerical simulations of impacts involving porous bodies. I. Implementing sub-resolution porosity in a 3D SPH hydrocode*, *Icarus*, 198, 242–255
- Jutzi, M., Michel, P., Benz, W., & Richardson, D. C. 2010, *Fragment properties at the catastrophic disruption threshold: The effect of the parent body's internal structure*, *Icarus*, 207, 54–65
- Jutzi, M., Michel, P., Hiraoka, K., Nakamura, A. M., & Benz, W. 2009, *Numerical simulations of impacts involving porous bodies. II. Comparison with laboratory experiments*, *Icarus*, 201, 802–813
- Kalas, P., & Jewitt, D. 1995, *Asymmetries in the Beta Pictoris Dust Disk*, *The Astronomical Journal*, 110, 794–804
- Kalas, P., et al. 2008, *Optical Images of an Exosolar Planet 25 Light-Years from Earth*, *Science*, 322, 1345–1348
- Kenyon, S. J., & Bromley, B. C. 2001, *Gravitational Stirring in Planetary Debris Disks*, *The Astronomical Journal*, 121, 538–551
- . 2004a, *Collisional Cascades in Planetesimal Disks. II. Embedded Planets*, *The Astronomical Journal*, 127, 513–530
- . 2004b, *Detecting the Dusty Debris of Terrestrial Planet Formation*, *The Astrophysical Journal Letters*, 602, L133–L136
- . 2005, *Prospects for Detection of Catastrophic Collisions in Debris Disks*, *The Astronomical Journal*, 130, 269–279
- . 2006, *Terrestrial Planet Formation. I. The Transition from Oligarchic Growth to Chaotic Growth*, *The Astronomical Journal*, 131, 1837–1850
- . 2008, *Variations on Debris Disks: Icy Planet Formation at 30–150 AU for 1–3  $M_{\text{Solar}}$  Main-Sequence Stars*, *The Astrophysical Journal Supplement*, 179, 451–483
- . 2010, *Variations on Debris Disks. II. Icy Planet Formation as a Function of the Bulk Properties and Initial Sizes of Planetesimals*, *The Astrophysical Journal Supplement*, 188, 242–279
- Kenyon, S. J., & Luu, J. X. 1999a, *Accretion in the Early Kuiper Belt. II. Fragmentation*, *The Astronomical*

- Journal, 118, 1101–1119
- . 1999b, *Accretion in the Early Outer Solar System*, The Astrophysical Journal, 526, 465–470
- Kim, J. S., et al. 2005, *Formation and Evolution of Planetary Systems: Cold Outer Disks Associated with Sun-like Stars*, The Astrophysical Journal, 632, 659–669
- Kimura, H., Ishimoto, H., & Mukai, T. 1997, *A study on solar dust ring formation based on fractal dust models*, Astronomy & Astrophysics, 326, 263–270
- Kimura, H., & Mann, I. 1998, *The Electric Charging of Interstellar Dust in the Solar System and Consequences for Its Dynamics*, The Astrophysical Journal, 499, 454–462
- Kimura, H., Okamoto, H., & Mukai, T. 2002, *Radiation Pressure and the Poynting-Robertson Effect for Fluffy Dust Particles*, Icarus, 157, 349–361
- Koerner, D. W., Sargent, A. I., & Ostroff, N. A. 2001, *Millimeter-Wave Aperture Synthesis Imaging of Vega: Evidence for a Ring Arc at 95 AU*, The Astrophysical Journal Letters, 560, L181–L184
- Koike, C., Chihara, H., Tsuchiyama, A., Suto, H., Sogawa, H., & Okuda, H. 2003, *Compositional dependence of infrared absorption spectra of crystalline silicate. II. Natural and synthetic olivines*, Astronomy & Astrophysics, 399, 1101–1107
- Kokubo, E., & Ida, S. 1996, *On Runaway Growth of Planetesimals*, Icarus, 123, 180–191
- Kolokolova, L., & Gustafson, B. A. S. 2001, *Scattering by inhomogeneous particles: microwave analog experiments and comparison to effective medium theories*, Journal of Quantitative Spectroscopy and Radiative Transfer, 70, 611–625
- Kóspál, Á., Ardila, D. R., Moór, A., & Ábrahám, P. 2009, *On the Relationship Between Debris Disks and Planets*, The Astrophysical Journal Letters, 700, L73–L77
- Krivov, A. V. 2010, *Debris disks: seeing dust, thinking of planetesimals and planets*, Research in Astronomy and Astrophysics, 10, 383–414
- Krivov, A. V., Herrmann, F., Brandeker, A., & Thébault, P. 2009, *Can gas in young debris disks be constrained by their radial brightness profiles?*, Astronomy & Astrophysics, 507, 1503–1516
- Krivov, A. V., Löhne, T., & Sremčević, M. 2006, *Dust distributions in debris disks: effects of gravity, radiation pressure and collisions*, Astronomy & Astrophysics, 455, 509–519
- Krivov, A. V., Mann, I., & Krivova, N. A. 2000, *Size distributions of dust in circumstellar debris discs*, Astronomy & Astrophysics, 362, 1127–1137
- Krivov, A. V., Müller, S., Löhne, T., & Mutschke, H. 2008, *Collisional and Thermal Emission Models of Debris Disks: Toward Planetesimal Population Properties*, The Astrophysical Journal, 687, 608–622
- Krivov, A. V., Queck, M., Löhne, T., & Sremčević, M. 2007, *On the nature of clumps in debris disks*, Astronomy & Astrophysics, 462, 199–210
- Krivov, A. V., Sremčević, M., & Spahn, F. 2005, *Evolution of a Keplerian disk of colliding and fragmenting particles: a kinetic model with application to the Edgeworth-Kuiper belt*, Icarus, 174, 105–134
- Krivova, N. A., Krivov, A. V., & Mann, I. 2000, *The Disk of  $\beta$  Pictoris in the Light of Polarimetric Data*, The Astrophysical Journal, 539, 424–434
- Kuchner, M. J., & Stark, C. C. 2010, *Collisional Grooming Models of the Kuiper Belt Dust Cloud*, The Astronomical Journal, 140, 1007–1019
- Lada, E. A. 1992, *Global star formation in the L1630 molecular cloud*, The Astrophysical Journal Letters, 393, L25–L28
- Lafrenière, D., Marois, C., Doyon, R., & Barman, T. 2009, *HST/NICMOS Detection of HR 8799 b in 1998*, The Astrophysical Journal Letters, 694, L148–L152
- Lamy, P. L., Gruen, E., & Perrin, J. M. 1987, *Comet P/Halley - Implications of the mass distribution function for the photopolarimetric properties of the dust coma*, Astronomy & Astrophysics, 187, 767–773
- Laor, A., & Draine, B. T. 1993, *Spectroscopic constraints on the properties of dust in active galactic*

- nuclei*, *The Astrophysical Journal*, 402, 441–468
- Larson, R. B. 1969, *Numerical calculations of the dynamics of collapsing proto-star*, *Monthly Notices of the Royal Astronomical Society*, 145, 271–295
- . 1981, *Turbulence and star formation in molecular clouds*, *Monthly Notices of the Royal Astronomical Society*, 194, 809–826
- Lawler, S. M., et al. 2009, *Explorations Beyond the Snow Line: Spitzer/IRS Spectra of Debris Disks Around Solar-type Stars*, *The Astrophysical Journal*, 705, 89–111
- Leinert, C., & Grün, E. 1990, *Interplanetary Dust*, in: *Physics of the Inner Heliosphere I*, 207–275
- Lestrade, J., Wyatt, M. C., Bertoldi, F., Dent, W. R. F., & Menten, K. M. 2006, *Search for cold debris disks around M-dwarfs*, *Astronomy & Astrophysics*, 460, 733–741
- Lestrade, J., Wyatt, M. C., Bertoldi, F., Menten, K. M., & Lahaigt, G. 2009, *Search for cold debris disks around M-dwarfs. II*, *Astronomy & Astrophysics*, 506, 1455–1467
- Lin, D. N. C., & Papaloizou, J. 1986, *On the tidal interaction between protoplanets and the protoplanetary disk. III - Orbital migration of protoplanets*, *The Astrophysical Journal*, 309, 846–857
- Lisse, C. M., Beichman, C. A., Bryden, G., & Wyatt, M. C. 2007, *On the Nature of the Dust in the Debris Disk around HD 69830*, *The Astrophysical Journal*, 658, 584–592
- Lisse, C. M., Chen, C. H., Wyatt, M. C., & Morlok, A. 2008a, *Circumstellar Dust Created by Terrestrial Planet Formation in HD 113766*, *The Astrophysical Journal*, 673, 1106–1122
- Lisse, C. M., Chen, C. H., Wyatt, M. C., & Morlok, A. 2008b, *Star System HD172555 - Spectral Evidence of Abundant Silica Created by a Massive In-System Collision?*, in: *Lunar and Planetary Institute Science Conference Abstracts*, Vol. 39, *Lunar and Planetary Institute Science Conference Abstracts*, 2119
- Lisse, C. M., Chen, C. H., Wyatt, M. C., Morlok, A., Song, I., Bryden, G., & Sheehan, P. 2009, *Abundant Circumstellar Silica Dust and SiO Gas Created by a Giant Hypervelocity Collision in the ~ 12 Myr HD172555 System.*, *The Astrophysical Journal*, 701, 2019–2032
- Liu, M. C., Matthews, B. C., Williams, J. P., & Kalas, P. G. 2004, *A Submillimeter Search of Nearby Young Stars for Cold Dust: Discovery of Debris Disks around Two Low-Mass Stars*, *The Astrophysical Journal*, 608, 526–532
- Löhne, T. 2008, *Models of Rotationally Symmetric, Collision-Dominated Debris Discs*, PhD thesis, Friedrich Schiller Universität Jena, Jena, Germany
- Löhne, T., Krivov, A. V., & Rodmann, J. 2008, *Long-Term Collisional Evolution of Debris Disks*, *The Astrophysical Journal*, 673, 1123–1137
- Love, S. G., Hörz, F., & Brownlee, D. E. 1993, *Target Porosity Effects in Impact Cratering and Collisional Disruption*, *Icarus*, 105, 216–224
- Lynch, D. W., & Hunter, W. R. 1991, *Optical constants of metals*, in: *Handbook of Optical Constants of Solids II*, ed. E. D. Palik (San Diego, CA: Academic Press), 385
- Makarov, V. V., Gaume, R. A., & Andrievsky, S. M. 2005, *Expansion of the TW Hydrae association and the encounter with Vega*, *Monthly Notices of the Royal Astronomical Society*, 362, 1109–1113
- Malfait, K., Waelkens, C., Waters, L. B. F. M., Vandenbussche, B., Huygen, E., & de Graauw, M. S. 1998, *The spectrum of the young star HD 100546 observed with the Infrared Space Observatory*, *Astronomy & Astrophysics*, 332, L25–L28
- Marois, C., Macintosh, B., Barman, T., Zuckerman, B., Song, I., Patience, J., Lafrenière, D., & Doyon, R. 2008, *Direct Imaging of Multiple Planets Orbiting the Star HR 8799*, *Science*, 322, 1348–1352
- Marsh, K. A., Dowell, C. D., Velusamy, T., Grogan, K., & Beichman, C. A. 2006, *Images of the Vega Dust Ring at 350 and 450  $\mu\text{m}$ : New Clues to the Trapping of Multiple-Sized Dust Particles in Planetary Resonances*, *The Astrophysical Journal Letters*, 646, L77–L80
- Martin, P. G. 1973, *Interstellar Circular Polarization and the Composition of Interstellar Dust*, in: *IAU Symposium*, Vol. 52, *Interstellar Dust and Related Topics*, ed. J. M. Greenberg & H. C. van de Hulst, 161–167

- Matthews, B. C., et al. 2007, *An Unbiased Survey of 500 Nearby Stars for Debris Disks: A JCMT Legacy Program*, Publications of the Astronomical Society of the Pacific, 119, 842–854
- Mayor, M., & Queloz, D. 1995, *A Jupiter-mass companion to a solar-type star*, Nature, 378, 355–359
- McKee, C. F., & Ostriker, E. C. 2007, *Theory of Star Formation*, Annual Review of Astronomy and Astrophysics, 45, 565–687
- Meeus, G., Waters, L. B. F. M., Bouwman, J., van den Ancker, M. E., Waelkens, C., & Malfait, K. 2001, *ISO spectroscopy of circumstellar dust in 14 Herbig Ae/Be systems: Towards an understanding of dust processing*, Astronomy & Astrophysics, 365, 476–490
- Meyer, M. R., et al. 2004, *The Formation and Evolution of Planetary Systems: First Results from a Spitzer Legacy Science Program*, The Astrophysical Journal Supplement, 154, 422–427
- . 2006, *The Formation and Evolution of Planetary Systems: Placing Our Solar System in Context with Spitzer*, Publications of the Astronomical Society of the Pacific, 118, 1690–1710
- . 2008, *Evolution of Mid-Infrared Excess around Sun-like Stars: Constraints on Models of Terrestrial Planet Formation*, The Astrophysical Journal Letters, 673, L181–L184
- Minato, T., Köhler, M., Kimura, H., Mann, I., & Yamamoto, T. 2006, *Momentum transfer to fluffy dust aggregates from stellar winds*, Astronomy & Astrophysics, 452, 701–707
- Mizuno, H. 1980, *Formation of the Giant Planets*, Progress of Theoretical Physics, 64, 544–557
- Molster, F. J., Waters, L. B. F. M., Tielens, A. G. G. M., Koike, C., & Chihara, H. 2002, *Crystalline silicate dust around evolved stars. III. A correlations study of crystalline silicate features*, Astronomy & Astrophysics, 382, 241–255
- Moór, A., Ábrahám, P., Derekas, A., Kiss, C., Kiss, L. L., Apai, D., Grady, C., & Henning, T. 2006, *Nearby Debris Disk Systems with High Fractional Luminosity Reconsidered*, The Astrophysical Journal, 644, 525–542
- Morbidelli, A., Bottke, W. F., Nesvorný, D., & Levison, H. F. 2009, *Asteroids were born big*, Icarus, 204, 558–573
- Moro-Martín, A., & Malhotra, R. 2003, *Dynamical Models of Kuiper Belt Dust in the Inner and Outer Solar System*, The Astronomical Journal, 125, 2255–2265
- Moro-Martín, A., Wolf, S., & Malhotra, R. 2005, *Signatures of Planets in Spatially Unresolved Debris Disks*, The Astrophysical Journal, 621, 1079–1097
- Moro-Martín, A., et al. 2007, *Are Debris Disks and Massive Planets Correlated?*, The Astrophysical Journal, 658, 1312–1321
- Moshir, M., et al. 1990, *The IRAS Faint Source Catalog, Version 2*, in: *Bulletin of the American Astronomical Society*, Vol. 22, 1325
- Mouillet, D., Larwood, J. D., Papaloizou, J. C. B., & Lagrange, A. M. 1997, *A planet on an inclined orbit as an explanation of the warp in the Beta Pictoris disc*, Monthly Notices of the Royal Astronomical Society, 292, 896–904
- Mukai, T., Ishimoto, H., Kozasa, T., Blum, J., & Greenberg, J. M. 1992, *Radiation pressure forces of fluffy porous grains*, Astronomy & Astrophysics, 262, 315–320
- Mukai, T., & Yamamoto, T. 1982, *Solar wind pressure on interplanetary dust*, Astronomy & Astrophysics, 107, 97–100
- Müller, S. 2007, *Berechnung photometrischer Eigenschaften von zirkumstellaren Trümmerscheiben*, Diplomarbeit, Friedrich-Schiller Universität Jena, Germany
- Müller, S., Löhne, T., & Krivov, A. V. 2010, *The Debris Disk of Vega: A Steady-state Collisional Cascade, Naturally*, The Astrophysical Journal, 708, 1728–1747
- Mustill, A. J., & Wyatt, M. C. 2009, *Debris disc stirring by secular perturbations from giant planets*, Monthly Notices of the Royal Astronomical Society, 399, 1403–1414
- Muzerolle, J., et al. 2009, *Evidence for Dynamical Changes in a Transitional Protoplanetary Disk with*



- Mid-Infrared Variability*, The Astrophysical Journal Letters, 704, L15–L19
- O'Brien, D. P., Morbidelli, A., & Levison, H. F. 2006, *Terrestrial planet formation with strong dynamical friction*, Icarus, 184, 39–58
- Olofsson, J., et al. 2009, *C2D Spitzer-IRS spectra of disks around T Tauri stars. IV. Crystalline silicates*, Astronomy & Astrophysics, 507, 327–345
- Ossenkopf, V. 1991, *Effective-medium theories for cosmic dust grains*, Astronomy & Astrophysics, 251, 210–219
- Owen, J. E., Ercolano, B., Clarke, C. J., & Alexander, R. D. 2010, *Radiation-hydrodynamic models of X-ray and EUV photoevaporating protoplanetary discs*, Monthly Notices of the Royal Astronomical Society, 401, 1415–1428
- Papaloizou, J. C. B., Nelson, R. P., & Masset, F. 2001, *Orbital eccentricity growth through disc-companion tidal interaction*, Astronomy & Astrophysics, 366, 263–275
- Perri, F., & Cameron, A. G. W. 1974, *Hydrodynamic instability of the solar nebula in the presence of a planetary core*, Icarus, 22, 416–425
- Peterson, D. M., et al. 2006, *Vega is a rapidly rotating star*, Nature, 440, 896–899
- Plavchan, P., Jura, M., & Lipsky, S. J. 2005, *Where Are the M Dwarf Disks Older Than 10 Million Years?*, The Astrophysical Journal, 631, 1161–1169
- Plavchan, P., Werner, M. W., Chen, C. H., Stapelfeldt, K. R., Su, K. Y. L., Stauffer, J. R., & Song, I. 2009, *New Debris Disks Around Young, Low-Mass Stars Discovered with the Spitzer Space Telescope*, The Astrophysical Journal, 698, 1068–1094
- Pollack, J. B., Hubickyj, O., Bodenheimer, P., Lissauer, J. J., Podolak, M., & Greenzweig, Y. 1996, *Formation of the Giant Planets by Concurrent Accretion of Solids and Gas*, Icarus, 124, 62–85
- Queck, M., Krivov, A. V., Sremčević, M., & Thébault, P. 2007, *Collisional Velocities and Rates in Resonant Planetesimal Belts*, Celestial Mechanics and Dynamical Astronomy, 99, 169–196
- Raymond, S. N., Quinn, T., & Lunine, J. I. 2006, *High-resolution simulations of the final assembly of Earth-like planets I. Terrestrial accretion and dynamics*, Icarus, 183, 265–282
- Reche, R., Beust, H., Augereau, J.-C., & Absil, O. 2008, *On the observability of resonant structures in planetesimal disks due to planetary migration*, Astronomy & Astrophysics, 480, 551–561
- Reidemeister, M., Krivov, A. V., Schmidt, T. O. B., Fiedler, S., Müller, S., Löhne, T., & Neuhäuser, R. 2009, *A possible architecture of the planetary system HR 8799*, Astronomy & Astrophysics, 503, 247–258
- Reidemeister, M., Krivov, A. V., Stark, C. C., Augereau, J. C., Löhne, T., & Müller, S. 2010, *Warm Dust around epsilon Eridani*, Astronomy & Astrophysics, submitted
- Rhee, J. H., Song, I., Zuckerman, B., & McElwain, M. 2007, *Characterization of Dusty Debris Disks: The IRAS and Hipparcos Catalogs*, The Astrophysical Journal, 660, 1556–1571
- Rice, W. K. M., & Armitage, P. J. 2003, *On the Formation Timescale and Core Masses of Gas Giant Planets*, The Astrophysical Journal Letters, 598, L55–L58
- Rice, W. K. M., Armitage, P. J., Bate, M. R., & Bonnell, I. A. 2003, *The effect of cooling on the global stability of self-gravitating protoplanetary discs*, Monthly Notices of the Royal Astronomical Society, 339, 1025–1030
- Rieke, G. H., et al. 2005, *Decay of Planetary Debris Disks*, The Astrophysical Journal, 620, 1010–1026
- Sadakane, K., & Nishida, M. 1986, *Twelve additional 'Vega-like' stars*, Publications of the Astronomical Society of the Pacific, 98, 685–689
- Safronov, V. S. 1969, *Evolution of the Protoplanetary Cloud and Formation of the Earth and the Planets* (Jerusalem, 1972: Israel Program for Scientific Translations), translated from Russian
- Schütz, O., Meeus, G., & Sterzik, M. F. 2005, *Mid-IR observations of circumstellar disks. II. Vega-type stars and a post-main sequence object*, Astronomy & Astrophysics, 431, 175–182

- Setiawan, J., Weise, P., Henning, T., Launhardt, R., Müller, A., & Rodmann, J. 2007, *Evidence for a Planetary Companion around a Nearby Young Star*, *The Astrophysical Journal Letters*, 660, L145–L148
- Shen, Y., Draine, B. T., & Johnson, E. T. 2008, *Modeling Porous Dust Grains with Ballistic Aggregates. I. Geometry and Optical Properties*, *The Astrophysical Journal*, 689, 260–275
- . 2009, *Modeling Porous Dust Grains with Ballistic Aggregates. II. Light Scattering Properties*, *The Astrophysical Journal*, 696, 2126–2137
- Shu, F., Najita, J., Galli, D., Ostriker, E., & Lizano, S. 1993, *The collapse of clouds and the formation and evolution of stars and disks*, in: *Protostars and Planets III*, ed. E. H. Levy & J. I. Lunine, 3–45
- Siegler, N., Muzerolle, J., Young, E. T., Rieke, G. H., Mamajek, E. E., Trilling, D. E., Gorlova, N., & Su, K. Y. L. 2007, *Spitzer 24  $\mu\text{m}$  Observations of Open Cluster IC 2391 and Debris Disk Evolution of FGK Stars*, *The Astrophysical Journal*, 654, 580–594
- Simon, M., & Prato, L. 1995, *Disk Dissipation in Single and Binary Young Star Systems in Taurus*, *The Astrophysical Journal*, 450, 824–829
- Sloan, G. C., Kraemer, K. E., Price, S. D., & Shipman, R. F. 2003, *A Uniform Database of 2.4–45.4 Micron Spectra from the Infrared Space Observatory Short Wavelength Spectrometer*, *The Astrophysical Journal Supplement*, 147, 379–401
- Spangler, C., Sargent, A. I., Silverstone, M. D., Becklin, E. E., & Zuckerman, B. 2001, *Dusty Debris around Solar-Type Stars: Temporal Disk Evolution*, *The Astrophysical Journal*, 555, 932–944
- Stark, C. C., & Kuchner, M. J. 2008, *The Detectability of Exo-Earths and Super-Earths Via Resonant Signatures in Exozodiacal Clouds*, *The Astrophysical Journal*, 686, 637–648
- . 2009, *A New Algorithm for Self-consistent Three-dimensional Modeling of Collisions in Dusty Debris Disks*, *The Astrophysical Journal*, 707, 543–553
- Stark, C. C., et al. 2009, *51 Ophiuchus: A Possible Beta Pictoris Analog Measured with the Keck Interferometer Nutter*, *The Astrophysical Journal*, 703, 1188–1197
- Stern, S. A., & Colwell, J. E. 1997, *Collisional Erosion in the Primordial Edgeworth-Kuiper Belt and the Generation of the 30–50 AU Kuiper Gap*, *The Astrophysical Journal*, 490, 879–883
- Stewart, S. T., & Leinhardt, Z. M. 2009, *Velocity-Dependent Catastrophic Disruption Criteria for Planetesimals*, *The Astrophysical Journal Letters*, 691, L133–L137
- Stognienko, R., Henning, T., & Ossenkopf, V. 1995, *Optical properties of coagulated particles.*, *Astronomy & Astrophysics*, 296, 797–809
- Strubbe, L. E., & Chiang, E. I. 2006, *Dust Dynamics, Surface Brightness Profiles, and Thermal Spectra of Debris Disks: The Case of AU Microscopii*, *The Astrophysical Journal*, 648, 652–665
- Su, K. Y. L., et al. 2005, *The Vega Debris Disk: A Surprise from Spitzer*, *The Astrophysical Journal*, 628, 487–500
- . 2006, *Debris Disk Evolution around A Stars*, *The Astrophysical Journal*, 653, 675–689
- . 2009, *The Debris Disk Around HR 8799*, *The Astrophysical Journal*, 705, 314–327
- Sylvester, R. J., Skinner, C. J., Barlow, M. J., & Mannings, V. 1996, *Optical, infrared and millimetre-wave properties of Vega-like systems.*, *Monthly Notices of the Royal Astronomical Society*, 279, 915–939
- Tamanai, A., Mutschke, H., Blum, J., & Meeus, G. 2006, *The 10  $\mu\text{m}$  Infrared Band of Silicate Dust: A Laboratory Study Comparing the Aerosol and KBr Pellet Techniques*, *The Astrophysical Journal Letters*, 648, L147–L150
- Tanigawa, T., & Ikoma, M. 2007, *A Systematic Study of the Final Masses of Gas Giant Planets*, *The Astrophysical Journal*, 667, 557–570
- Tanner, A., Beichman, C., Bryden, G., Lisse, C., & Lawler, S. 2009, *Survey of Nearby FGK Stars at 160  $\mu\text{m}$  with Spitzer*, *The Astrophysical Journal*, 704, 109–116
- Thébaud, P. 2009, *Vertical structure of debris discs*, *Astronomy & Astrophysics*, 505, 1269–1276

- Thébault, P., & Augereau, J.-C. 2007, *Collisional processes and size distribution in spatially extended debris discs*, *Astronomy & Astrophysics*, 472, 169–185
- Thébault, P., Augereau, J. C., & Beust, H. 2003, *Dust production from collisions in extrasolar planetary systems. The inner beta Pictoris disc*, *Astronomy & Astrophysics*, 408, 775–788
- Thébault, P., & Brahic, A. 1999, *Dynamical influence of a proto-Jupiter on a disc of colliding planetesimals.*, *Planetary and Space Science*, 47, 233–243
- Thébault, P., Marzari, F., & Scholl, H. 2002, *Terrestrial planet formation in exoplanetary systems with a giant planet on an external orbit*, *Astronomy & Astrophysics*, 384, 594–602
- Thébault, P., & Wu, Y. 2008, *Outer edges of debris discs. How sharp is sharp?*, *Astronomy & Astrophysics*, 481, 713–724
- Toomre, A. 1964, *On the gravitational stability of a disk of stars*, *The Astrophysical Journal*, 139, 1217–1238
- Trilling, D. E., & Bernstein, G. M. 2006, *Light Curves of 20-100 km Kuiper Belt Objects Using the Hubble Space Telescope*, *The Astronomical Journal*, 131, 1149–1162
- Trilling, D. E., et al. 2007, *Debris disks in main-sequence binary systems.*, *The Astrophysical Journal*, 658, 1289–1311
- . 2008, *Debris Disks around Sun-like Stars*, *The Astrophysical Journal*, 674, 1086–1105
- Vitense, C., Krivov, A. V., & Löhne, T. 2010, *The Edgeworth-Kuiper debris disk*, *Astronomy & Astrophysics*, 520, A32–A49
- Wada, K., Tanaka, H., Suyama, T., Kimura, H., & Yamamoto, T. 2009, *Collisional Growth Conditions for Dust Aggregates*, *The Astrophysical Journal*, 702, 1490–1501
- Walker, H. J., & Wolstencroft, R. D. 1988, *Cool circumstellar matter around nearby main-sequence stars*, *Publications of the Astronomical Society of the Pacific*, 100, 1509–1521
- Warren, S. G. 1984, *Optical constants of ice from the ultraviolet to the microwave*, *Applied Optics*, 23, 1206–1225
- Weidenschilling, S. J. 1980, *Dust to planetesimals - Settling and coagulation in the solar nebula*, *Icarus*, 44, 172–189
- Weidenschilling, S. J., Spaute, D., Davis, D. R., Marzari, F., & Ohtsuki, K. 1997, *Accretional Evolution of a Planetesimal Swarm*, *Icarus*, 128, 429–455
- Wetherill, G. W., & Stewart, G. R. 1993, *Formation of planetary embryos - Effects of fragmentation, low relative velocity, and independent variation of eccentricity and inclination*, *Icarus*, 106, 190–209
- Williams, J. P., & Andrews, S. M. 2006, *The Dust Properties of Eight Debris Disk Candidates as Determined by Submillimeter Photometry*, *The Astrophysical Journal*, 653, 1480–1485
- Williams, J. P., Najita, J., Liu, M. C., Bottinelli, S., Carpenter, J. M., Hillenbrand, L. A., Meyer, M. R., & Soderblom, D. R. 2004, *Detection of Cool Dust around the G2 V Star HD 107146*, *The Astrophysical Journal*, 604, 414–419
- Wilner, D. J., Holman, M. J., Kuchner, M. J., & Ho, P. T. P. 2002, *Structure in the Dusty Debris around Vega*, *The Astrophysical Journal Letters*, 569, L115–L119
- Witten, T. A., & Cates, M. E. 1986, *Tenuous Structures from Disorderly Growth Processes*, *Science*, 232, 1607–1612
- Wolf, S. 2008, *Signatures of planets in young and evolved circumstellar disks*, *Physica Scripta Volume T130*, 130, 1–6
- Wolf, S., Henning, T., & Stecklum, B. 1999, *Multidimensional self-consistent radiative transfer simulations based on the Monte-Carlo method*, *Astronomy & Astrophysics*, 349, 839–850
- Wolf, S., & Hillenbrand, L. A. 2003, *Model Spectral Energy Distributions of Circumstellar Debris Disks. I. Analytic Disk Density Distributions*, *The Astrophysical Journal*, 596, 603–620
- . 2005, *Debris disk radiative transfer simulation tool (DDS)*, *Computer Physics Communications*, 171,

- 208–218
- Wolf, S., Moro-Martín, A., & D'Angelo, G. 2007, *Signatures of planets in protoplanetary and debris disks*, *Planetary and Space Science*, 55, 569–581
- Wolf, S., Padgett, D. L., & Stapelfeldt, K. R. 2003, *The Circumstellar Disk of the Butterfly Star in Taurus*, *The Astrophysical Journal*, 588, 373–386
- Wolf, S., Schegerer, A., Beuther, H., Padgett, D. L., & Stapelfeldt, K. R. 2008, *Submillimeter Structure of the Disk of the Butterfly Star*, *The Astrophysical Journal Letters*, 674, L101–L104
- Wolf, S., & Voshchinnikov, N. V. 2004, *Mie scattering by ensembles of particles with very large size parameters*, *Computer Physics Communications*, 162, 113–123
- Wolk, S. J., & Walter, F. M. 1996, *A Search for Protoplanetary Disks Around Naked T Tauri Stars*, *The Astronomical Journal*, 111, 2066–2076
- Wolstencroft, R. D., & Walker, H. J. 1988, *Dust discs around low-mass main-sequence stars*, *Royal Society of London Philosophical Transactions Series A*, 325, 423–437
- Wolszczan, A., & Frail, D. A. 1992, *A planetary system around the millisecond pulsar PSR1257 + 12*, *Nature*, 355, 145–147
- Wyatt, M. C. 2003, *Resonant Trapping of Planetesimals by Planet Migration: Debris Disk Clumps and Vega's Similarity to the Solar System*, *The Astrophysical Journal*, 598, 1321–1340
- . 2005a, *Spiral structure when setting up pericentre glow: possible giant planets at hundreds of AU in the HD 141569 disk*, *Astronomy & Astrophysics*, 440, 937–948
- . 2005b, *The insignificance of P-R drag in detectable extrasolar planetesimal belts*, *Astronomy & Astrophysics*, 433, 1007–1012
- . 2006, *Dust in Resonant Extrasolar Kuiper Belts: Grain Size and Wavelength Dependence of Disk Structure*, *The Astrophysical Journal*, 639, 1153–1165
- . 2008, *Evolution of Debris Disks*, *Annual Review of Astronomy and Astrophysics*, 46, 339–383
- Wyatt, M. C., Clarke, C. J., & Greaves, J. S. 2007a, *Origin of the metallicity dependence of exoplanet host stars in the protoplanetary disc mass distribution*, *Monthly Notices of the Royal Astronomical Society*, 380, 1737–1743
- Wyatt, M. C., & Dent, W. R. F. 2002, *Collisional processes in extrasolar planetesimal discs - dust clumps in Fomalhaut's debris disc*, *Monthly Notices of the Royal Astronomical Society*, 334, 589–607
- Wyatt, M. C., Smith, R., Greaves, J. S., Beichman, C. A., Bryden, G., & Lisse, C. M. 2007b, *Transience of Hot Dust around Sun-like Stars*, *The Astrophysical Journal*, 658, 569–583
- Wyatt, M. C., Smith, R., Su, K. Y. L., Rieke, G. H., Greaves, J. S., Beichman, C. A., & Bryden, G. 2007c, *Steady State Evolution of Debris Disks around A Stars*, *The Astrophysical Journal*, 663, 365–382
- Wyatt, S. P. 1969, *The electrostatic charge of interplanetary grains*, *Planetary and Space Science*, 17, 155–171
- Zuckerman, B., & Becklin, E. E. 1993, *Submillimeter studies of main-sequence stars*, *The Astrophysical Journal*, 414, 793–802
- Zuckerman, B., & Song, I. 2004, *Dusty Debris Disks as Signposts of Planets: Implications for Spitzer Space Telescope*, *The Astrophysical Journal*, 603, 738–743

# Danksagung

*The smallest act of kindness is worth more than the grandest intention.*

OSCAR WILDE

Abschließend möchte ich allen danken, die zum Gelingen dieser Arbeit beigetragen haben. An ertser Stelle ist da Prof. Alexander Krivov zu nennen, der trotz aller „Schusseligkeiten“ meinerseits immer geduldig blieb und mir weiterhin sein Vertrauen geschenkt hat. Besonders dankbar bin ich ihm vor allem aber dafür, dass er es mir im Zuge meiner Promotion, ungeachtet der knappen Finanzlage, immer wieder ermöglicht hat, die Welt zu bereisen und somit einen großen Beitrag nicht nur zu meiner fachlichen, aber auch zu meiner persönlichen Entwicklung in den letzten drei Jahren geleistet hat.

Desweiteren ist es zu einem großen Teil Dr. Torsten Löhne zu verdanken, dass die letzten drei Jahre erfolgreich verlaufen sind. Ab und zu wird er sicherlich den Tag verflucht haben, an dem ich in sein Büro gezogen bin — besonders wenn die morgendliche Begrüßung in einen etwas genervten „Torsten, sag mal...“ bestand. Dass er sich dennoch immer die Zeit genommen hat, sich geduldig mit meinen Fragen und Problemen auseinanderzusetzen (so trivial sie auch manchmal waren), rechne ich ihm hoch an.

Die Zeit am AIU wäre wohl nicht so angenehm, wären da nicht auch noch die andere Kollegen, neben den bereits genannten allen voran Martin Reidemeister, Christian Vitense und Dr. Hiroshi Kobayashi. Viele fachliche, aber auch private Diskussionen im Büro oder in der Mittagspause machen den Arbeitsalltag abwechslungsreich.

Dass mein Forschungsaufenthalt in Kobe tatsächlich stattfinden konnte, habe ich vor allem der ausgiebigen Unterstützung durch Prof. Hiroshi Kimura und Nagisa Machii, sowie den liebenswerten Sekretärinnen des CPS in Kobe zu verdanken. Dank ihnen durfte ich die aufregenden drei Monate meines Lebens in Japan verbringen. Für die Hilfe bei den Vorbereitungen von Jena aus, möchte ich mich herzlich bei Dr. Akemi Tamanai und Dr. Hiroshi Kobayashi bedanken.

Wie schon angedeutet, geht natürlich nichts ohne das entsprechende Kleingeld. Daher gilt mein Dank der DFG, die mein erstes Promotionsjahr finanziert hat, sowie dem Freistaat Thüringen, der über das *Thüringer Landesstipendium* die Finanzierung der verbliebenen Promotionsdauer übernommen hat. Fast alle Dienstreisen und Forschungsaufenthalte waren nur möglich durch die Unterstützung von DAAD, AAS, CPS und der *Wilhelm und Else Heraeus Stiftung* in Form von Kooperationsprojekten und Reisestipendien.

Desweiteren sei noch allen gedankt, die zu der Verbesserung dieser Dissertation beigetragen haben. So waren die inhaltlichen Anmerkungen von Sascha, Torsten und Hiroshi sehr hilfreich. Angesichts meines rudimentären Englischs war die sprachliche Überarbeitung sehr wichtig — danke Sebastian (es ist immer gut, wenn der beste Freund erfolgreich Englisch studiert hat).

Zu guter Letzt möchte ich mich bei meiner Freundin, meiner Familie und bei meinen Freunden bedanken, die mich im Laufe der letzten Jahre immer wieder auf den Boden zurück geholt haben und, falls notwendig, immer ein offenes Ohr für mich hatten.

# Ehrenwörtliche Erklärung

Ich erkläre hiermit ehrenwörtlich, dass ich die vorliegende Arbeit selbstständig, ohne die unzulässige Hilfe Dritter und ohne die Benutzung anderer als der angegebenen Hilfsmittel und Literatur angefertigt habe. Die aus anderen Quellen direkt oder indirekt übernommenen Daten und Konzepte sind unter Angabe der Quelle gekennzeichnet. Bei der inhaltlich-materiellen Erstellung der vorliegenden Arbeit waren keine weiteren Personen beteiligt. Insbesondere habe ich hierfür nicht die entgeltliche Hilfe von Vermittlungs- und bzw. Beratungsdiensten (Promotionsberater oder andere Personen) in Anspruch genommen. Niemand hat von mir unmittelbar oder mittelbar geldwerte Leistungen für Arbeiten erhalten, die im Zusammenhang mit dem Inhalt der vorgelegten Dissertation stehen.

Die Arbeit wurde bisher weder im In- noch im Ausland in gleicher oder ähnlicher Form einer anderen Prüfungsbehörde vorgelegt.

Die geltende Promotionsordnung der Physikalisch-Astronomischen Fakultät ist mir bekannt.

Ich versichere ehrenwörtlich, dass ich nach bestem Wissen die reine Wahrheit gesagt und nichts verschwiegen habe.

Jena, den 26.04.2010

---

Müller, Sebastian

# Curriculum Vitae

- PERSÖNLICHE DATEN
- ◇ Voller Name: Sebastian Müller
  - ◇ Geburtstag: 21.03.1983
  - ◇ Geburtsort: Dortmund, NRW (Deutschland)
  - ◇ Staatsangehörigkeit: Deutsch
- AUSBILDUNG
- ◇ 1989 – 1993: Aplerbecker Grundschule, Dortmund
  - ◇ 1993 – 2002: Gymnasium an der Schweizer Allee, Dortmund  
Abitur, Note: 1,4
  - ◇ 2002 – 2004: Universität Dortmund  
Vordiplom Physik, Note: sehr gut
  - ◇ 2004 – 2007: Friedrich–Schiller–Universität Jena  
Diplom Physik, Note: mit Auszeichnung (1,0)  
Diplomarbeit (Betr. Prof. A. V. Krivov): *Berechnung photometrischer Eigenschaften von zirkumstellaren Trümmerscheiben*
  - ◇ seit 2007: Friedrich–Schiller–Universität Jena  
Promotion (Dr. rer. nat.), Note: magna cum laude  
Dissertation (Betr. Prof. A. V. Krivov): *Thermal Emission Modeling of Circumstellar Debris Disks*
- LEHRE
- ◇ SS 07: Korrektur der Übungsaufgaben zur Vorlesung *Planetenentstehung* (Prof. Dr. Krivov)
  - ◇ WS 07/08: Betreuung von Physiktudenten (3. Semester) als Assistent des Physikalischen Grundpartikums
  - ◇ SS 08: Betreuung von Physiktudenten (1. Semester) als Assistent des Physikalischen Grundpartikums
  - ◇ WS 08/09: Betreuung von Nebenfachsstudenten als Assistent des Physikalischen Grundpartikums
  - ◇ SS 09: Betreuung von Nebenfachsstudenten als Assistent des Physikalischen Grundpartikums
- STIPENDIEN
- ◇ 10.2008 – 09.2010: Graduiertenstipendium des Freistaats Thüringen zur Finanzierung der Promotion
  - ◇ 06./07.2008: Wilhelm und Else Heraeus-Fellowship zur Teilnahme am 58th Meeting of Nobel Laureates
  - ◇ 10.2008: Hartman Travel Grand der AAS/DPS zur Teilnahme am 40th Meeting of the AAS Division for Planetary Sciences
  - ◇ 01.2009: Reiseunterstützung des CPS zur Teilnahme an der CPS International School of Planetary Sciences 2009
  - ◇ 09. – 11.2009: Reiseunterstützung des CPS zur Teilnahme an einem Austauschprogramm mit der Universität Kobe

- ÖFFENTLICHE VORTRÄGE
- ◇ 19.09.2007: 40th Meeting of the AAS / DPS  
*Ithaca, NY, USA* What Children Tell us about Their Parents
  - ◇ 06.04.2009: ISSI-Meeting  
*Bern, Schweiz* What IR photometry and Spectrometry Can Tell Us About Exozodis
  - ◇ 07.04.2009: ISSI-Meeting  
*Bern, Schweiz* HD 69830 Exozodi: Combining Dynamics and Spectroscopy
  - ◇ 10.09.2009: CPS-Seminar  
*Kobe, Japan* Debris Disks and Their Dust
  - ◇ 29.10.2009: Group Seminar  
*Nagoya, Japan* Debris Disks and Their Dust
  - ◇ 25.11.2009: EPS TV-Seminar  
*Kobe, Japan* Debris Disks and Their Dust
- KONFERENZEN & DIENSTREISEN
- ◇ 19.09. – 21.09.2007: 5th Planet Formation Workshop  
*Braunschweig*
  - ◇ 18.02. – 22.02.2008: The Early Phase of Planet Formation (Winterschule)  
*Bad Honnef*
  - ◇ 29.06. – 04.07.2008: 58th Meeting of Nobel Laureates (dedicated to Physics)  
*Lindau*
  - ◇ 14.07. – 16.07.2008: DUNES Modeling Workshop  
*Jena*
  - ◇ 08.09. – 12.09.2008: Cosmic Dust Near & Far  
*Heidelberg*
  - ◇ 06.10. – 08.10.2008: Forschungsbesuch im Rahmen eines DAAD Projekts  
*Grenoble, Frankreich*
  - ◇ 11.10. – 15.10.2008: 40th Meeting of the AAS Division for Planetary Sciences  
*Ithaca, NY, USA*
  - ◇ 05.01. – 09.01.2009: Dust in Space (CPS Winterschule)  
*Kobe, Japan*
  - ◇ 06.04. – 10.04.2009: ISSI Meeting (Exozodiacal Dust Disks and Darwin)  
*Bern, Schweiz*
  - ◇ 24.05. – 01.06.2009: Forschungsbesuch im Rahmen des ISSI Projekts  
*Grenoble, Frankreich*
  - ◇ 01.09. – 30.11.2009: Forschungsreise im Rahmen eines CPS Austauschprogramms  
*Kobe, Japan*
  - ◇ 08.03. – 12.03.2010: Forschungsbesuch im Rahmen des Herschel/DUNES Projekts  
*Grenoble, Frankreich*
  - ◇ 04.05. – 07.05.2010: Herschel First Results Symposium  
*Noordwijk, Niederlande*
  - ◇ 05.09. – 06.09.2010: Arbeitstreffen der DUNES-Kollaboration für die Herschel Raumsonde  
*Göteborg, Schweden*



- PUBLIKA –  
TIONEN
- ◇ A. V. Krivov, S. Müller, T. Löhne & H. Mutschke  
*Collisional and Thermal Emission Models of Debris Disks:  
Toward Planetesimal Population Properties*  
The Astrophysical Journal 687, 608 – 622, 2008
  - ◇ M. Reidemeister, A. V. Krivov, T. O. B. Schmidt, S. Fiedler, S. Müller,  
T. Löhne, & R. Neuhäuser  
*A possible architecture of the planetary system HR 8799*  
Astronomy & Astrophysics 503, 247 – 258, 2009
  - ◇ S. Müller, T. Löhne & A. V. Krivov  
*The Debris Disk of Vega: A Steady-state Collisional Cascade, Naturally*  
The Astrophysical Journal 708, 1728 – 1747, 2010
  - ◇ C. Eiroa, D. Fidele, J. Maldonado, 35 Co-Autoren, S. Müller  
& 10 Co-Autoren  
*Cold DUsT around NEarby Stars (DUNES). First Results  
A Resolved Exo-Kuiper Belt around the Solar-Like Star  $\zeta^2$  Ret*  
Astronomy & Astrophysics, 518, L132, 2010
  - ◇ R. Liseau, C. Eiroa, D. Fidele, 23 Co-Autoren, S. Müller & 8 Co-Autoren  
*Resolving the Cold Debris Disc around a Planet-Hosting Star  
PACS Photometric Imaging Observations of  $q^1$  Eri (HD 10647, HR 506)*  
Astronomy & Astrophysics 518, L131, 2010
  - ◇ M. Reidemeister, A. V. Krivov, C. C. Stark, J.-C. Augereau, T. Löhne  
& S. Müller  
*Warm Dust around epsilon Eridani*  
Astronomy & Astrophysics, eingereicht